5. MATERIAL SCIENCE & TECHNOLOGY

5.1. Lectures

L01 SIMULATION OF TENSILE CHARACTERISTICS OF THE NANOCRYSTALLINE MATERIALS: AFFINE AND PHANTOM NETWORK MODEL

JAN ŽÍDEK and JOSEF JANČÁŘ
Institute of Materials Science, Faculty of Chemistry, Brno University of Technology, Purkyňova 118, 612 00 Brno, Czech Republic, zidek@fch.vutbr.cz

Introduction

Application of polymer materials was developed from the consumer goods and packaging to the field of sophisticated engineering applications during the last decades. This stimulated the research on the morphology – mechanical property relationships. Mostly, the materials with tailored properties are required. It is possible to develop the material with desired mechanical properties by an empirical work or by combination of theoretical prediction and experimental techniques. Model simulations cannot predict exactly composition of the material with ideal mechanical properties, however, they can narrow the area of the structural variables and accelerate the material development. Combination of experimental work with precedent theoretical calculations is promising for investigation of nanocomposites, too. Some structural mechanical property relations clearly observable in the systems of nanoparticle are helpful for understanding of the properties of other materials. Therefore, an appropriate model of nanostructures with easily available input parameters and desired output values will make the investigation of materials more efficient.

Several approaches are used to the modeling of the mechanical response of solids with varying structure. Mostly finite element method (FEM) is used. It allows to calculate the surroundings of one nanocrystallite as well as to model the whole product. The finite element studies discretize the material into the elements, which load-deformation relations are known. The resulting mechanical properties are calculated by addition of mechanical properties of the individual components. The usual finite element methods for tensile properties of composites[1] discretize the surroundings of one crystallite. When the size of the crystallite (or particle) is in the nano-scale, the size of the element falls to the molecular level. So, the chain between two entanglements would be taken as an element. The model was first proposed by Termonia[2] for the calculation of the properties of spider silk. In this approach, the silk fiber was represented by an array of β-pleated sheets rich in alanine, which were interconnected by amorphous chain rich in glycine. The chains were linked together by entanglements. The chains between the crystallite and amorphous phase had limited segmental mobility and, therefore, the chains in the interphase were more rigid than those in the bulk of amorphous phase and they had higher modulus of elasticity.

Termonia assumed that when the semicrystalline polymer was deformed, the deformation of the crystalline phase is very small, whereas the amorphous phase was deformed extensively. Therefore, the deformation of the crystalline phase did not exceed the elastic region and the tension of the crystalline phase could be calculated from the Hooke's law:

$$\sigma = E\,\varepsilon \tag{1}$$

The non-Gaussian theory of elasticity was used as a theoretical principle on single chain mechanics. The chain was considered a set of segments joined serially. The deformation was followed by the change of conformation entropy and the tensile properties were calculated by means of the inverse Langevin function[3].

$$\sigma = \frac{1}{3} E \sqrt{N} L^{-1}\left(\frac{\lambda}{\sqrt{N}}\right) \tag{2}$$

where E is Young modulus; N–number of segments of the chain; λ – draw ratio (elongation) of the chain and L^{-1} is an Inverse Langevin function[4]:

$$L(x) = \coth(x) - x^{-1} \tag{3}$$

We would like to adapt our model to the calculation of dynamic mechanical stress/relaxation response which is often observed in polymers[5]. Load applied to the sample oscilates sinusoidally and the deformation response is also sinusoidal but with certain phase shifts (see Fig. 1.) This is a combination of elastic – solid like – and viscous – liquid like – properties. Elastic properties are interpreted by rubber elasticity and molecular mechanics. Viscosity is caused by several reasons[6] e. g. diffusion of chains in surroundings with steric obstacles, retraction polymer chain by rearrangement

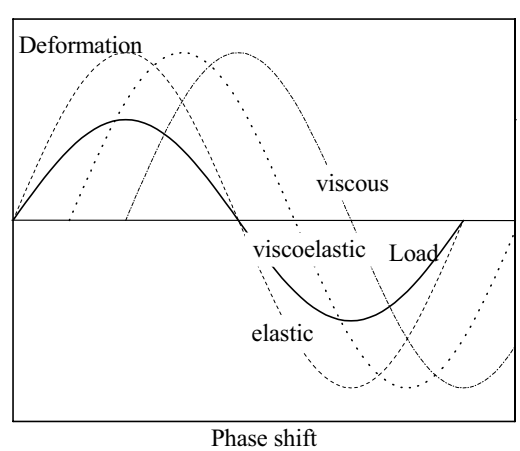

Fig. 1. **Load-deformation response for a sample subjected to sinusoidal load; elastic component – In phase; viscous component (phase shift angle is π/2 RAD)**

of chain conformations and sliding of links of chains in the entanglement. Therefore, different types of network should be introduced into the model.

The model of Termonia was extended in our work. The structure was approached to the real structure of nano-filled materials.

In our model[7] the 3D-network of entanglements was created. Each entanglement had its position given by the space coordinates. Then the chains connecting two entanglements and the nanocrystallite were introduced into the model. Modulus of each chain was set according to its distance from the nanocrystallite.

The network was deformed stepwise from undeformed state, where the elongation ratio λ was 1 to the elongation ratio λ_{MAX}. In each step, the network was first deformed uniformly. After, the equilibrium state of the model was searched. The composition of all forces acting on one entanglement was made. When the entanglement was in the equilibrium position, the total force acting on it was equal to zero. If the force was of non zero value, the entanglement was moved in the direction of vector of total force until the force was zeroized. The total force was minimized several times for each entanglement and for the interphase nanoparticle-amorphous chains. When all components of the model reached the equilibrium state, the resulting tension of the model was calculated from the tension of all chains in the model and the tension of nanoparticle.

Our new network model enabled to calculate except of tensile deformation the shear and cyclic shear deformation.

Two types of network were used in the model. First, affine network was used in the basic model. The chains in entanglements were considered as compact and exchange of the chain links between two chains was disabled. The phantom network was considered a set of freely entangled chain, where each loop can move until reaching of the equilibrium state. The loading mode was changed from simple stretching to the shear deformation, because in the shear mode the relaxation is visible more clearly. Elastic response of stress-shear deformation curve should be observed because both affine and phantom network reached equilibrium position during the test.

The model was adapted so the viscoelastic properties were observable. Dynamic properties can be observed in the model when after making a step of deformation and before the next step, should not model reach the equilibrium state. The simplified mode of simulation of non-equilibrium state was made introduced. One step of deformation was made and reached equilibrium position of all nods. After, affine/phantom character of the nods was re-arranged, so the model fell into the non-equilibrium state. When this mode was applied, the inelastic relaxation of the stress should be observed in the model.

Results and discussion

The model of a fiber in an amorphous phase was created. The chains in the immediate vicinity of the solid particle were marked as the interface chains and were fixed to the surface of the particle. The modulus of the amorphous phase was 0.5 GPa and the modulus of the solid particle was 200 GPa. Only the chains in the immediate vicinity were considered interphase and its modulus was 10 times higher than modulus of amorphous phase. The volume fraction of the nano-crystallite was 46 volume percent. Part of the nods was randomly set as phantom and complementary part stood affine.

Skew deformation mode was used in the simulation. The deformation started in the undeformed state with ratio 1.00 increased up to the deformation ratio 1.1 after it decreased to the elongation ratio 0.9 and again increased up to deformation ratio 1.1. Only the rubber elastic component was taken. The second component hanging together with stretching of bonds, bond angles and dihedral angles was not considered.

The character of each nod was set before calculation and the distribution of nods stood conserved during the simulation. Dependence of stress–shear deformation characteristics as a function of amount of phantom nods was investigated See Fig. 2. The limit cases with 0 % and 100 % of phantom nods are fully affine and phantom networks.

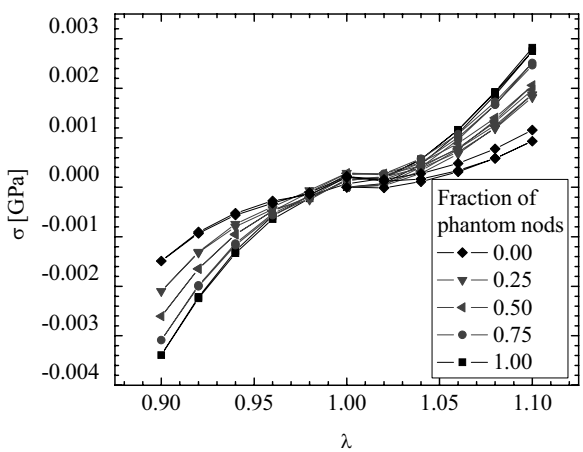

Fig. 2. **Stress-shear deformation curves of heterogenous network model of surrounding of one particle as a function of nod type. Phantom nod – freely entangled chains, affine nod – both chains are fixed. Fraction of affine nod is complementary to the phatom**

The dynamic properties were activated in the combined Phantom/Affine network. Re-distribution of the phantom/affine nod characters were made after each step. Results were shown in the Fig. 3.

It was found that, the stress-shear deformation curve of the depended on the type of network. The stiffness of the affine network was higher than the stiffness phantom network. It corresponded to reality, because the affine network corresponds to the material in a solid state, whereas the phantom network corresponded to the melt.

The model of each phantom/affine ratio in the first series had always elastic response. It was because, after each step, equilibrium position was reached.

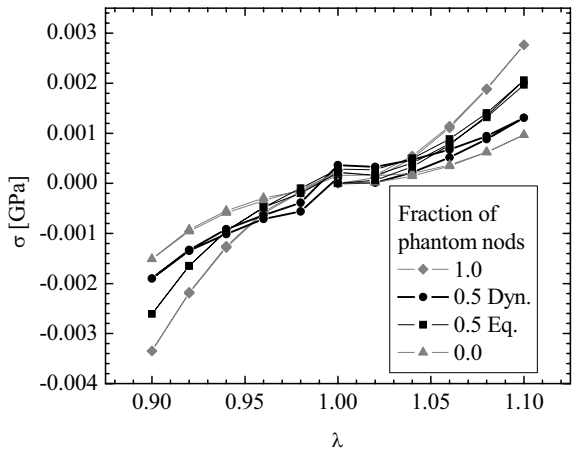

Fig. 3. **Stress-shear deformation curves of heterogenous network model from Fig. 1. Thick line – Dynamic mode Character of each nods switched many times during the simulation to induce inelastic stress-relaxation response**

The non-equilibrium network model adapted to the properties had inelastic response.

Conclusion

Shear deformation was applied to the heterogenous network model with different volume fraction of affine and phantom nods.

Stress-shear deformation curves of heterogenous material depended on used network type. The stiffness of network is increasing with increasing amount of affine nods.

The deformation was performed stepwise. After each step the model was into the equilibrium position. Therefore, both phantom and affine network have elastic deformation response, that the stress–shear deformation curve had the same trace when the model was deformed and the deformation was relaxed.

Simplified process enabling simulate dynamic properties was included into the model. After each step the equilibrium position was found. Before making the next step, the character of the nods was re-arranged and so the model came to non-equilibrium position. This model had inelastic relaxation properties.

This research was supported by Ministry of Education of the Czech Republic under research project MSM 0021630501.

REFERENCES

1. Agarwall B. D.: *Dissertation*. University Microfilms International, Michigan USA 1972.
2. Termonia Y.: Macromolecules; *24*, 1128 (1991).
3. Davis H.: Macromolecules; *28*, 1060 (1995).
4. http://scienceworld.wolfram.com/physics/LangevinFunction.html.
5. Sperling, L. H.: *Introduction to physical polymer science*, Wiley-Interscience, New York 2001.
6. Benallal A., Marin G., Monfort J. P., Derail C.: Macromolecules; *26*, 7229 (1993).
7. Zidek J. Jancar J.: 11th International Conference Polymeric Materials 2004: Properties of polymer and applications, Halle, 2004, Book of Abstract (Michler G. H., ed.) p C02.

L02 NEW PERSPECTIVES OF PLASMA POLYMERIZATION

VLADIMIR CECH, RADEK PRIKRYL
and JAN STUDYNKA
Institute of Materials Chemistry, Brno University of Technology, Purkynova 118, CZ-612 00 Brno, Czech Republic, cech@fch.vutbr.cz

Introduction

Technological applications of new materials often require them to be in the form of thin films. Many thin-film processing techniques have been developed for the fabrication of monolayers and single layers. Some of the techniques are able to prepare high quality thin films with high reproducibility. This level of technology has enabled us to deal with more complicated film systems. Over the last ten years, scientists from varying backgrounds have rallied around a versatile new method for the synthesis of multilayer thin films[1]. Because the layer-by-layer assembly method provides opportunities for creative design and application of function-specific films, the field has experienced an initial period of exponential growth. In complex systems, new properties appear that are not observed for each individual component. Plasma-enhanced chemical vapor deposition (PE CVD) is one of the perspective techniques[2] suitable for deposition of complex film structures.

In PE CVD, chemical activation is achieved by supplying electrical power to a gas at reduced pressure (10^{-1}–10^{3} Pa). At that pressure, the application of a sufficiently high voltage creates a visible glow, called glow discharge plasma. The low temperature plasma consists of about equal concentration of ions and electrons. Charge recombination processes and relaxation of electronically excited atoms and molecules cause the visible glow. The electrical power is coupled into the gas through the mediation of plasma electrons. The energetic electrons in the plasma ionize the gas, if only to a minor extent – about one part per million. The electrons chemically activate a much larger fraction of the gas, about 1 percent. The increased chemical activity of the gas (monomer vapor) results primarily from dissociation of the molecules into smaller species, called radicals. Radicals are chemically unsaturated and therefore capable of chemical reactions at high rates; they are the species that react at a surface (substrate) and contribute to film formation. Plasma polymerization is a film-forming process, in which growth of low-molecular-weight molecules (monomers) into high-molecular-weight molecules (polymers) occurs with the assistance of the plasma energy[3]. It should be emphasized,

that the adjective "plasma" does not mean a kind of activated species propagating polymeric chains in plasma polymerization in contrast to radical or ionic polymerizations. The term "plasma" means an energy source to initiate polymerization reactions. In many cases, polymers formed by plasma polymerization show distinguished chemical composition, and chemical and physical properties from those formed by conventional polymerizations, if the same monomer is used for the two polymerizations. This uniqueness of plasma polymers results from the reaction mechanism of the polymer--forming process.

Plasma polymer films of controlled properties

Plasma-polymerized organosilicones constitute a class of materials with a rich and varied scientific background. This class of materials possesses a special characteristic, which distinguishes it from other plasma polymers. It is the ability to vary and control the degree of organic/inorganic character (that is, the carbon content) by appropriate choice of fabrication variables. This allows one to control many physico-chemical properties over wide ranges resulting in an extraordinary potential for useful applications, which are now only beginning to be tapped. The organosilicon plasma polymers are widely observed with respect to the potential for optical, mechanical and electronics applications.

Plasma polymer films of vinyltriethoxysilane (VTES) were deposited on planar glass or silicon substrates using a helical coupling plasma system (13.56 MHz) and selected deposition conditions (monomer vapor flowrate 0.45 sccm, process pressure 0.02 mbar); details on the apparatus have been described in Ref. 4. The effective power was ranging from 0.05 to 25 W, using pulsed plasma with t_{on} = 1 ms and a total power of 50 W. Plasma polymerized (pp-) films were continuous and homogeneous for the film thickness ranging from 5 nm to 4 μm evaluated by ellipsometry. The deposition rate varied as a function of the effective power in a range of 1–120 nm min^{-1} and thus the film thickness could be controlled by deposition time. The elemental composition in surface region (top 6–8 nm) of the deposited films was determined by X-ray photoelectron spectroscopy (XPS) and atomic concentrations corresponding to the pp-films are depicted in Fig. 1.

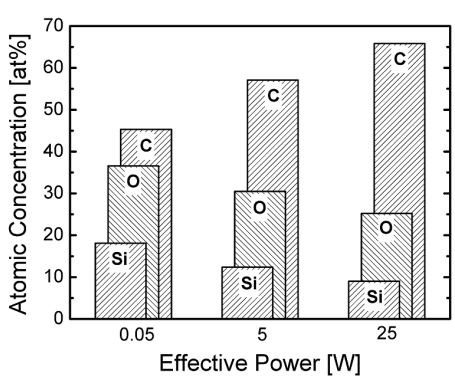

Fig. 1. **Elemental composition of pp-films deposited at different power was evaluated from XPS spectra**

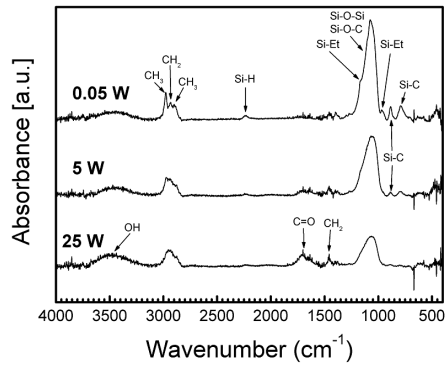

Fig. 2. **Infrared spectra of pp-films corresponding to different power**

Chemical structure of plasma polymer films depended on the effective power used, see infrared spectra (FTIR) (Fig. 2.).

The pp-film was constituted by Si–O–Si/Si–O–C network with side ethoxy groups that decreased when increasing the power. The absorption bands corresponding to the C=O and OH stretching vibrations were apparent for pp-films deposited at higher power. However, the vinyl groups in the pp-VTES were not confirmed by FTIR spectroscopy even if a very low power was used. The surface elemental composition of films corresponded to a bulk one determined by Rutherford backscattering (RBS) measurements. The organic/inorganic character of the pp-film was varied extensively and can be expressed by element ratio of C/Si, which increased from 2.5 to 7.3 enhancing the power.

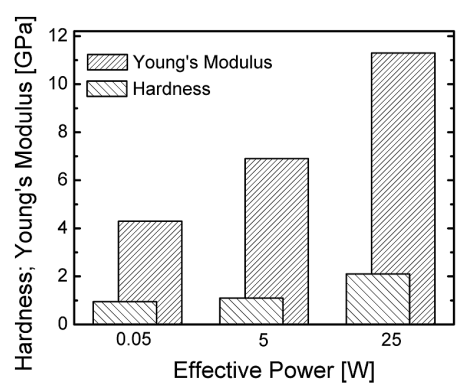

Fig. 3. **Young's modulus and hardness of pp-films prepared at different power**

The Young's modulus and the hardness of films (Fig. 3.) were determined[5] from load-displacement curves obtained by nanoindentation measurements. A microscratch tester was employed to characterize film adhesion. The scratch test involves drawing a stylus over the film under increasing normal loads and the value of the load at which adhesion failure is detected is known as the critical load (Fig. 4.). As evident from Fig. 3. and 4., the magnitude of selected mechanical properties could be controlled by power in case of the pp-films.

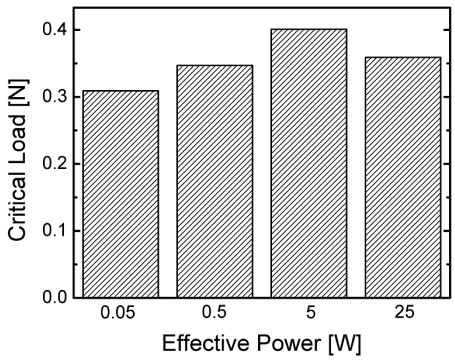

Fig. 4. **Critical load as a measure of adhesion bond between the pp-film and the glass substrate**

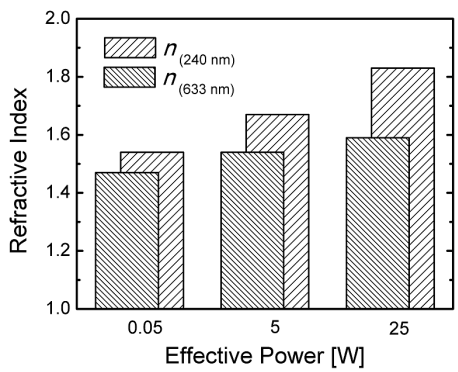

Fig. 5. **Refractive index at wavelengths of 240 and 633 nm as a function of the effective power**

A spectroscopic phase-modulated ellipsometer was used to characterize optical constants of pp-films in the spectral range 240–830 nm. A model of a single homogeneous film on the semi-infinite silicon substrate was used for the calculation of the film thickness, refractive index and extinction coefficient. Similarly to mechanical properties, the refractive index of pp-film was a function of the power (Fig. 5.).

Technological progress

Experience with preparation of high quality thin films of controlled physicochemical properties led us to development of a novel plasma reactor during the past years (2002–2004). The capacitive coupling plasma system (Fig. 6.) is aimed at preparation of functionally nanostructured thin films of high reproducibility. The internal setup of the deposition chamber, using plan-parallel electrodes, was derived from a typical capacitive coupling system, but our apparatus of new creative design was equipped with many non-standard components. A special construction of bottom rotary electrode (ø 114 mm) enabled us to stick in/out samples into/from the chamber under vacuum, and so without reactor contamination, using a magnetic drive (linear and rotary, BOC Edwards) and a special load lock mounted inside of differentially pumped side chamber. Next, the rotary electrode can be heated/cooled ranging from –100 to 300 °C and biased ranging from –500 V to +500 V. An upper electrode (ø 135 mm) of shower-type can be positioned in a distance of 20–60 mm from the bottom one. A movable substrate shutter can be used to deposit film at steady-state plasma conditions. An RF-generator (Cesar 1310, 13.56 MHz, 1000 W, Dressler) was connected to the system using an automatic matching network (VM 1000A, Dressler). It was possible to achieve a range of effective power density from $1 \cdot 10^{-4}$ to $4 \cdot 10^{0}$ W cm^{-3} ($1 \cdot 10^{-3}$ to $4 \cdot 10^{0}$ W cm^{-3}) using pulsed (continuous) plasma regime with respect to the movable top electrode. A turbomolecular pump (TMU 261 P, Pfeiffer Vacuum) with a dry scroll pump (TriScroll 300, Varian) as the first stage and an LN2-cooled trap were selected to evacuate the system in order to eliminate oil vapor, minimize a rest of water in all vacuum chambers and thus acquire the basic pressure ~ 10^{-6} Pa. Cleaning of the system, substrate pretreatment, and deposition process were automatized via control unit.

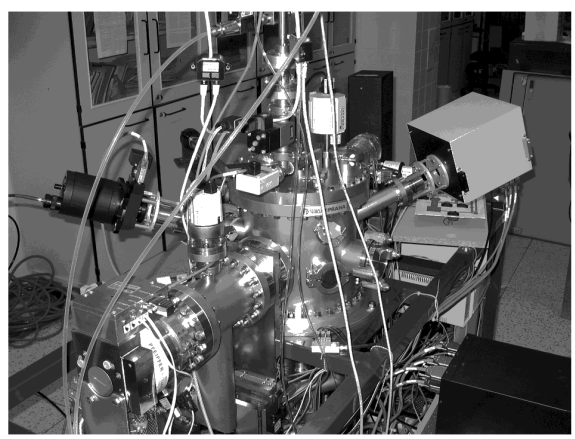

Fig. 6. **A real view of new technological apparatus**

The reactor was equipped by mass spectrometer (Process Gas Analyser HPR-30, Hiden Analytical), in-situ spectroscopic ellipsometer (UVISEL, Jobin Yvon), and optical emission spectrometer (Triax 550, Jobin Yvon) to monitor the plasma process and film growth. The in-situ ellipsometry enables analyses not only single layers but also multilayers[6–8] with respect to their thicknesses and optical constants. New numerical simulations enabled fast analyses of measured ellipsometric data corresponding to complex multilayer and gradient nanostructures. The optical constants of a newly grown ultrathin layer should be used as a feedback for the control of deposition conditions during a nanostructure growth. This is a new conception of a controlled plasma process (PE CVD).

Controlled deposition of the functionally nanostructured thin films is a new technological step for creative design and application of complex film systems in smart materials. Functionally gradient and/or multilayered nanostructured thin films of continuously or quasi-continuously varying physicochemical properties are worthwhile as compatible interlayers among distinct materials.

Conclusion

We would like to introduce plasma polymerization as a technique capable to prepare high quality thin films with high reproducibility. This level of technology could enable us to deal with more complicated film systems – multilayers and gradient films. In general, multilayer films can be prepared using the fabrication "bottom-up". Thus, a nanostructured film can be prepared as layer-by-layer, where the film thickness of a single layer could be only several tens of nanometers and single layers have to be bonded each other using strong chemical bonds. We could construct a functionally gradient nanostructured film "without" interfaces in one deposition if the plasma technology would be able to prepare film of continuously varying properties. Such a nanotechno-logy could be worth for formation of the controlled interphase in multicomponent materials, transparent nanostructured films of the varying refractive index – valuable as materials for optoelectronic applications, and functionally doped and hybrid layered structures for electronic devices.

The Czech Ministry of Education supported this work by contract No. MSM0021630501.

REFERENCES

1. Decher G., Schlenoff J. B. (Eds.): *Multilayer Thin Films*. Wiley-VCH, Weinheim 2003.
2. Jansen F.: Plasma-enhanced chemical vapor deposition. In *Handbook of Vacuum Science and Technology* (Hoffman D. M., Singh B., and Thomas J. H., Eds.), London, Academic Press, 1997.
3. Inagaki N.: *Plasma Surface Modification and Plasma Polymerization*, Lancaster, Technomic Publ., 1996.
4. Prikryl R., Salyk O., Vanek J., and Cech V.: Czech. J. Phys. *52*, D816 (2002).
5. Oliver W. C., Pharr G. M.: J. Mater. Res. *7*, 1564 (1992).
6. Valee C., Goullet A., Nicolazo F., Granier A., Turban G. J.: Non-Cryst. Solids *216*, 48 (1997).
7. Aumaille K., Vallee C., Granier A., Goullet A., Gaboriau F., Turban G., Thin Solid Films *359*, 188 (2000).
8. Spectroscopic Elipsometry (brochure), Jobin Yvon, Horiba Group (www.jyhoriba.com).

L03 TOUGHNESS OF FIBER/MATRIX INTERFACE FROM THE SINGLE-FIBER COMPOSITE TEST

JANA ZEISBERGEROVÁ and VLADIMÍR ČECH
Institute of Materials Chemistry, Brno University of Technology, Purkyňova 118, CZ-612 00 Brno, Czech Republic, xczeisbergerova@fch.vutbr.cz

Introduction

In recent years, experimental methods for measuring the adhesion between a rigid fiber and a more ductile polymer matrix have been progressively developed, and intensively investigated. Currently, several micromechanical techniques exist, such as the single-fiber composite (or fragmentation) test[1], the microbond test[2], the fiber pull-out test[3] and the microindentation test[4]. All of these involve complex interfacial stress states. However, simple force equilibrium, shear-lag, or elastic-plastic analyses are normally used to analyze the test results in terms of the stress transfer ability, a mechanical parameter usually loosely termed the interfacial shear strength (τ). Large differences for τ are obtained among the various experimental test results, as recently observed in an international range. This is so because the tests are different in nature: indeed, the loading configurations and the specimen geometries vary from test to test and therefore the stress fields induced locally are different. Despite the popularity of this approach and the large amount of experimental results obtained over the years, some investigators have suggested that τ may not be the critical factor governing fiber-matrix debonding, and that in the search for fracture criteria an energy-based theory is usually better approach than a theory based on the identification of a stress at a point.

Theory

The interfacial shear strength (τ) is possible determined by single-fiber fragmentation test. The model composite is tensile loaded and the matrix stress is transferred to the fiber by means the interface. When the tensile loading increases the fragmentation in fiber arises to the saturation. The fragments are short enough and the stress is inadequated for next fragmentation. The interfacial shear strength (τ) is determined by the mean fragment length and by the stress. The saturation arise by the high value model composite deformation. The general prerequisite is matrix elongation at break 3–4 times higher than reinforced fiber elongation. The interfacial shear strength and the toughness of interface is persuaded with respect to utility properties. The initial debonding length is used to determine the toughness of interface in model composite. This approach was invented by Wagner et al.[5]. The first fiber crack influenced by tensile loading is followed.

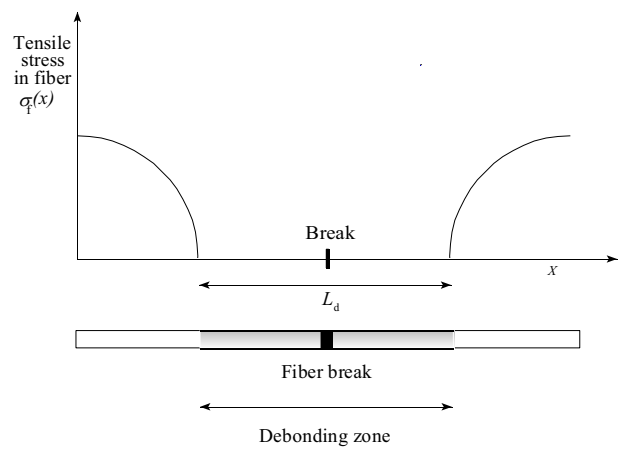

Fig. 1. **Isolated fiber break and associated initial interface debonding in fiber fragmentation experiment**

The fiber crack is accompanying by interface damage. The fracture energy as degree of toughness is constituted.

Wagner-Nairn-Detassis (WND) model: Consider a brittle, elastic, fiber embedded in a more ductile, elastic, polymeric matrix that can be considered as infinite in size (Fig. 1.). For simplicity, all pre-existing fiber stresses (such as residual thermal stresses) are neglected. A tensile stress pararellel to the fiber is applied to the composite, until the fiber breaks sequentially, from the weakest fiber defect to progressively less critical defects. Only the portion of such fiber fragmentation process that takes place in the linear elastic region of the composite test is considered. A fiber break is accompanied by simultaneous formation of an interface debonding zone, symmetrically on both sides of the fiber break site, as is often experimentally observed. The debonding length L_d is obtained from WND model:

$$L_d = \frac{2\sigma_f^2 r_f \left[\frac{1}{\beta} - \frac{\beta \cdot E_f r_f^2}{16 G_f}\right] - 2E_f r_f \Gamma_f}{4E_f \Gamma_i - r_f \sigma_f^2}, \quad (1)$$

where

$$\beta = \frac{1}{r_f}\sqrt{\frac{2G_m}{E_f \ln\left(\frac{R}{r_f}\right)}} \quad (2)$$

where r_f – radius of fiber, Γ_f – fiber fracture energy, E_f – the axial modulus of the fiber, G_f – axial shear modulus of the fiber, G_m – axial shear modulus of the matrix, R – the radius of the matrix over, which the stress is affected by the break event, σ_f – axial stress in the fiber.

Tailoring the Equation (1) is obtained interface fracture energy[5, 6].

$$\Gamma_i = \frac{\sigma_f^2 r_f}{2E_f L_d}\left[\frac{L_d}{2} + \frac{1}{\beta} - \frac{\beta E_f r_f^2}{16 G_f}\right] - \frac{r_f \Gamma_f}{2L_d} \quad (3)$$

Experiment

Material: The E-glass bundles (1200 tex) unsized and commercial 706 sized. The base of commercial 706 sizing is γ-methacryloxypropyltrimethoxysilane. The rovings were supplied by Saint-Gobain Vertex, Litomyšl, Czech republic. The diameter of the sized and unsized fibers was 19 μm. The surface of unsized fibers was modified by chemical wetting process using vinyltriethoxysilane (VTES, purity >98 %, Fluka). 0.5 cm^3 of VTES was hydrolyzed for 60 min in 99.5 cm^3 of deionized water using a magnetic stirrer. The aqueous solution was poured into a bath which is a part of automated apparatus for continuous surface modification of glass fiber bundles using the prepared solution. The surface modified bundles were dried at a temperature of 120 °C for 4 hours. The matrix material used in this study was unsaturated polyester resin VIAPAL VUP 4649E(M) (Vianova Kunstharz). The resin was mixed with hardener – styrene, low temperature iniciator – Perkadox 16, high temperature iniciator – Norpol 62, UV stabilizer and internal lubricant – INT-PUL24.

Preparation of specimens and measuring: A parallel single fiber was pasted in the center of silicone form (LUKOPREN) form for manufacturing of the model composite. The single fiber composite is used for tensile testing. The single fiber was embedded by the matrix. The specimens were dried for 24 hour by 145 °C. After cooling down followed taking out specimens from the forms and smoothing edge. The specimen was fixed to the tensile machine and set under objective the light polarizing microscope (Fig. 2.). When the embedded single fiber was found out the tensile stress was applied to the model composite. If the run of the tensile process was slow enough (qvasi-static) the precedence of the break matrix is ruled out. The measuring process was studied and scanned by microscope. An evaluation by image analysis (AnalySIS) was followed. When the fiber broke the measuring process was finished. The debonding length was evaluated by image analysis. The measurement error on the debonding lengths was estimated to the 1–2 μm (ref.[7]).

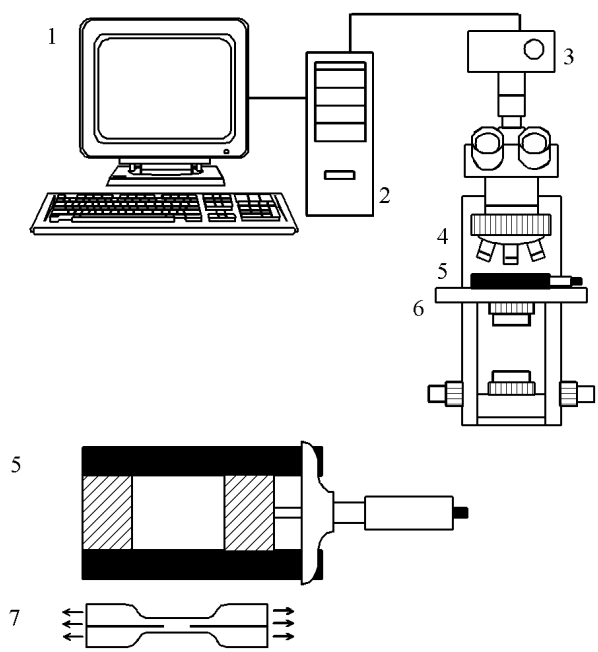

Fig. 2. **The scheme of measuring machine: 1 – PC monitor, 2 – PC, 3– digital camera, 4 – microscope objectives, 5 – loading device, 6 – XY translation stage, 7 – single fiber specimen**

Results and discussion

A typical plot showing the dependence between the initial debonding length and the elongation of model composite for unsized and two types of sizing on the fibers is presented in Fig. 3.

The range of elongation is between 2.2–4.2 % for all types E-glass fibers. The scattering of measured data is evident. It is hardly to find functional dependence between initial debonding length and elongation for individual sizing.

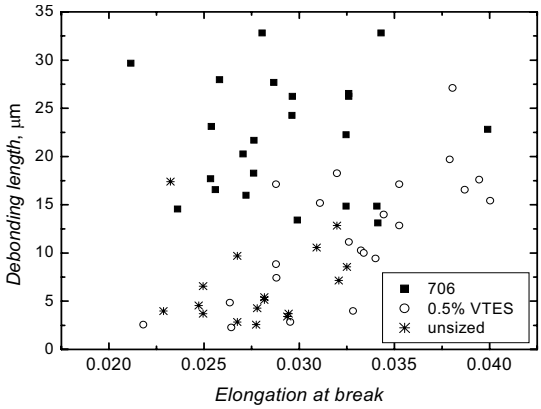

Fig. 3. **Dependence of initial debonding length on the elongation of model composite**

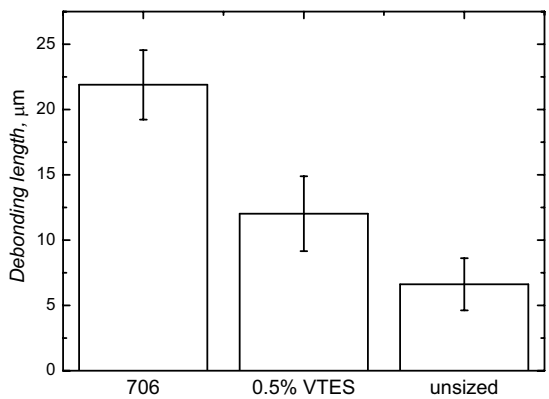

Fig. 4. **Dependence of the mean value of initial debonding length for different fiber sizing**

For initial debonding length is obvious that 706 sizing extends to high value than unsized fiber and fiber with 0.5 % VTES sizing. The average values of initial debonding length and directive deviation for different sizing were evaluated. The results are compared in Fig. 4.

The average value of initial debonding length is evidently different for three types of sizing. The tensile stress of model composites and individual fibers were measured by tensile machine Zwick Z010/TH2A. The mean value of Young's modulus was assessed by analysis of tensile curves for individual fibers. The Young′s modulus E_f is presented in the Table I. The Young′s modulus of the matrix E_m was determined from tensile curves of the model composites (Table I). The tensile curve could be utilized for the conversion of relating elongation from the single fiber fragmentation test for the fiber stress σ_f. The instantaneous fiber stress $\sigma_f = \sigma_m E_f/E_m$ (where σ_m is the matrix or composite applied stress), could be calculated. The initial debonding length is indirectly proportional interface fracture energy which is characteristic for interface toughness. According to Fig. 4. the interface toughness come up to the highest value for unsized fibers and the lowest value show fibers with commercial 706 sizing. The toughness of interface for 0.5% VTES is between unsized and commercially sized fibers. The initial debonding zone for 706 sizing and unsized fiber is represented in Fig. 5., 6. Fig. 5. and 6. are typical examples for used sizings.

Table I
The numerical values of the parameters used in Equation 3

Parameter	E-glass fiber	Polyester resin
fracture energy, J m^{-2}	10	
radius of matrix over, μm		R = 4 r_f
radius of fiber, μm	10	
Young's modulus, GPa	5.24	68

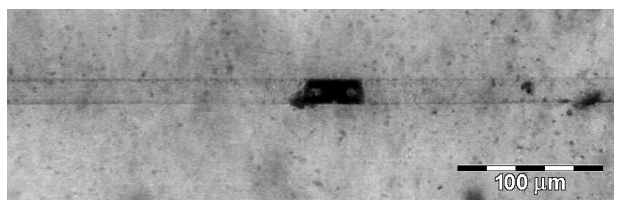

Fig. 5. **The example of fiber break for 706 sizing**

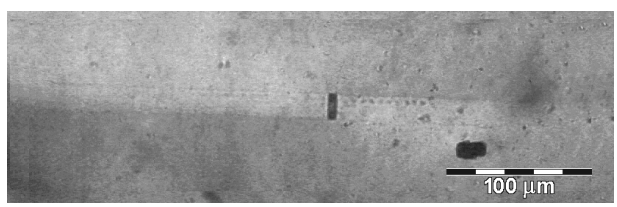

Fig. 6. **The example of fiber break for unsized fiber**

The WND model which follows previous energy-based theories[8–12] is supposed to be right in principle. Despite of the careful specimen preparation the dispersion of measured data is too great (Fig. 3.). This could be cause by significant initial stress when the model composite is fixed to the tensile machine and further by non homogenity in model composite.

The experimental data were evaluated using Eq. 3 in order to give a rough estimation of the fracture energy which could be compared among different sizing. The mean value of the interface fracture energy is shown in the Fig. 7. The used parameters are shown in Table I (ref.[6,8]).

Conclusion

We have studied the toughness of interface in composite system glass fiber/polyester matrix composite using fragmentation test. The unsized, commercial 706 sized and 0.5% VTES sized E-glass fibers were used in our study. The model composites were tested under tensile loading. The initial debonding zone was observed by light polarizing microscope and analysed by image analysis. The *Wagner-Nairn-Detassis*

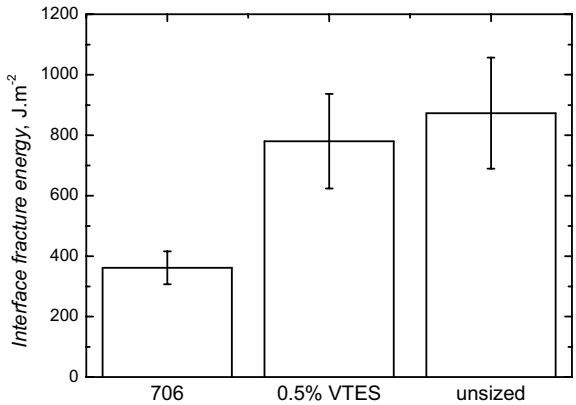

Fig. 7. **Dependence of mean value of interface fracture energy for different sizing**

model for an evaluation of experimental data. According to qualitative analySIS, the toughness of interface reached the highest value in case of unsized fibers and the lowest value in case of commercial sized fibers.

The authors express their thanks to M. Sirový and Saint--Gobain Vertex for providing glass fibers. This research was supported by grant no. MSM0021630501 (Czech Ministry of Education).

REFERENCES:

1. Drzal L. T., Herrera-Franco P. J., Ho H.: *Comprehensive Composite Materials 5*, Elsevier Science Ltd. 2000.
2. Miller B., Muri P., Rebenfeld L.: Composites Science and Technology *28*, 17 (1987).
3. Piggott M. R., Chua P. S., Andison D.: Polymer Composites *6*, 242 (1985).
4. Mandell J. F., Grande D. H., Tsiang T. H., McGarry F. J.: *87*, ASTM STP 893 (1986).
5. Wagner H. D., Nairn J. A., Detassis M.: Applied Composite Materials *2*, 107 (1995).
6. Yallee R. B., Young R. J.: Composites Science and Technology *58*, 1907 (1998).
7. Zhou X. F., Nairn J. A., Wagner H. D.: Composites: Part A *30*, 1387 (1999).
8. Outwater J. O., Murphy M. C.: Modern Plastics, *160* (1970).
9. Mullin J. V., Berry J. M., Gatti A., Journal of Composite Materials *2*, 82 (1968).
10. Mullin J. V., Mazzio V. F. (NASA): NASw-2093 (1971).
11. Piggott M. R.: Composites Science and Technology *30*, 295 (1987).
12. DiBenedetto A. T.: Composites Science and Technology *42*, 103 (1991).

L04 LIVING POLYMERIZATION OF OLEFINS INITIATED BY NICKEL CATALYSTS

JAN MERNA[a], SONA HERMANOVA[a], JAROSLAV CIHLAR[a], MILOSLAV KUCERA[a], HENRI CRAMAIL[b] and ALAN DEFFIEUX[b]
[a]*Institute of Materials Chemistry, Brno University of Technology, Purkynova 118, 612 00 Brno, Czech Republic, merna@fch.vutbr.cz,* [b]*Laboratoire de Chimie des Polymčres Organiques, UMR 5629, ENSCPB, CNRS, Université Bordeaux I, Avenue Pey Berland, B.P. 108, 33402 Talence Cedex – France*

Introduction

The discovery of late transition metal catalysts capable to polymerize olefins in the mid 90's arose intensive industrial and academic research1. Interesting subgroup of this family are nickel and palladium diimine complexes first reported by Brookhart in 1995 (ref.[2]). One feature of such catalysts is a migration of metal center through the last incorporated monomer unit (chain-walking mechanism) producing polyolefins with unusual branching topology[3]. Moreover these catalysts can promote living-like polymerization of olefins[4, 5]. In original Brookhart study[4] only **Ni2a** and **Ni2b** complexes (Fig. 1.) activated by methylalumoxane (MAO) were claimed to be active as living polymerization catalysts in higher olefin polymerization. In this work we report for the first time on the livingness of polymerization of hex-1-ene (C6) initiated by other two nickel catalysts **Ni2c** and a **Ni2e** (Fig. 1.).

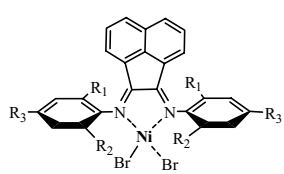

Ni2a: R_1=R_2=iPr, R_3=H
Ni2b: R_1= t-Bu, R_2=R_3=H
Ni2c: R_1=R_2=R_3= Me

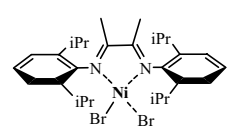

Ni2e

Fig. 1. **Nickel diimine complexes used in the study of living olefin polymerization**

Experimental

Materials. All manipulations with air-sensitive compounds were done by standard Schlenk techniques under dry nitrogen. Hex-1-ene (Aldrich) was passed through a column of basic alumina and dried over trihexylaluminium. Chlorobenzene was dried over P_4O_{10}. All the monomers and solvents were distilled under reduced pressure before use. MAO (10 wt % solution in toluene) was purchased from Crompton and used as such. Nickel initiators were prepared according to literature procedures[4, 6] and used as a solution in chlorobenzene. Both catalyst and MAO solutions were stored at 5 °C.

Analytical techniques. ^{1}H and ^{13}C NMR spectra of polymers were obtained on 400 MHz Bruker Avance spectro-

meter in $CDCl_3$ solution at 25 °C. Molar masses were determined on Varian size exclusion chromatograph equipped with four TSK Gel G columns and RI detector at 25 °C in THF solution (3 mg/ml THF) at an elution rate of 0.8 ml min^{-1} against PS standards. DSC analyses were performed on a Perkin Elmer DSC 7 instrument using 10 °C min^{-1} heating rate after second heating cycle. UV-VIS spectra were recorded on a Varian carry 3E spectrometer. A quartz cell (0.5 cm optical length) connected directly to glass reactor was used for measurements.

Polymerization procedure. Kinetics of polymerization was followed by dilatometry. 15 ml dilatometer equipped with a PTFE valve was loaded with catalyst solution, monomer, solvent and cooled 20 min in bath at –10 °C. Polymerization was started by addition of MAO solution. After a given reaction time the polymerization mixture was precipitated into 200 cm^3 of acidified methanol. Polymer was decanted and dried under vacuum to constant weight. The other polymerizations were done in Schlenk tubes according analogous procedure. UV-visible measurements are described elsewhere[7].

Results and discussion

Polymerization of hex-1-ene initiated by four nickel complexes **Ni2a–c**, **e** activated by MAO (Al/Ni = 200) in chlorobenzene was studied. The influence of temperature and monomer concentration on monomer conversion, poly(hex-1-ene) molar mass and microstructure was examined and results are summarized in Table I.

Living-like character of hex-1-ene polymerization, as previously reported by Brookhart for **Ni2a** and **Ni2b** complexes, was observed for the first time also for complexes **Ni2c** and **Ni2e** in the temperature range from –10 to 25 °C and monomer concentration 0.8 M or lower.

Interestingly it seems that the bulkiness of ortho substituents of fenyl rings is not so crucial as seen from very narrow molar mass distribution of polyhexen prepared by **Ni2c** bearing only small methyl groups. On the example of **Ni2e** it is demonstrated that also the effect of backbone diimine substituents (1,8-nafalendiyl for **Ni2a** and methyl for **Ni2e**) is not very significant. Thus, it is probable that there exists much wider spectrum of diimine ligands that can sufficiently hinder Ni center against the monomer transfer reaction. Complexes **Ni2a** and **Ni2e** with bulky isopropyl groups in ortho positions

Table I
Effect of temperature and monomer concentration on hex-1-ene polymerization initiated by nickel diimine complexes **Ni2a–c, e** activated by MAO

Vz.	Precursor	[C6] [mol dm^{-3}]	T_p [°C]	Conversion [%]	M_n^a [kg mol^{-1}]	D^a	M_n^{exp}/M_n^{th}
1	**Ni2a**	0.2	–10	93	27,8	1.08	1.9
2		0.8	–10	100	93,3	1.05	1.4
3		3.2	–10	73[c]	223,9	1.09	1.3
4		0.8	0	100[d]	96,5	1.04	1.5
5		0.8	25	100[c]	104,3	1.05	1.5
6	**Ni2b**	0.2	–10	80	33.0	1.05	2.5
7		0.8	–10	93	121.0	1.07	1.9
8		3.2	–10	85	301.2	1.30	1.3
9		0.8	25	100	122.3	1.13	1.7
10	**Ni2c**	0.2	–10	96	30.9	1.09	1.9
11		0.8	–10	100	95.4	1.12	1.3
12		3.2	–10	100	174.1	1.61	–
13		0.8	0	100	92.2	1.15	1.2
14		0.8	25	100	79.2	1.26	1.0
15	**Ni2e**	0.2	–10	66	24.6	1.14	2.2
16		0.8	–10	78	88.7	1.06	1.7
17		3.2	–10	59	232.5	1.10	1.5
18		0.8	25	100	165.5	1.08	2.3

[Ni] = 1.0 M, [Al] = 0.20 M, time of polymerization 5 h, Tp = –10 °C, total volume 10–40 cm^3.
[a]Molar mass and disperzity (Mw/Mn) determined by SEC against PS standards
[b]Number of branches per 1000 °C atoms determined by ^1H NMR spectroscopy
[c]Time of polymerization 1 h
[d]Time of polymerization 2 h

displayed narrow molar mass distribution even at such high monomer concentration as 3.2 M (monomer/initiator ratio is 3200) indicating extremely high resistance of catalyst to transfer to monomer.

On the basis of conversion and monomer/initiator ratio it can be calculated theoretical value of molar mass. The difference of calculated (M_n^{th}) and experimental (M_n^{exp}) molar mass values reveals incomplete activation of all Ni precursors by MAO observed previously by UV-VIS spectroscopy[8]. The true livingness of polymerization was demonstrated for Ni2a/MAO also by the possibility to reinitiate the chain growth by addition of monomer after complete consumption of first monomer feed (Fig. 2.).

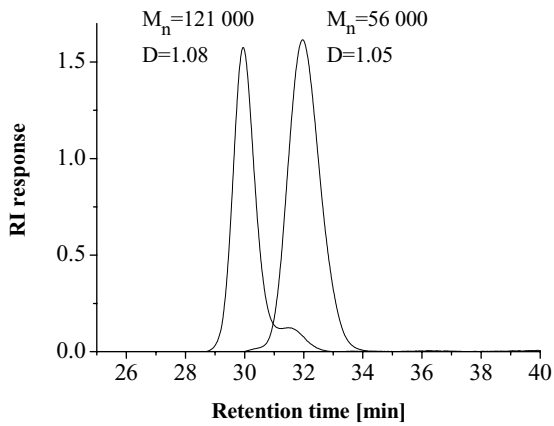

Fig. 2. **SEC chromatograms of poly(hex-1-ene) after first (right) and second (left) monomer addition, [Ni] = 1 mM, Al/Ni = 200, 0 °C, chlorobenzene**

The molar mass of poly(hex-1-ene) was doubled while its distribution remained narrow. Low molar mass shoulder in second chromatogram is caused by impurities in monomer that deactivated small (less than 5 %) amount of growing centers. Another proof of livingness is the linear dependence of molar mass on monomer conversion depicted in Fig. 3.

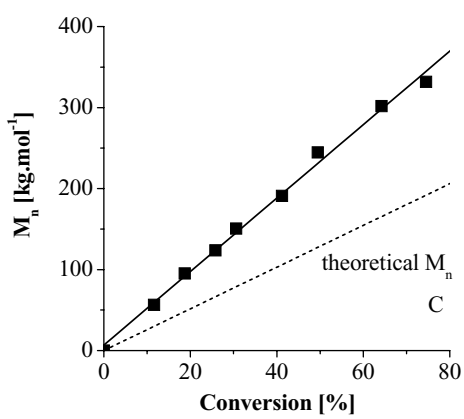

Fig. 3. **Dependence of molar mass on monomer conversion for hex-1-ene polymerization initiated by** Ni2a/**MAO at 0 °C in chlorobenzene, [C6] = 0.8 M, [Ni] = 0.25 mM, Al/Ni = 200, 4 h**

Kinetic study. Kinetics of hex-1-ene polymerization activated by Ni2a/MAO was investigated at –10 °C in chlorobenzene. Attention was paid to unusual kinetic behavior reported previously by Peruch[8] and Souza[9] when the polymerization rate decreased with monomer concentration. Results are shown in Fig. 4.

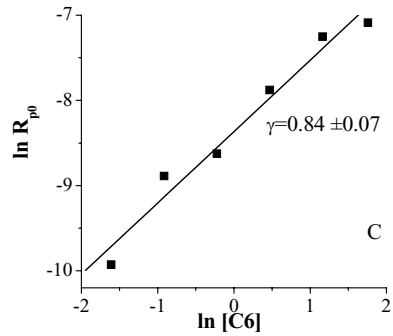

Fig. 4. **Logarithmic variation of initial polymerization rate on monomer concentration during hex-1-ene polymerization initiated by Ni2a/MAO at –10 °C in chlorobenzene, [Ni] = 1 mM, Al/Ni = 200, [C6] = 0.2–5.8 M.**

Hex-1-ene polymerization shows first internal order kinetics with respect to monomer concentration. As can be seen from Fig. 4. there is no decrease of polymerization rate in the whole range of hex-1-ene concentration, but external monomer order is decreased to value approx. 0.8. Explanation of this result is based on the following reaction mechanism (Fig. 5.).

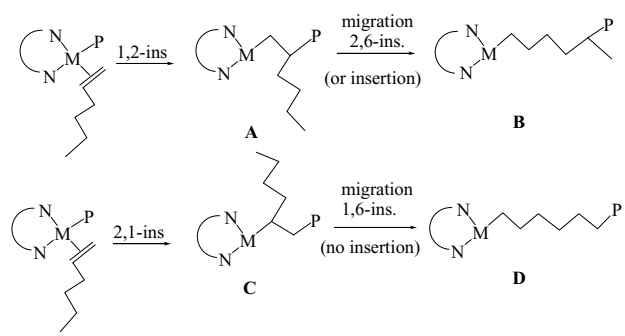

Fig. 5. **Proposed mechanism of formation of active centers with different reactivity during hex-1-ene polymerization initiated by nickel diimine catalyst**

Metal migration following either 1,2- or 2,1-insertion leads to the formation of species B and D that were suggested to be more reactive towards monomer insertion than specie A, arising from 1,2-insertion, and C, issued from 2,1-insertion which can not insert a new monomer molecule. At high monomer concentration, monomer insertion is favored and the migration extent is decreased. Therefore the relative concentration of more reactive species B and D is reduced. The consequence of that is a decrease of polymerization rate with increase of monomer concentration.

Relation between poly(hex-1-ene) microstructure and kinetics. Different poly(hex-1-ene) microstructure should be observed with respect to the monomer concentration as interpreted from kinetic data. Normal 1,2-insertion of C6 produces polymer with 167 methyl groups per 1000 °C atoms (1 methyl per monomer unit). In both cases we observed significantly lower methyl branch content as a consequence of 2,1-insertion followed by chain walking, producing linear polyethylene sequences (D). As it is shown in Fig. 6., ^{1}H NMR analysis confirms the branching decrease with a decrease of monomer concentration.

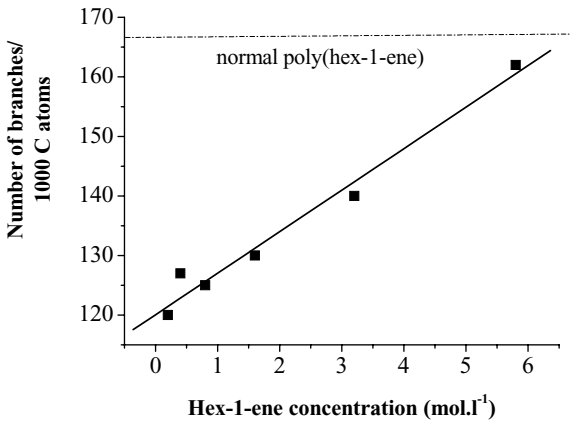

Fig. 6. **Dependence of branching of poly(hex-1-ene) on initial monomer concentration, [Ni] = 1 mM, Al/Ni = 200, 0.2 < [C6] < 5.8 M, determined by ^{1}H NMR**

Conclusion

Living-like polymerization behavior was observed for nickel complexes **Ni2c** and **Ni2e** for the first time. Living polymerization of **Ni2a** was further proofed by the ability of active centers to restart the polymer growth after second monomer addition and by linear dependence of molar mass on the monomer conversion. All nickel complexes treated by MAO were activated incompletely, therefore the discrepancies between predicted and measured molar masses of poly(hex-1-enes) were observed. Hex-1-ene polymerization kinetics was followed by dilatometry. External monomer order was found to be around 0.8 as a consequence of formation of two types of growing centers with different reactivity whose ratio is dependent on monomer concentration. Proposed mechanism was confirmed by correspondence of kinetics with the change in polymer microstructure observed by ^{1}H NMR spectroscopy.

This work was supported by EU project COST D17.10 and project MSM0021630501 of the Ministry of Education, Youth and Sports of the Czech Republic.

REFERENCES

1. Ittel S. D., Johnson L. K., Brookhart M.: Chem. Rev. *100*, 1169 (2000).
2. Johnson L. K., Killian C. M., Brookhart M.: J. Am. Chem. Soc. *117*, 6414 (1995).
3. Guan Z., Cotts P. M., McCord E. F., McLain S. J.: Science *283*, 2059 (1999).
4. Killian C. M., Tempel D. J., Johnson L. K., Brookhart M.: J. Am. Chem. Soc. *118*, 11664 (1996).
5. Gottfried A. C., Brookhart M.: Macromolecules *36*, 3085 (2003).
6. Maldanis R. J., Wood J. S., Chandrasekaran A., Rausch M. D., Chien J. C. W.: J. Organomet. Chem. *645*, 158 (2002).
7. Coevoet D., Cramail H., Deffieux A.: Macromol. Chem. Phys. *199*, 1459 (1998).
8. Peruch F., Cramail H., Defieux A.: Macromolecules *32*, 7977 (1999).
9. Simon L. C., Williams C. P., Soares J. B. P., Souza R. F.: J. Mol. Cat. A: Chemical *165*, 55 (2001).

L05 SYNTHESIS OF UV CURABLE PVA MACROMERS FOR INK RECEIVING SUBSTRATES

PETR DZIK and MICHAL VESELÝ
Faculty of chemistry, Brno University of Technology, Purkyňova 118, 612 00 Brno, Czech Republic, petr@dzik.cz

Introduction

Since the marketing of polyvinyl alcohol (PVA) in the 30's of last century, it has found a great plethora of applications in very many different industrial fields. Its hydrophility and solubility in water proved to be the key properties that are exploited with a great success in most its applications.

As specially modified grades of PVA were being introduced, they were succefully used in many small-scale highly specialized technologies. Examples include PVA fiber, laminating films for safety glass, special purpose inkjet printing media, CRT phosphor slurry, membranes, gels for bioengineering applications etc. Although these high-tech applications require relatively small amounts of PVA and/or its derivatives, they are of a great importance – because of the very special functions they are able to perform and also, from the economic point of view, because of the high added value.

As far as the photoreactive PVA systems based on PVA are concerned, these found numerous applications as well. Their importance has been gradually growing as our environmental awareness induces pressure on the manufacturers to implement more environment-friendly technologies. PVA is an excellent material for this purpose. Advanced imaging systems based on PVA can be developed with pure water and produced waste does not represent toxicological problem. Lately, PVA good biocompatibility together with the advances of medicine and bioengineering opened a new area for its utilization. PVA proved to be excellent material for medical

implants as well as biotechnological carrier. It seems that it is just the biotechnology and bioengineering field where we can expect further surprising developments.

Apart from the rapidly developing area of photoreactive systems based on PVA mentioned above, there is also one recently found application of PVA – the inkjet printing substrates. As inkjet printers have become common in homes and offices and their print quality approaches that of traditional silver halide photography, the demand for high-end photorealistic inkjet printing papers rose as well.

Experimental aims

In our research work, we would like to study the possible utilization of the PVA photoreactive derivatives special functionality for the design of special inkjet printing substrates. We strive to develop a "smart" photoreactive ink-receiving layer. We seek the preparation of a suitable, highly hydrophilic polymeric layer, which would:

Have suitable surface energy characteristics, determining the behavior of the ink drop during the very first few moments of ink-surface interaction.

Absorb large amount of deposited ink without deteriorating deformation to the image raster points.

Effectively drain the solvent away, leaving the colorant untransported.

Be able to freely evaporate the solvent.

Be susceptible to photochemically induced cross-linking by radical cross-polymerization. This photochemically induced process would preferably perform the following functions: fix the colorant agent in the layer, make the layer water repellent and provide mechanical durability and archival stability.

In order to perform the projected functions, we plan to modify PVA of different grades of hydrolysis by polymer-analogous reaction. Our approach is based on the idea of introducing photoreactive lateral groups to the backbone macromolecule of receiving layer-forming polymer. Upon the modification, pendant groups containing activated unsaturated bonds will be attached to the linear PVA backbone macromolecule. In this way, water-soluble multifunctional PVA macromer will be prepared.

This macromer can then be used pure or together in mixture with different macromers and other additives to prepare ink-receiving layer. The layer will be carried on an inert support for experimental purposes, but compatibility with a wide scale of applicable supports is expected. The layer should provide premium quality when printed in an inkjet printer. Then, the layer could be fixed by UV curing: upon exposure to actinic light the layer would crosspolymerize, and this process will bring the sought changes in the layer properties: ink fixation and improved resistance.

To prepare the projected PVA macromers bearing pendant unsaturated groups, several modifying agents and synthetic routes are applicable. In this report the authors would like to review the synthethic routes of 3 common examples of cross-polymerisable PVA macromers synthetised from simple precursors and compare the properties of prepared products.

Experimental

Maleinated PVA: PVA (Mowiol 10–98, 20 g, app. 0.5 mol monomeric units) is dissolved in anhydrous dimethylformamide (DMF, 200 ml) at 70 °C, and maleic anhydride (2–10 g) and the catalyst dimethylaminopyridine (1 w % of maleic anhydride) is added. The mixture is stirred at 70 °C for 1 hour and then it is let to cool down to ambient temperature. The product is then precipitated by pouring into 400 ml of acetone. Modified polymer is separated by filtration on a polyester mesh, washed twice with ethanol and dried to constant weight at 50 °C.

Methacrylated PVA: 80 ml of water, 0.3 mol acetic acid and 0.3 mol methacrylic acid are stirred in a beaker in water bath at 40 °C. To this mixture, PVA (20 g) is added in small amounts over the course of 8 hours, until a clear viscous solution is obtained. The mixture is then stirred for another 36 hours. The product is then precipitated by pouring into 400 ml of acetone. Modified polymer is separated by filtration on a polyester mesh, washed twice with ethanol and dried to constant weight at 50 °C.

Glycidylmethacrylated PVA: PVA (20 g) is dissolved in a mixed solvent consisting of 100 ml DMFA and 50 DMSO at 70 °C. After complete dissolution, 0.1 to 20 ml of glycidylmethacrylate (GMA) is slowly added drop-wise, so that the polymer would not precipitate. Then, 5 ml of methanolic solution of KOH (5 w %) is added in the same manner. During the course of reaction, the mixture turns yellow to even brownish depending on the content of GMA and a smell of methacrylate is present. The reaction mixture is stirred at 70 °C for 2 hours and then it is let to cool down to ambient temperature. The product is then precipitated by pouring into 400 ml of acetone. Modified polymer is separated by filtration on a polyester mesh, washed twice with ethanol and dried to constant weight at 50 °C.

Prepared modified polymers were used for further study to evaluate their suitability for the projected purpose, i. e. ink receiving layers. To do so, they were characterized by numerous analytical methods including, but not limited to infrared and UV spectroscopy, surface characterization by dynamic contact angle measurement, photoresist speed determination, thermal analysis, swelling kinetics study, gravimetric determination of volatile/soluble/network fraction and others. With respect to the limited space for this paper, the characterization methods cannot be described in details.

Results and discussion

Maleic anhydride was actually the first modifying agent we have been experimenting with. For maleinization of PVA, the esterification reaction catalyzed by dimethylaminopyridine is the preferable synthetic route[1]. Catalysed reaction mixture will reach equlibrium within 1 hour, whereas non-catalysed will take app. 6 hour. In both cases, even if excess

of maleic anhydride is used, the conversion degree will not rise over 10 molar % relatively to OH content.

Maleinized PVA shows several interesting properties. The carboxyl group present at the end of the lateral group effectively increases surface energy, contributing to a good wetting of the receiver by the ink. Also, the hydroxyl groups present there provide the option for cross-linking of adjacent macromolecules via ester bonding. In this way, a hydrophilic xerogel of varying cross-link density can be prepared by heat-curing. And finally, the activated carbon-carbon double bond can be cross-polymerized, resulting into insoluble, low--swelling xerogel.

Well, the maleinized PVA has also some drawbacks, such as low aqueous solubility at higher conversion degrees and very low crosslinking sensitivity, resulting into unacceptably long exposure times. Anyway, it has showed us a possible way in the ink receiving layer design. In order to overcome its limitations, we have been experimenting with other compounds that might be suitable for the introduction of activated double bond to the PVA backbone macromolecule.

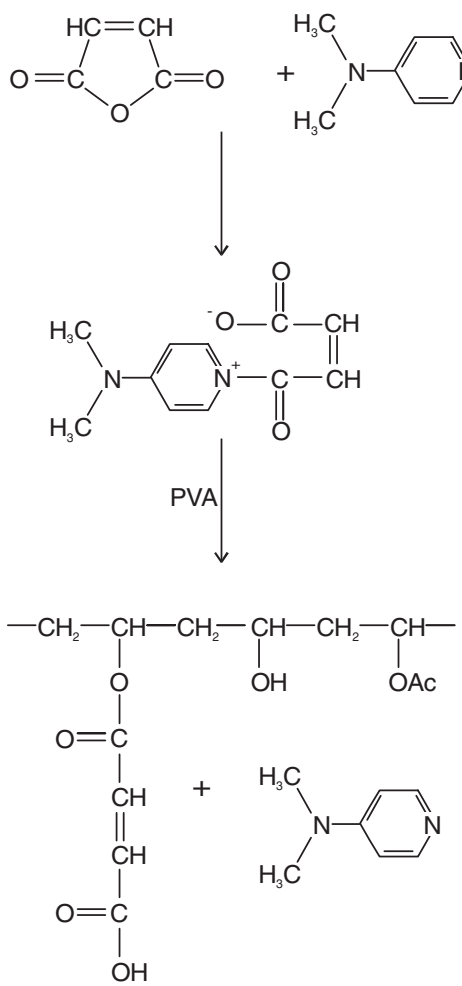

Fig. 1. **Maleinization of PVA**

Acrylic acid and/or methacrylic acids are important monomers and monomer precursors for a number of industrial processes. PVA with pendant (meth)acrylate groups was proved to be readily crosspolymerized. However, the esterification reaction of PVA is rather tricky. It might seem that the (meth)acrylic esters of PVA could have been readily prepared by an esterification reaction with some reactive (meth)acrylating agents, such as (meth)acryloyl chloride. However, attempts to do so were unsucceful[2]. Therefore, the polymer-analogous equilibrium reaction with acrylic or methacrylic acid is the preferred method[3], although the difficult PVA dissolving and slow equilibrium establishment represent significant technological challenges. The product, poly(vinyl alcohol)-co-(vinyl (meth)acrylate), is a water soluble polymer containing varying number of (meth)acrylate units.

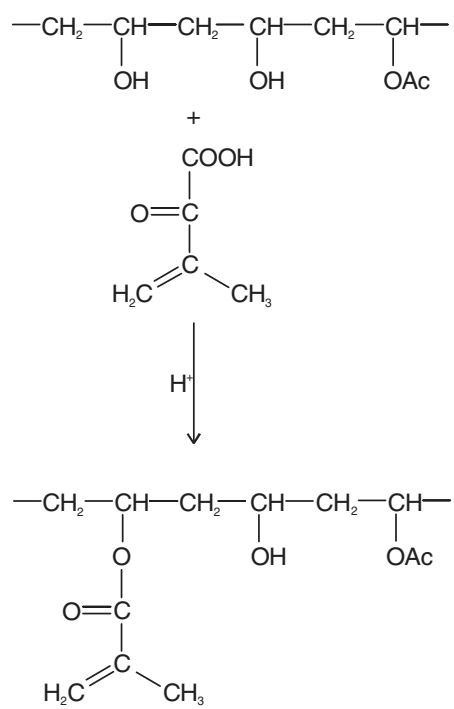

Fig. 2. **Esterification of PVA by methacrylic acid**

The conversion degree obtained is relatively low (app. 2 molar %) as there is quite a narrow solubility "window" in the composition of reaction mixture. Greater changes in the reaction mixture composition will prevent PVA from dissolving. Although the photochemical sensitivity is good, the low conversion degree leads into a low crosslink density of resulting polymeric network. Therefore the crosslinked polymer swells much, contains large soluble fraction and swollen gel shows poor mechanical properties.

Glycidyl methacrylate (GMA) is a unique compound because of its double functionality. Apart from the activated carbon-carbon double bond of methacrylate, it also contains highly reactive epoxy groups. Therefore it is capable to poly-

merize via both radical and cationic way. For the purpose of PVA modification, the epoxy group is used for attaching the moiety to PVA backbone while the acrylate is left intact to be ready for radical crosspolymerization.

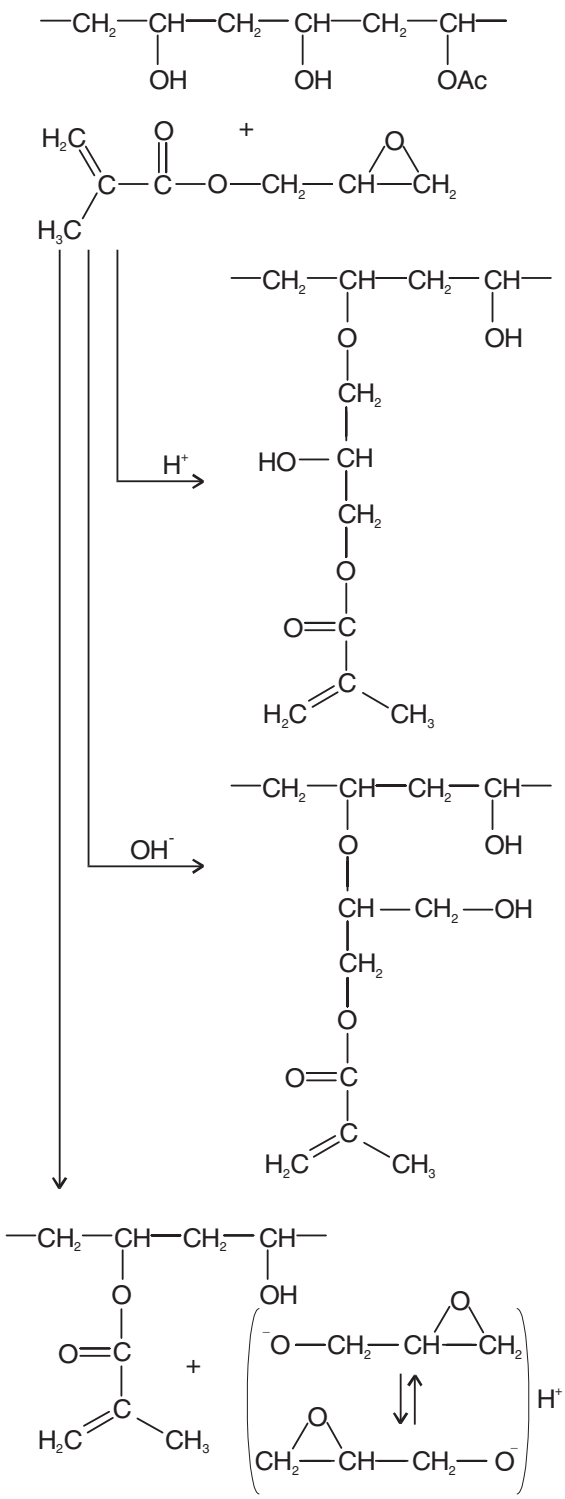

Fig. 3. **Reactions of PVA with GMA**

The reaction path of GMA is somewhat more complex than it might seem. The strained expoxide ring can be opened either by acidic or basic catalysis[4]. During the course of an acid-catalysed ring opening, the nucleophile attacks the more substituted carbon atom of epoxide group primarily. On the other hand, during the course of base-catalysed ring opening, the alkoxy anion attacks the less substituted carbon atom of epoxide group more preferably. But this is not the end to the peculiarities. If the reaction is carried out in neutral conditions with the aid of a catalyst (dimethylaminopyridine), a completely different behavior is observed[2,5].

In this case, the mild reaction conditions leave the epoxy ring untouched and glycidylmethacrylate undergoes transterification – glycidol is a good leaving group, since the glycidol anion is stabilized by charge delocalization over the two oxygen atoms. Therefore under these conditions PVA is esterified by methacrylic moiety and free glycidol can be detected in the reaction mixture. Despite the tangled reaction routes of PVA and GMA, the products have been intensively studied for the purpose of bioengineering applications[6].

For our purposes, we have chosen the basic catalytic route. Under these conditions, the reaction proceeds almost quantitatively and the conversion degree is easily adjusted by the modifying agent dosage. Methacrylated PVA has very interesting surface properties. GMA is essentially hydrophobic, leading to a lower surface energy and hydrophobization of modified polymer. On the other hand, it is highly susceptible to photoinitiated cross-polymerization, and the effective photographic speed of this compound is much higher than that of the maleinized PVA. The hydrophobic nature of modified PVA is highly dependent on the conversion degree. This can be clearly illustrated by the changing value of water droplet contact angle. Pure PVA has CA value of approximately 65°. As the content of methacrylate increases, so does the CA and reaches a value of 100° for PVA containing 20 molar % of methacrylate. Another very interesting phenomenon can be observed after exposure to UV. The CA significantly decreases, which can be explained by the combined effect of two processes: the highly non-polar double bonds are cleaved by cross-polymerization and during this reaction oxygen is incorporated into the layer, making it ever more hydrophilic.

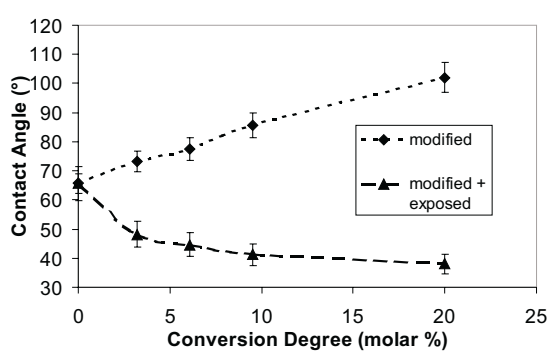

Fig. 4. **The influence of GMA content in PVA on surface properties**

Conclusion

Our test proved that all the three prepared modified grades of PVA are able to perform the projected functions:

Pendant unsaturated groups are attached to the PVA backbone during the modification reactions.

Modified grades of PVA are compatible with water-based inks.

Modified grades of PVA are susceptible to cross-polymerization and the prints can be fixed in this way.

However, all three types of modified PVA have significant drawbacks that were discovered by our detailed investigation. PVA modified by maleic anhydride has prohibitively low crosslinking speed. PVA modified by methacrylic acid has very good photochemical performance, but the properties of resulting network are poor because of limited crosslink density dues to low conversion degrees. Finally, PVA modified by GMA seems to be nearly perfect: conversion degree is easily adjusted and modified PVA has good photochemical performance. Unfortunately, the surface properties vary greatly with the conversion degree and higher conversions have unsuitably high value of contact angle.

Our study proved that each of these simple modifying agents induces some unsuitable property to the modified product. In order to fulfill all the projected functions, more sophisticated modifying agents have to be used. Our team is currently experimenting with advanced methacrylating agents based on (meth)acryloyl-(alkyl)amino-alkylaldehyde dimethyl acetals, which we believe will perform much better than the simple modifying agents reviewed in this report.

REFERENCES

1. Sánches-Chaves M., Arranz F., Cortazar M.: *Polymer*, *39*, 2751 (1998).
2. van Dijk-Wolthius W. N. E., Kettenes-van den Bosh J. J., van der Kerck-van Hoof A., Hennink W. E.: *Macromolecules*, *30*, 3411 (1997).
3. Mühlebach A., Müller B., Pharisa C., Hofmann M., Guerry D.: *Journal of Polymer Science: Part A: Polymer Chemistry, 35*, 3603 (1997).
4. Solomons, T. W. G.: *Organic Chemistry*. 6th edition, New York: John Wiley & Sons, Inc., 1996, pp. 450–451.
5. van Dijk-Wolthius, W. N. E., Franssen, O., Tlasma, H., van Steenbergen, M. J., Kettenes-van den Bosh, J. J., Hennink, W. E.: *Macromolecules*, *28*, 6317 (1995).
6. Cavalieri, F., Miano, F., D'Antona, P., Paradossi, G.: *Biomacromolecules*, *5*, 2439 (2004).

L06 HYDROLYTIC STABILITY OF GF/UPE COMPOSITES

ONDŘEJ SMRTKA and VLADIMÍR ČECH
Institute of Materials Chemistry, Faculty of Chemistry, Brno University of Technology, Purkyňova 118, 61200 Brno, Czech Republic, smrtka@fch.vutbr.cz

Introduction

Thermosetting unsaturated polyesters with glass fibers as the reinforcement are used extensively as the materials in composite systems. Although these composites are often used in aggressive environments due to their chemical resistance, this resistance cannot be perfect. The effects of environment to these materials are just different or not as rapid as in the case of traditional materials like metals or wood. Moisture diffuses into all organic matrix composites, to varying extents and at various rates, leading to changes in their mechanical and thermophysical properties[1]. The polymeric matrices, in fact, do not represent an effective barrier to the diffusion of water through the fibers. Absorbed moisture, as both plasticizer and a crazing agent, deteriorates the mechanical integrity of the matrix, in a manner, which is dependent upon the temperature and humidity to which the material has been previously exposed[2]. Temperature of glass transition T_g is reduced due to the plasticizing effect of water.

Usually, the matrix has a greater sensitivity to moisture then the fiber; polyester bonds presented in resin can be hydrolyzed, especially at risen temperatures. Therefore matrix-dominated properties will be most affected. The interphase region is also strongly attacked; water gets between the fiber and the matrix and minimizes the adhesion between them. Sizing prevents the water diffusion in the material and increases the adhesion between the fiber and the matrix. Most usual ingredients of sizings are silane coupling agents. However, the siloxane bond between the agent and the fiber can be hydrolyzed, too[3]. This also causes changes in adhesion between fiber and matrix leading to decrease of mechanical properties.

Moisture induced effects are often reversible on drying the composite. In addition, absorbed moisture will modify the changes in internal stresses. It is essential that a resin-rich layer is presented on the composite surface to protect glass fibers from moisture degradation. This is usually accomplished by the use of gel coats and surface veils[4].

In this paper we managed to sum up the behavior of the composite glass fibers/unsaturated polyester resin (GF/UPE) during stay in water environment. The E-glass fibers with commercial silane sizing and bare fibers were used as the reinforcement, as the matrix we used isophtalic acid-based unsaturated polyester resin cured with styrene.

Experimental

Materials: Glass fibers (roving 1200 tex, average diameter of fibers 19 μm) were obtained from Saint Gobain Vertex a. s., Litomyšl, CR, one type without sizing and another with

commercial sizing 706 (mixture of silane coupling agents) applied by the manufacturer.

Isophtalic acid-based unsaturated polyester resin Viapal VUP 4649 was purchased from Polyvia Nova s.r.o. Zlín, CR. Separator Axel Inpul 24, Peroxide 62, Percadox 16, UV-Stabilizer MTE and styrene were purchased from Prefa a. s., Brno, CR. All compounds were used as obtained.

Samples preparation: Short beams of unidirectionally reinforced composite material were prepared by hand lay-up. The resin system was prepared by mixing 96.1 % Viapal VUP 4649, 0.5 % Axel INPUL 24, 1.0 % Peroxide 62, 0.2 % Percadox 16, 0.2 % Uvabsorb MTE and 2 % of styrene, in which the other additives were premixed before adding to Viapal (all values are weight %). The composite beams were prepared in silicon rubber (Lukopren) form, in which the beams were cured.

In the first step, the resin was partially cured; then the beams could be taken out of the form and post-cured. This is the complete temperature program of curing:

I. Ramp to 45 °C in 5 minutes
II. Isothermal at 45 °C for 30 minutes
III. Ramp to 100 °C in 30 minutes
IV. Isothermal at 100 °C for 30 minutes
V. Ramp to 140 °C in 30 minutes
VI. Isothermal at 140 °C for 60 minutes
VII. Automatic drop to laboratory temperature
VIII. Cure of separate beams for 24 hours at 140 °C (step 2).

After curing the samples were grinded to dimensions $(35 \times 10 \times 5)$ mm^2 for mechanical and physical properties testing, and to various dimensions for determination of diffusion constants.

Resulting fibers content in the composite was around 60 vol. %.

Determination of diffusion constants: Weight gain of water (M) in composite material was measured. The samples were exposed to water for the different time. After pulling the samples out of water they were wiped and let getting dry for 3 minutes on air before they were weighed on analytical balance. Samples from the boiling water were cooled in cold water before drying.

The diffusion rates were determined using Equation

$$\frac{Ml\sqrt{\pi}}{4M_\infty\sqrt{t}} = \frac{l(d+b)}{db}\sqrt{D_x} + \sqrt{D_y}\,, \qquad (1)$$

where M is the moisture content at time t, M_∞ is the equilibrium or maximum moisture concentration, d, b and l are coupons thickness, breadth and length, D_x and D_y are the diffusion constants through-thickness, and along-the-length of the material.

The Equation was derived[5] starting from Fickian diffusion law and other presumptions[6,7].

Let A Equals $\frac{Ml\sqrt{\pi}}{4M_\infty\sqrt{t}}$ and B Equals $\frac{l(d+b)}{db}$. When A is plotted against B, value of D_x and D_y can be obtained from the slope $\left(\sqrt{D_x}\right)$ and the intercept $\left(\sqrt{D_y}\right)$, respectively. This dependence (equation 1) is fully correct only at the beginning of exposure to water, when the diffusions in different directions do not influence each other.

Mechanical tests: Dynamic-mechanical measurements were performed on a TA Instruments Dynamic Mechanical Analyser DMA 2980. The short beam was tested as the single cantilever, with following parameters: span-length approx. 17 mm, frequency 10 Hz and amplitude 5 μm. Temperature was equilibrated at 35 °C and then ramped to 140 °C at 2 °C min^{-1}. From this measurement, the storage modulus, loss modulus, loss tangent and glass transition temperature (T_g) were obtained. T_g was determined from the maximum of tan δ dependence.

The short-beam test was performed according to the standard ASTM D 2344/D 2344M[8]. Universal Testing Machine Zwick Z010 was used to perform this test. Parameters for this measurement were following: three-point bending, loading nose diameter 6 mm, supports diameter 3 mm, span length 20 mm, testing speed 1 mm/min. Short-beam strength is determined using Equation 2:

$$F^{sbs} = 0.75\frac{P_m}{bd}\,, \qquad (2)$$

where F^{sbs} is short-beam strength [MPa], P_m maximum load observed during test [N], b is specimen width [mm] and d is specimen thickness [mm].

Mean values of T_g, short-beam-strength and storage modulus were obtained from at least three measurements, with standard deviation.

Results and discussion

In this section the results of weight gain measurements during exposure to water environment and related changes of mechanical and physical properties of composite material are summarized.

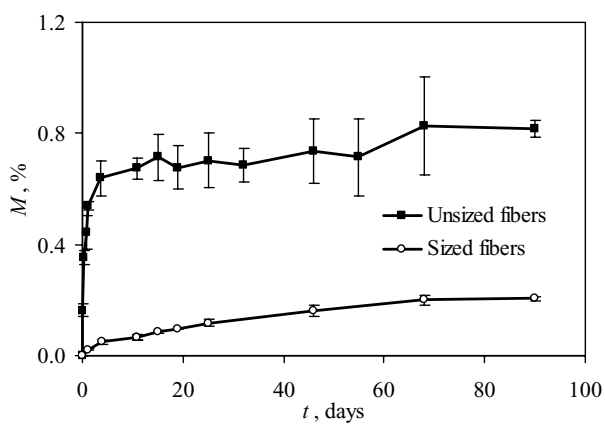

Fig. 1. **Moisture absorption in the GF/UPE composite, cold water (23 °C)**

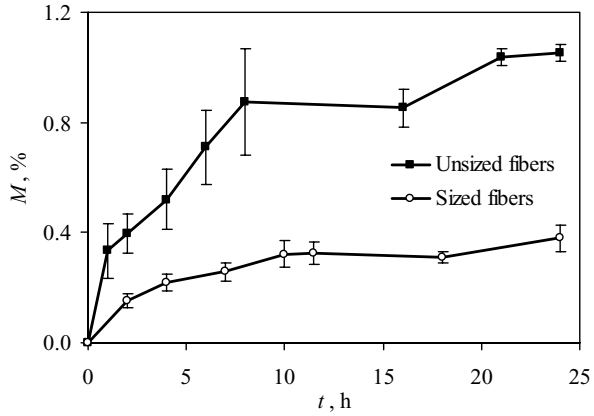

Fig. 2. **Moisture absorption (M) in the GF/UPE composite, hot water (98 °C)**

The following graphs show the dependences of moisture absorbed in composite material on time of exposure to water environment.

From these dependences the maximum moisture content in the material and the phase of validity of Fickian diffusion law were determined. These data were used in diffusion constants calculations.

Following table shows D_x, D_y and D_y/D_x, the diffusion constants and their ratios:

Table I
Diffusion constants

Material	Environment	M_∞ [%]	D_x [mm^2 s^{-1}]	D_y [mm^2 s^{-1}]	D_y/D_x
Unsized GF/UPE	23 °C water	0.83	$1.8\cdot10^{-5}$	$7.9\cdot10^{-5}$	4.4
Unsized GF/UPE	98 °C water	1.05	$7.9\cdot10^{-6}$	$2.1\cdot10^{-3}$	266
Sized GF/UPE	23 °C water	–	$1.3\cdot10^{-8}$	$1.5\cdot10^{-7}$	11.5
Sized GF/UPE	98 °C water	–	$3.9\cdot10^{-6}$	$4.4\cdot10^{-5}$	11.3

In the case of the composite GF(sized)/UPE the values of maximum weight gain M_∞ were not reached and the value from the weight gain measurement in GF(unsized)/UPE composite exposed to cold water was used for the calculations. The error is significant, but it does not meet the D_y/D_x ratios. These values are not much precise, the percentage error is expected to be about 20 %, through the errors in measurement of dimensions of the beams, the variance of weight gain values and the estimate of the maximum moisture concentration values for GF(sized)/UPE composite; the values of diffusion constants can suspiciously show ranges of the diffusions along the fibers and transversally and the differences between the diffusion in cold and hot water.

The following two graphs (Fig. 3. and 4.) show the values of short-beam-strength and storage modulus of the composite material before and after exposure to water. Great differences are evident between the composite containing

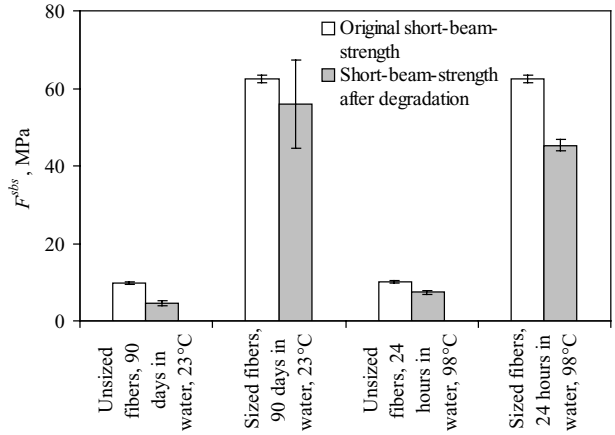

Fig. 3. **Short-beam-strength (F^{sbs}) of the composite before and after exposure to water environment**

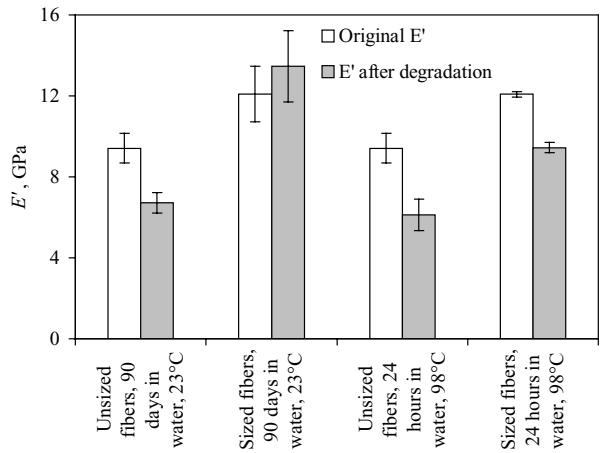

Fig. 4. **Storage modulus (*E'*) of the composite before and after exposure to water environment**

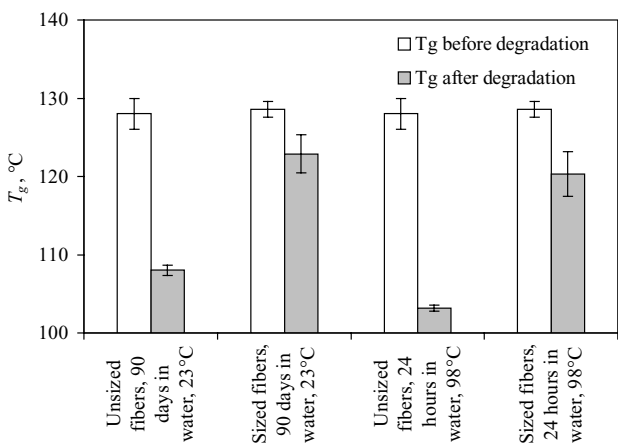

Fig. 5. **Glass transition temperature (T_g) of the matriw before and after exposure to water envionment**

unsized and sized fibers. Mainly the strengths of the composites are very different. The value of the storage modulus is highly affected by elastic modulus of the fibers.

Data in the Fig. 5. show decrease of the glass transition temperature of polyester resin used as the polymer matrix. The decrease is very significant in GF(unsized)/UPE because of higher diffusion rate of water. The graph of T_g implies that water serves as the softener and that the Fox equation can be used to describe this phenomenon even in our composite system.

In all of these measurements it was proved, that the degradation processes occur in the hydrolytic active environments. Short-beam-strength, storage modulus and also glass transition temperature descend during the composite material stays in water.

From the obtained results it can be concluded that the sizing of the fibers increases the mechanical properties, such as the short-beam-strength and storage modulus, indirectly demonstrating the increase of adhesion between the fibers and the matrix. The sizing also decreases the influence of the hydrolytic environment on the properties of the composite material by slowing down the diffusion of water.

Conclusion

In this work the influence of the hydrolytic active environment on the composite material glass fibers/unsaturated polyester resin (GF/UPE) is dealt. Changes of mechanical properties (short-beam-strength, dynamic storage modulus) of the material and glass transition temperature of polymer matrix are studied.

The project was intended as the preliminary study of hydrolytic stability of GF/UPE with aim to determine the extent of degradation of existing systems. Fibers with new sizings will be used for composite preparation later, and these composites will have to be tested with respect to hydrolytic stability and compared with the existing systems. Also other environments will be used, e. g. acidic and basic solutions. Long-term testing is planned, too.

The authors express their thanks to M. Sirový and Saint-Gobain Vertex for providing glass fibers. This research was supported by grant no. 104/03/0236 (Czech Science Foundation).

REFERENCES

1. Jones F. R., in: *Reinforced plastics durability* (Pritchard G., ed.), p. 70. Woodhead Publishing Limited, Cambridge 1999.
2. Apicella A.: Composites *13*, 406 (1982).
3. Plueddemann E. P.: *Silane Coupling Agents*. Plenum Press, New York 1991.
4. Sims G. D., Broughton W. R.: Comprehensive Composite Materials *2*, 151 (2000).
5. Smrtka O.: *Diploma thesis*. Brno University of Technology, Brno, Czech Republic, 2004.
6. Jones F. R.: *Proceedings of Conference on Designing Cost Effective Composites, London*, *15–16 September 1998*, p. 65. Professional Engineering Publishing, London 1998.
7. Shen C. H., Springer C. S.: Journal of Composite Materials *10*, 2 (1976).
8. ASTM D2344/D2344M-00: Standard Test Method for Short-Beam Strength of Polymer Matrix Composite Materials and Their Laminates (2000).

L07 EFFECT OF PAPER PROPERTIES ON INK-JET PRINT QUALITY

ŠTEFAN ŠUTÝ[a], JURAJ GIGAC[b], MILAN VRŠKA[a], PAVOL STREŽO[a], MICHAL JABLONSKÝ[a], RADOVAN TIŇO[a], KATARÍNA VIZÁROVÁ[a] and JANA KOZÁNKOVÁ[a]

[a]Department of Wood, Pulp and Paper and Department of Ceramics, Glass and Cement, Faculty of Chemical and Food Technology Slovak University of Technology, Radlinského 9, Bratislava, Slovak Republic, stefan.suty@stuba.sk, [b]Pulp and Paper Research Institute Bratislava, Lamačská cesta 3, Bratislava, Slovak Republic, gigac@vupc.sk

Introduction

The quality of print in any print technology depends on the parameters of printing process and the parameters of paper. The optimum parameters of paper can be adjusted by paper producers that are motivated to produce optimum quality paper for different kinds of print. From the point of print, paper is characterised by runability and printability. Runability is determined by all properties that influence total output of printing devices. Printability quantifies print quality or qualitative potential of paper running through a given printing process. To test printability usually means to test paper, trial print on paper and to perform measurements on and to evaluate trial-print papers and commercial papers. Printability can be represented by a set of properties typical for a particular sort of paper, but it can also be expressed by so called suitability of that particular sort of paper for a certain printing process[1]. A print quality is usually characterised by optical quality and user quality[2]. Analysers of high quality differentiation are being developed to evaluate the technical quality of an image. They are expressed in quantities of statistic information technology[3,4]. However, presently besides classic methods applied in print quality research, there exist many other applications suitable for digital analysis of images. To qualitatively evaluate useful properties of paper, sensory evaluation and assessment have been accepted as a fully reliable procedure, e. g. in evaluation of printed papers. There are several methods for evaluation of sensorially perceived quality. One of them is the method of all-pairs ranking. To evaluate by this method, a set of samples has to be prepared and each sample is compared to every other sample[5].

Thus, a paper can be evaluated sensorially and assessed as a sum of all parameters of print and paper that affects all human senses. On the other hand, a paper can also be evaluated objectively, on the basis of paper and print. From the relations between sensorially evaluated parameters and objective parameters we can decide about decisive technological parameters, as to their effect on optical perception by human beings. The aim of this paper is to analyse relations between objective methods of print quality assessment, paper properties and sensory evaluation and assessment.

Material and methods

Several types of commercially available paper were used: a) non-coated, b) coated matt or c) coated glossy. All coated paper samples were intended for application in quality photography print. The various sorts of papers were investigated for their characteristic parameters that are listed in Table I. The properties were measured and evaluated by standardised procedures and techniques in accordance with the STN ISO standards.

S t r u c t u r e o f p a p e r

The surface and section area of all samples has been investigated with the help of SEM and optical microscope and the photographic images were assessed. Our results show that for ink-jet papers different sorts of paper have been used as a basis for coating, as well as fillers. The findings are in Table II.

Table I
Characteristic parameters of various sorts of inject paper

Sample	Basic weight of paper [g m^{-2}]	Thickness, [μm]	Paper mass per volume [kg m^{-3}]	Roughness, PPS [10 kp cm^{-2}]	Ash content 450 °C [%]
2	82.1	96	855	4.1	17.7
3	110.8	140	791	3.1	27.6
6	170.4	215	793	0.91	14
6B	180.1	211	854	3.3	23.9
10	102.1	124	823	4.8	24.9
15	137.6	164	839	2.3	17.3

Table II
Characteristic features of ink-jet paper surface

Sample Nr.	Averse side	Thickness of coating [μm]	Reverse side	Paper
2	non-coated	0	non-coated	paper filled with fine particles
3	matt/coated	15	matt/coated	non-filled
6	glossy/coated	25	matt/coated	filled, large particles
6B	matt/coated	33	matt/coated	–
10	matt/coated	35	non-coated	high filled, fine particles
15	glossy/coated	55	non-coated	non-filled

Note: The thickness of coating in sample 6B was found with the help of optical microscopy all others used SEM.

Table III
Parameters of porous structure of paper

Sample	Overall specific volume [mm^3 g^{-1}]	Specific surface [m^2 g^{-1}]	Average radius of pores [$\times 10^{-1}$ nm]	Overall porosity [%]
2	518	4.15	20240	28
3	615	28.16	13020	50
6	650	17.98	23360	30
6B	570	24.68	13020	34
10	553	24.12	16230	27
15	513	21.82	20240	49

Table IV
Optical characteristics of paper measured with different filter

Sample		D_0 2	3	6	6B	10	15
Filter applied	c	0.0706	0.0700	0.0694	0.0476	0.0876	0.0546
	m	0.0746	0.0758	0.0820	0.0558	0.0972	0.0630
	y	0.0490	0.0558	0.0642	0.0302	0.0580	0.0578
	v	0.0762	0.0778	0.0816	0.0562	0.0978	0.0634

P o r o s i t y

To find out the porous structure of papers, the samples were measured by mercury microporosimetry. This method allows us to obtain the following paper parameters: overall specific volume of pores, specific surface of pores, average radius of pores and overall porosity as well as distribution of pores) that characterise the porous structure of paper. The results are introduced in Table III.

A n a l y s i n g o p t i c a l d e n s i t y o f p r i n t o n p r i n t e d i n k - j e t p a p e r s

The measurements were carried out on samples of ink-jet papers. Every sample was printed in four lines. In each line there were three squares. Every line was printed in the same colour (cyan, magenta, yellow, black) but each had a different area print density. One square in line had the area print density A = 100 %. Tables IV–VIII give colorimetric data of colours measured at separate samples of papers. The optical characteristics were measured with the device X – Tire 486. The measurements were carried out on samples backed with a black matt pad. The measurements of absolute optical density of pads were performed with all four filters (c-bright blue, m-purple, y-yellow, v-visual). The measurements of process print colours were done under the given filters (bright blue – c filter, purple – m filter, yellow – y filter, black – v filter). Every printed colour and every pad underwent five measuring procedures. Their average values and standard deviation can be found in Tables IV–VIII. The measured data were used to calculate the values of densitometrically effective degree of area print density. The area print density, rastre tone value, of autotypical area is defined in Murray-Davies Equation 1:

Table V
Optical densities for cyan printed squers

Sample	Cyan1 (C1)		Cyan2 (C2)		Cyan3 (C3)	
	D_{100}	A [%]	D_r	A [%]	D_r	A [%]
2	1.0076	100	0.7556	89.72	0.2310	34.92
3	1.1216	100	0.7130	84.77	0.1962	27.67
6	1.1852	100	0.7480	85.59	0.2174	31.27
6B	1.1240	100	0.7102	85.42	0.1802	28.72
10	1.0906	100	0.7330	85.91	0.2248	30.07
15	1.1820	100	0.7464	86.09	0.2063	31.86

Table VI
Optical densities for magenta printed squers

Sample	**Magenta1 (M1)**		**Magenta2 (M2)**		**Magenta3 (M3)**	
	D_{100}	**A (%)**	**D_r**	**A (%)**	**D_r**	**A (%)**
2	1.1176	100	0.5178	70.33	0.1530	18.16
3	1.3662	100	0.4380	59.62	0.1350	13.43
6	1.4754	100	0.4962	64.06	0.1544	16.00
6B	1.3700	100	0.4512	62.81	0.1236	15.19
10	1.2882	100	0.4738	61.98	0.1622	14.86
15	1,4614	100	0,4850	64,74	0,1398	16,88

Table VII
Optical densities for yellow printed squers

Sample	Yellow1 (Y1)		Yellow2 (Y2)		Yellow3 (Y3)	
	D_{100}	A [%]	D_r	A [%]	D_r	A [%]
2	1.1218	100	0.5226	72.53	0.1768	27.85
3	1.3656	100	0.4528	63.00	0.1490	20.31
6	1.4392	100	0.5224	68.05	0.1800	24.44
6B	1.3600	100	0.4496	64.97	0.1310	21.73
10	1.3116	100	0.4934	67.04	0.1644	23.01
15	1.4422	100	0.4966	66.33	0.1668	23.15

Table VIII
Optical densities for black printed squers

Sample	Black1 (B1)		Black2 (B2)		Black3 (B3)	
	D_{100}	A [%]	D_r	A [%]	D_r	A [%]
2	1.1914	100	0.5950	75.51	0.1610	19.21
3	1.4444	100	0.4946	64.47	0.1392	13.78
6	1.6310	100	0.5482	67.76	0.1576	16.52
6B	1.4506	100	0.4956	66.32	0.1222	14.69
10	1.3914	100	0.5270	66.14	0.1650	15.10
15	1.6660	100	0.5334	67.81	0.1386	16.31

$$A = \frac{1-10^{-(D_r-D_0)}}{1-10^{-(D_{100}-D_0)}}$$

A – print density (%)
D_r – optical density of autotypical area
D_{o-} optical density of paper
D_{100} – maximal optical density.

Comparisons of the area print density values show that the area print density of sample 2 is the highest with all print colours and the second sample having the highest area print density is the sample 10. The basis weight of sample 2 is 104 g m^{-2}, and it is a non-coated, wood free white paper. Sample 10 has the basis weight 108 g m^{-2} and it is a coated, from one side matt, wood free paper.

Comparisons of differences in optical density of print colours from particular sample lead to the conclusion that the differences reach the highest values with all colours, except for colours with effective area print density 100 %. The best parameters for differences of optical density in all set of colours could be found with samples 15 (glossy, coated, wood free paper) and 6 (glossy, coated, wood free paper).

Test of print quality on printed samples of paper by pair comparison

To compare the paper quality as to quality of print, we chose a subjective method of successive pair comparison of printed samples of papers. Twelve persons randomly chosen compared and evaluated the print quality of single samples. The samples carried the same testing picture that was printed by the same regime of print. The evaluated parameters were sharpness of print edges in details, precision, readability of letters, agreement with the original, adhesion of print and smear of colour. Each of the evaluators filled in a test sheet questionnaire. The evaluation and assessment of the test sheets and quality classification were done by Gigac and Krkoška[2]. To compare single samples the PV Index had to be calculated. The results can be found in Table IX.

Table IX
Calculated values of PV Index and final order of samples

Sample	2	3	6	6B	10	15
PV Index	0	25	40	29	14	41

Microscopic determination of depth of jet-ink absorption

The depth of absorption of single print points was studied by optical microscope and the results of this procedure have been summarised in Table X (ref.[6]).

Penetration of ink-jet colours

Data on thickness of coating and absorption of jet-ink are shown in Table X. The depth of penetration was measured in imprints with the lowest area print density, where the points were printed as individual and did not overlap. As can

Table X
Microscopic determination of depth of jet-ink Statistic characteristics of samples

Sample no	2	3	6	6B	10	15
Averagea [μm]	20	24	29	26	25	20
Minimum [μm]	17	17	18	19	22	15
Maximum [μm]	27	27	42	33	28	28
Standard deviation	3.46	3.77	5.21	4.08	2.42	4.47
Thickness of coating [μm]	0	15	25	33	35	55
Depth of ink penetration [μm]	20	24	29	26	25	20
Diference [μm]	20	9	4	–7	–10	–35

be seen, sample 2 is non-coated, samples 3 and 6 show deeper absorption than just into the coating layer, in samples 6B, 10 and 15 the ink is held in the coating. It can be concluded that the paper pad of coated papers does not play an important role in ink absorption. In some cases (sample 6B, 10, 15) the ink did not penetrate to the pad at all. Thus, mostly the coating of paper with its chemical and physical properties influences the quality of print.

Results and discussion

The aim of this paper has been to find out those significant parameters of paper that influence the quality of print evaluated by a subjective method (sensory evaluation and assessment by comparison of pairs) and by an objective method (optical density of print).

The dependence of PV Index on optical density of print D100, with a strong polynomial correlation between the quantities is documented in Fig. 1. As can be seen, the optical density of print as a measure of objective method of print quality correlates very well with the PV Index which is a measure of subjective evaluation of print quality. Both parameters are suitable for evaluation and assessment of print quality. The effect of other parameters of paper on the two most decisive parameters of paper, considered as to print quality, has been the subject of study presented in this paper.

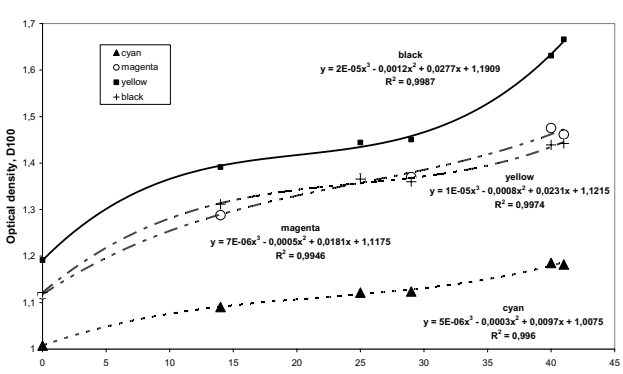

Fig. 1. **Dependence of PV Index on optical density D 100 of imprints produced by ink-jet printing**

The inner structure of paper was examined by mercury porosimetry. Using this method one can feel uncertainty as to values obtained. Nevertheless, this method is advantageous for analysis of certain structural parameters of coated papers some of which are introduced in Table II. The enumerated parameters signal certain dependence between the PV Index and specific surface of paper (Fig. 2.). A similar dependence has been found between optical density and specific surface of paper (Fig. 3.).

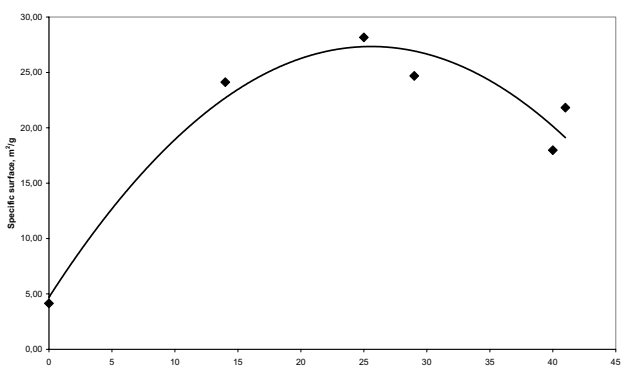

Fig. 2. **Dependence of PV Index of samples on specific surface of paper, as determined by mercury microporosimetry**

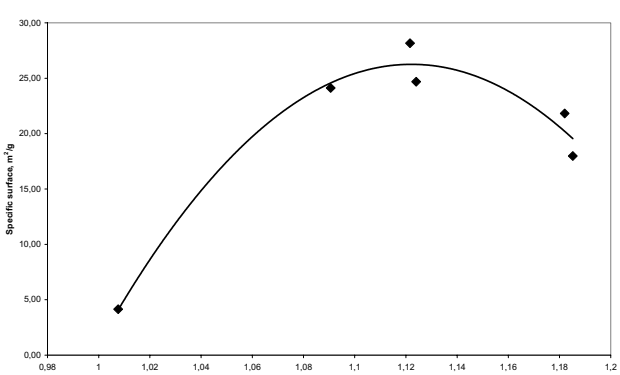

Fig. 3. **Dependence of optical density of samples on specific surface of paper, determined by mercury microporosimetry**

These dependencies can only be explained with difficulty. It can be said that the worries mentioned above have come true. In our case, various samples have been compared by mercury microporosimetry as to their structure (Table II.) The measurements of porosimetry provide us with a complex value that is a summary of structural properties of a paper and its coating. However, it should be stressed that as for the print quality, the most decisive and important is the layer of coating and not the layer of paper, to which the ink nearly did not penetrate, as can be seen from our measurement in Table X. Unambiguously it can be presumed that specific coating surface will have a decisive effect on quality of ink-jet print.

Conclusion

The presented investigation has revealed a significant correlation between objective and subjective assessment of quality of ink-jet print. The optical density D 100 correlates with PV Index as determined by subjective and objective comparisons of prints. These two parameters can be considered objective for determination of print quality.

Another dependence between the specific surface of paper, as measured by mercury microporosimetry, and between PV Index, as well as between optical density has been also found. The dependence curve is concave and the maximum values of optical density and PV Index do not occur at maximum values of specific surface.

This analysis leads to conclusion that the print quality will be significantly influenced by specific surface of paper. Other properties that were followed in our investigation did not prove any correlation with the parameters determining print quality.

This paper was supported by the Agency for Promotion of Science and Technology from the project APVT-99-007302.

REFERENCES

1. Kocurek J., Kouris M., in: *Pulp and Paper Manufacture vol. 9 Mill Control & Control Systems (Aspler J. S.)*, chapter VII, p. 192. 3rd ed. 1992.
2. Gigac J., Krkoška P.: Papír a celulóza *57*, 368 (2002).
3. Černý J.: *Nekterá nové pohledy na vymezení kvality tisku a její měření*, odborný seminár VŠCHT Pardubice, 1993, p. 36.
4. Perento J., Erho T.: Paper Technology *40*, 29 (1999).
5. Chareza C., Greve T., Gottsching L.: Das papier *39*, 239 (1985).
6. Lehotský V.: *MSc. Thesis*. Slovenská technická univerzita v Bratislave, Bratislava, 2004.

L08 THE STUDY OF CONE CALORIMETER METHOD OF ACCELERATED PAPER AGEING AND SPECTRAL DETERMINATION OF PAPER PERFORMANCE CHARACTERISTICS

IGOR ŠURINA[a], MARTIN POLOVKA[a], MILAN VRŠKA[a], MONIKA FRISOVÁ[a], SVETOZÁR KATUŠČÁK[a], MILAN MIKULA[b] and HELENA MARTVOŇOVÁ[c]

[a]Department of Chemical Technology of Wood, Pulp and Paper, igor.surina@stuba.sk, [b]Department of Graphic Art Technology and Applied Photochemistry, Faculty of Chemical and Food Technology of the Slovak University of Technology, Radlinského 9, 812 37 Bratislava, Slovakia, [c]Pulp and Paper Research Institute, Lamačská 3, 841 04 Bratislava, Slovakia

Introduction

The process of paper ageing, which results in worsening of its physico-mechanical properties and therefore leads to potential loss of information on historical and cultural heritage, is intensively studied all over the world by means of wide range of mostly destructive methods (folding endurance, tear strength, as well as zero-span breaking length)[1,2].

These methods are time-consuming and their reliability is not as high as it should be. Therefore, non-destructive analytical methods based on the interaction of studied material with energy, photons, waves (e. g. spectrophotometry, UV-VIS, FTIR and Raman spectroscopy, as well as colorimetry, ultrasonic method, and image analysis) are used [3–8,17].

Wood and cellulose itself have been widely studied by Fourier transform infrared spectroscopy[6–12], but only few works concern the ageing of paper. The correlation between the spectral and mechanical parameters was not published up today.

In this study, different heat flows were applied to the commercially available paper samples using cone calorimeter heater. The structural changes, which take place during the accelerated ageing[18–19], were evaluated by means of FTIR DRIFT spectroscopic method. Subsequently, the results obtained were correlated with the changes in their mechanical properties (folding endurance and tensile strength) in an order to verify FTIR spectroscopy as a method suitable for monitoring the ageing process as well as the cone calorimetry as alternate ageing method.

Experimental

Paper sample characterisation. Commercially available newsprint paper – paper mill Slavošovce, Slovak Republic, (surface pH ~ 4.5; grammage ~ 66.9 g m^{-2}) was used. Paper sheets were stored at 300 K and relative humidity of 50 % between the experiments.

Accelerated ageing. Thermally accelerated ageing of paper samples was carried out using cone calorimeter (Fire Testing Technology, Ltd., UK). The sample was placed into the specimen holder of calorimeter in the horizontal orienta-

tion, and treated with constant heat flow energy in the range of 0–10 kW m^{-2}.

DRIFT analysis. The paper samples (approximately area of 1 cm^2) were placed in a standard sample holder of Digilab Excalibur FTS 3000MX FTIR spectrometer. The FTIR spectra were recorded with the resolution of 4 cm^{-1} using DRIFT technique from both topside and underside in an order to account the side-orientation effect. Spectra were recorded over the range 400–4000 cm^{-1} as the average of 40 individual scans.

Test of mechanical properties. The mechanical properties tests of all paper samples were performed according to STN ISO 1924-1 (1996) (Ref[13]) and STN ISO 5626 (1999) (Ref[14]) standards.

Statistical analysis. The experimental DRIFT spectra were mathematically evaluated using OMNIC® (Thermo Nicolet Corp.) and MicroCal® Origin software. The kinetic parameters and statistical calculations were realized using MicroMath Scientist software.

Results and discussion

Drift FTIR spectra

The degradation of paper samples as a result of the thermal ageing process causes the changes in both physical and chemical composition. The decrease of degree of polymerization (DP) followed by changes in the hydrogen bonds network structure influencing the ratio of amorphous/crystalline areas, the formation of low-molecular weight carbonyls and ketones, as well as of carboxylic acids and esters should be expected in accord with generally accepted process of both cellulose back-bone degradation and oxidation.

Firstly, FTIR spectra of each paper sample were recorded from both sides, as depicted in Fig. 1. Here in these experiments, the main differences between spectra appear in the region of ν (OH) vibrations (~ 3400) and additionally, in the region of ν (C-O) and δ (CH_2) ~ 1100–1000 cm^{-1}. Some differences in the region of about 800 cm^{-1} are also visible, probably as a result of different content of inorganic filling agents accompanied by the changes in the aromatic ring structures[8,10]. The above mentioned side-effect was previously described elsewhere[15,16], mostly caused by the orientation of the pulp fibers and other components on the machine wire during paper fabrication. The under (machine) side of paper is rougher; the content of glues as well as the brightness and whiteness is lower than that of topside[15,16].

Baseline correction was realized in two steps. Firstly, all the spectra intensity was set to zero at 1900 cm^{-1},where no significant absorption appears for this type of matrix. Subsequently, the baseline was created carefully using OMNIC® software and subtracted from the spectrum, as previously describet by Oh et all[10]. All the measured spectra (asigned to the same side only), were transformed using Kubelka-Munk function (KM). The KM intensities of characteristic spectral bands were evaluated and mutually compared.

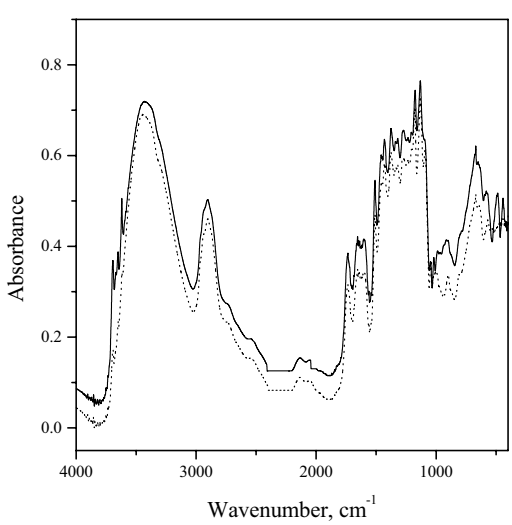

Fig. 1. **Experimental DRIFT FTIR spectra of newsprint paper (paper mill Slavošovce, pH ~ 4.5; grammage ~ 66.9 g m^{-2}), measured with resolution of 4 cm^{-1} for both topside (—) and underside (….). The spectra are the average of 40 individual scans**

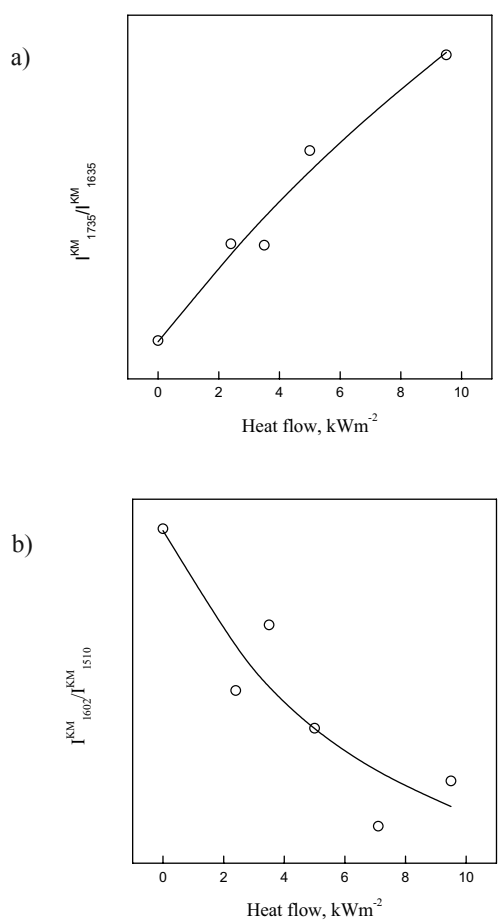

Fig. 2. **The experimental (○) and calculated (—) dependencies of averaged KM intensities on heat flow energy, evaluated from experimental DRIFT spectra:** a) **C=O valence vibrations of aldehydes, ketones and carboxylic acid/carboxylate anions;** b) **C=C stretching vibrations of lignins**

The most interesting are the changes in the region of about 1740 cm^{-1} and 1635, where the presence C=O valence vibrations of aldehydes, ketones and carboxylic acid/carboxylate anion set in, respectively. Fig. 2a. illustrates the dependence of the $I^{KM}_{1735}/I^{KM}_{1635}$ ratio on the energy heat flow. Both bands intensity decrease as a result of ageing process. This decrease was fitted using exponential function model ($I^{KM}=a\cdot\exp(-k\cdot x)$, where „a" represents pre-exponential factor, „x" is the energy of heat flow). The values of so evaluated exponential factor (k^{KM}_{1735} ~ 0.048, k^{KM}_{1635} ~ 0.028, R^2 ~ 0.996 and 0.998) indicates, that the carboxylic acids/aldehydes probably transform to more stable ketones during the ageing process, subsequently released from the paper surface.

The changes in chemical structure is very good observable through the changes in lignins structures. The bands at ~ 1602 and 1510 cm^{-1} were previously assigned to phenyl C=C stretching vibrations of the aromatic rings of 3,5-dimethoxy-4-hydroxyphenyl (syringyl) and 3-methoxy-4-hydroxyphenyl (guaiacyl), respectively – both of the lignins origin. The syringyl to guaiacyl ratio (Fig. 2b) calculated from the relative intensities of both bands can be used as the marker of lignins degradation[6–8].

Very helpfull information, in good accordance with previously published data for different types of accelerated ageing, and also with the results obtained in standard mechanical properties tests, brings the ratio 1430/900 cm^{-1} as well as the changes of band at 1385 cm^{-1} (Fig. 3.). The first mentioned is known as crystallinity index (CI)[9,10], and gives the information about the changes in the structure of cellulose during the ageing, as the amorphous cellulosic polymer changes to crystalline form, accompanied with the decrease of DP. The last one serves as the marker of the conformational changes in glycosidic bridge, occuring as a result of paper sample tretment.

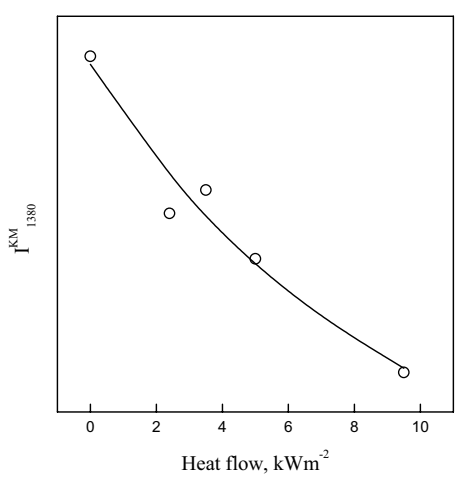

Fig. 3. **The experimental (○) and calculated (—) dependence of averaged KM intensity on heat flow energy, evaluated from experimental DRIFT spectra, representing the conformational changes in glycosidic bridge during thermal ageing**

M e c h a n i c a l p r o p e r t i e s t e s t

The tests of mechanical properties are the most commonly used experimental methods in paper properties evaluation. With numerous of modifications they are used from the middle of last century, but their application still brings some problems, concerning mainly the reliability of the results obtained. To compare the properties of different paper samples, folding endurance index, taking into account the grammage of paper sample is likely accepted. Fig. 4. shows the dependence of the average folding endurance index on the heat flow energy. In accordance with the expectation, the mechanical properties became worsen as a result of the changes induced by the ageing process.

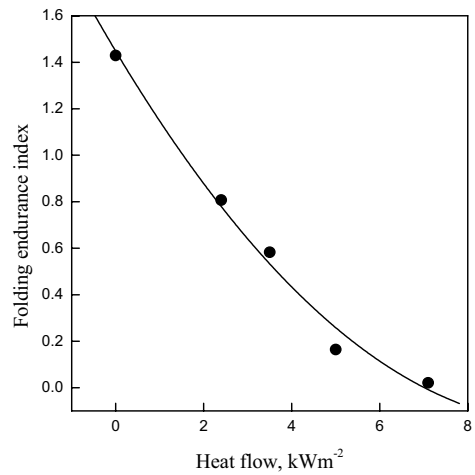

Fig. 4. **The dependence of experimental (●) and calculated (—) average folding endurance index on heat flow energy**

Conclusion

The cone calorimetric ageing of paper samples is the appropriate equivalent to standardly used ageing methods. The DRIFT spectroscopy is suitable and reliable method for the evaluation of changes, occuring in paper sample structure during the ageing process. The results are in good accordance with the test of mechanical properties. Additional experiments are in progress, in an order to optimize the process of assignment and mathematical evaluation of spectra.

We thank Slovak Grant Agency (Project VEGA 2/3161/23) for its financial support. Dr. Vlasta Brezová and Dr. Júlia Pigošová are gratefully acknowledged for helpful discussion.

REFERENCES

1. Rezayati-Charani P., Mohammadi-Rovshandeh J.: Bioresour. Technol. *In press* (2005).
2. Luner P.: Wood Sci. *22*, 81 (1988).
3. Chai X.-S, Hou Q. X., Luo Q., Zhu J. Y.: Anal. Chim. Acta *507*, 281 (2004).
4. Origgi S., Trichet V., Castellan A., Davidson R. S.: J. Photochem. Photobiol. A: *103*, 159 (1997).

5. Princi E., Vicini S., Pedemonte E., Mulas A., Franceschi E., Luciano G., Trefiletti V.: Thermochim. Acta *425*, 173 (2005).
6. Proniewicz L. M., Paluszkiewicz C., Weseucha-Birczynska A., Baranski A., Dutka D.: J. Mol. Struct. *614*, 345 (2002).
7. Proniewicz L. M., Paluszkiewicz C., Weseucha-Birczynska A., Baranski A., Konieczna A.: J. Mol. Struct. *596*, 163 (2001).
8. Colom X., Carrillo F., Nogues F., Garriga P.: Polym. Degrad. Stab. *80*, 543 (2003).
9. Ali M., Emsley A. M., Herman H., Heywood R. J.: Polymer *42*, 2893 (2001).
10. Oh S. Y., Yoo D. I., Shin Y., Seo G.: Carbohydr. Res. *340*, 417 (2005).
11. Cotrim A. R., Ferraz A., Goncalves A. R., Silva F. T., Bruns R. E.: Biores. Technol. *68*, 29 (1999).
12. Lojewska L., Miskowiec P., Lojewski T., Proniewicz L. M.: Polym. Degrad. Stab. *88*, (2005) 512.
13. STN ISO 1924-1(1996): Determination of Tensile properties (constant rate of loading method).
14. STN ISO 5626 (1999): Determination of Folding Endurance-Schopper method.
15. Panák J., Čeppan M., Dvonka V., Karpinský Ľ., Kordoš P., Mikula M., Jakucewicz S.: Basics of Graphic Arts Technology. TypoSet, Bratislava 2002.
16. Hinterstoisser B., Akerholm M., Salmen L.: Carbohydr. Res. *334*, 27 (2001).
17. Vizárová K., Soldán M.: UV/VIS spectroscopy study of paper colouring during accelerated ageing (in Slovak) In: Zborník príspevkov 51. Zjazd chemických spoločností, sekcia E, Drevo, celulóza, papier, Nitra 1999, STU Bratislava, s. E-P5 (1999).
18. Krkoška P., Vizárová K.: Chemické listy *94*, 881 (2000).
19. Vizárová K., Cedzová M., Reháková M., Šutý Š.: Papir a celulóza *58*, 264 (2003).

L09 ACTIVATION OF INTERACTIONS OF POLYSACCHARIDE MODIFICATORS WITH LIGNOCELLULOSICS

ĽUDMILA ČERNÁKOVÁ[a], KATARÍNA VIZÁROVÁ[b], ŠTEFAN ŠUTÝ[b], RADOVAN TIŇO, MARTINA CEDZOVÁ[b], MILAN VRŠKA[b] and SVETOZÁR KATUŠČÁK[b]

[a]Department of Plastic and Rubber, [b]Department of Chemical Technology of Wood, Pulp and Paper, Faculty of Chemical and Food Technology, Slovak University of Technology in Bratislava, Radlinského 9, SK - 812 37, Bratislava, Slovakia, katarina.vizarova@stuba.sk

Introduction

During the last decade several papers devoted to physical modifications of surfaces by plasma formed by electric discharge in various gases have appeared in the literature.

Plasma[1] may be characterized by several intrinsic parameters such as density of its individual components, energy and intensity of electromagnetic radiation, gas temperature, etc. In polymer chemistry the low-temperature plasma is usually applied possessing a low degree of ionization as its typical characteristic.

When working with gases such as N_2, O_2, CO_2 and similar, chemically active plasma is formed enabling to transport various function groups to the polymer surface able to exert positive impact on some physical properties. Coating the polymer material, natural or synthetic, with thin polymeric layers exhibiting specific features seems to be a very promising mode of treatment. This way of physico-chemical modification is based on radical formation on the treated surface with subsequent covalent bonding of new materials with specific properties[2–3].

The use of the plasma in modification of ligno-cellulosic materials is mentioned prediminantly in connection with hydrophobisation of paper surface[4–5]. A few papers deal with direct application of the plasma in the field of paper stabilisation. Vohrer[6] considered that the main advantage in the plasma use for documents conservation and protection lies in the fact that it is a dry procedure allowing to combine various effects, e. g. sterilization associated with an increase in paper strength, or deposition of polymeric films to protect documents against external adverse influence. Plasma may be used also to regulate the acidity of cellulose surfaces[7].

In the present work system of raw lignocellulosic materials (LCM) and polysaccharide modificators in conjunction with the activation by plasma in nitrogen atmosphere at atmospheric pressure was tested. Some modifications mixtures, based on some polysaccharides, were selected with the purpose of improving the strength and permanence of investigated materials.

Experimental

In a function of a raw LCM, paper with a basis weight of 45 g m^{-2}, groundwood, unsized (55 % groundwood, 20 % kraftpulp, 15 % recycled fibers, 10 % white clay), pH value of 4.5–5.0.

Polysaccharides used in modification mixtures preparation: low-molecular weight poly(D-glucosamine) chitosane (Aldrich), water soluble cellulose derivative methyl-hydroxyethyl-cellulose Tylose MH 300, cationic potato starch derivative Empresol N (Emsland-Stärke GMBH). Neutralizing solution 0.04 mol dm^{-3} $Mg(HCO_3)_2$ was prepared as the water solution of $MgCO_3$ saturated with CO_2 for 2 hours.

To modify paper samples, the following modification systems were used:

2% solution of chitosane in 0.1 M solution of CH_3COOH, (CH)

polysaccharide mixture consisiting of 1 % chitosane, 0.25 % Tylose MH 300 and 0.75 % Empresol N in water, (TECH)

polysaccharide mixture consisting of 1 % chitosane, 0.25 % Tylose MH 300 and 0.75 % Empresol N in neutralizing solution of $Mg(HCO_3)_2$ (TECHN).

A plasma equipment: coplanar barrier discharge at ambient pressure, nitrogen atmosphere, 1 second activation.

The paper samples were subjected to treatment using the above mentioned modificators and the dried surface was activated by the plasma in nitrogen atmosphere during 1 second. The samples modified in such a procedure were subjected to dry accelerated aging at 105 °C for 12 days.

Mechanical properties of the modified materials, tensile strength[8] and folding endurance[9] were determined. Monitoring pH of the samples surface[10] the changes in acidity were followed. Changes of surface structure were observed with Scannig Electron Microscopy (SEM).

Results and discussion

Raw LCM – paper samples in our investigation – are materials undergoing degradation during their lifetime[11–13]. There is a continuous search for new methods of lifetime prolongation and/or preservation of their utility properties. One of the modes lies in treatment of paper by combined physicochemical way applying plasma. In the present work, various kinds of polysaccharides were investigated as modification agents. Chitosane contains a high portion of nitrogen basicly in the form of primary amino groups, providing it with basic nature. Its solutions contain highly charged polycations allowing it to form insoluble ionic complexes with other ions present in aqueous solution. Stemming from the mentioned chitosane properties, paper treatment was based on an assumption on chitosane ionic bonding to a cellulose substrate, as well as on its ability to reduce the paper acidity. Cationic starch derivative is bonded to the negatively charged fibre surface in aqueous media providing thus a higher strength of the fibre. Within plasma activation it is supposed that covalent bonds are formed too. Two kinds of the active centres, namely radicals and nitrogen containing function groups (e. g. amino or imino groups) might be formed at plasma activation in nitrogen atmosphere. Chitosane may be covalently bonded and even crossed-linked via radicals providing that suitable conditions are reached.

Due to the primary importance of the paper strength, combination of chitosane and the impact of plasma on this property was investigated at first within preliminary experiments. It was found that plasma activation exhibited a positive effect to the measured parameter.

An effect of surface activation of the material by the plasma was verified both before applying the modification agent and after it. The procedure comprising a subsequent plasma application seems to be more efficient, namely for tensile strength parameter and based on this observation this procedure was used in further experiments.

The change in the mechanical properties due to modification was expressed as a ratio of the monitored values for the modified sample to that for the unmodified one after a certain duration of aging. The tensile strength of the modified material as a function of the modification procedure is illustrated in Fig. 1. The paper activated without previous impregnation exhibited a lower tensile strength. Chitosane-based protection layer in combined with plasma activation in nitrogen atmosphere had a positive impact on the strength,and, in addition, the strength is preserved even after 12 days of accelerated aging. With the goal to find modes to improve paper strength and stability, a mixture of polysaccharides was applied in combination with the plasma treatment. When compared with chitosane-based data, the immediate efficiency of the modification was higher, however, lower values were found after 12 days aging. From the viewpoint

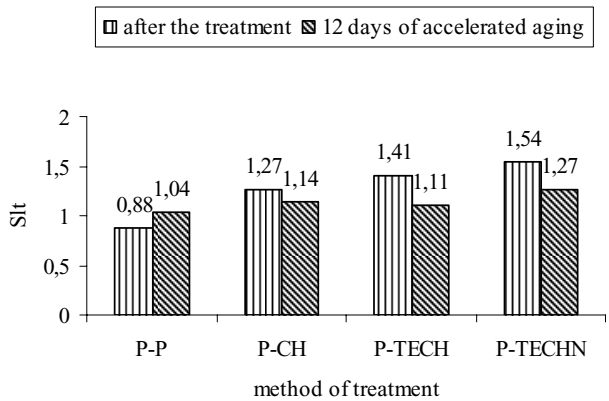

Fig. 1. **Efficiency of modification system expressed by ratio of tensile strenght modified and unmodified substrate (Slt = lt modified/lt unmodified) for samples: P-P – activation of paper with plasma, P-CH – modification with chitosane and activation with plasma, P-TECH – modification of paper with mixture of polysaccharides and activation with plasma, P-TECHN – modification of paper with mixture of polysaccharides in neutralising solution and activation with plasma**

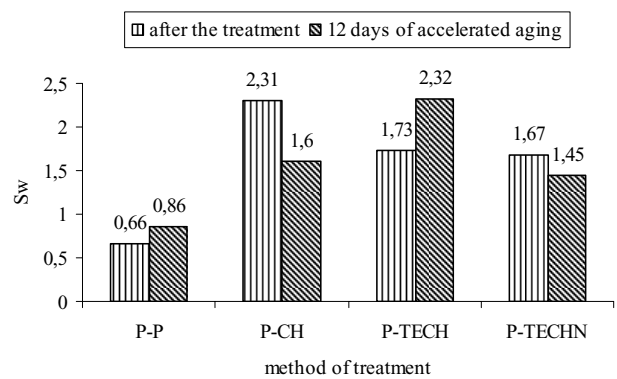

Fig. 2. **Chenge in folding endurance expressed by ratio of number of double folds of modified and unmodified substrate (Sw = wt modified/w unmodified) for samples: P-P – activation of paper with plasma, P-CH – modification with chitosane and activation with plasma, P-TECH – modification of paper with mixture of polysaccharides and activation with plasma, P-TECHN – modification of paper with mixture of polysaccharides in neutralising solution and activation with plasma**

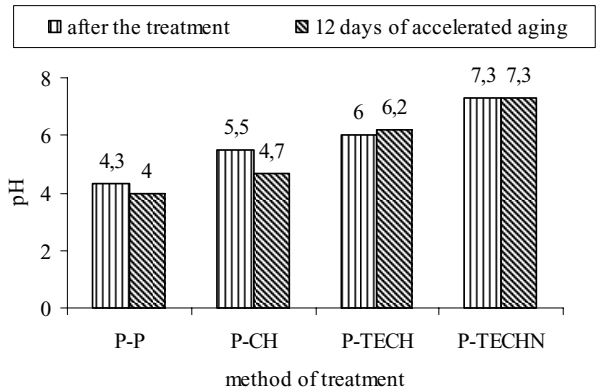

Fig. 3. **pH value of paper sample: P-P – activation of paper with plasma, P-CH – modification with chitosane and activation with plasma, P-TECH – modification of paper with mixture of polysaccharides and activation with plasma, P-TECHN – modification of paper with mixture of polysaccharides in neutralising solution and activation with plasma**

of aging, the results obtained at the substrate impregnation by a polysaccharide mixture in basic media are of interest. The modified substrate exhibited a higher tensile strength values after aging.

The effect of modification procedure on folding endurance can be seen in Fig. 2. While the combination of modification using chitosane and plasma treatment led to higher number of doublefolds immediately after application, the effect disappeared in the course of accelerated aging. Contrary, the use of modification mixture led to a lower immediate effect, however, the effect was more stable.

Other investigated parameter was pH of the tested material. It is known that degradation processes occur faster in acid groundwood paper and its pH value decreased in time. This is why the paper pH was increased by the modification performance. A small increase in pH is a consequence of chitosane application, the pH, however, decreased at aging. A change in the modification process led to both better results and pH stabilization. Substrate impregnation by a polysaccharide mixture seems to be the most effective mode of treatment, taking the mentioned parameter into account.

Changes in paper morphology due to the plasma impact and those induced by combined modification treatment were subjected to microscopic analysis. SEM pictures of the tested paper samples are shown in Fig. 4.–11.

It obviously follows from Fig. 4. and 5. that application of the plasma did not induce any destruction of the paper structure. It is worth reminding that the plasma influences only surface layers of the treated paper down to some hundreds of nanometers and the paper properties as a whole are preserved.

Substantial differences were not observed in SEM pictures when comparing the original untreated paper with that containing chitosane layer (Fig. 6.–7.). Chitosane being in the form of aqueous solution penetrates probably into the paper pores and does not cover surface fibres. Its presence is,

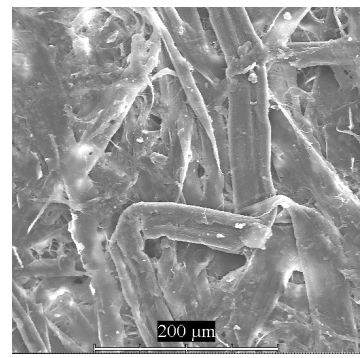

Fig. 4. **Original paper**

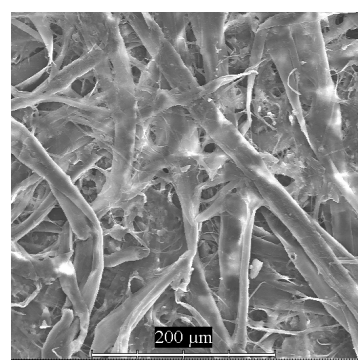

Fig. 5. **Paper activated with plasma**

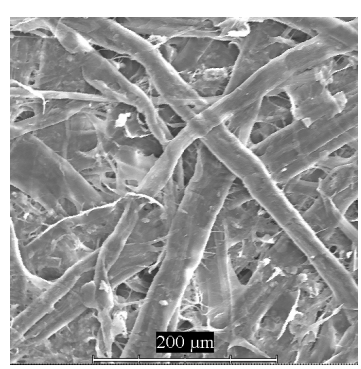

Fig. 6. **Paper treated with chitosane and activated with plasma**

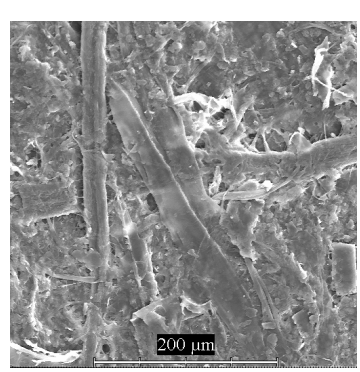

Fig. 7. **Paper treated with chitosane and activated with plasma after accelerated aging**

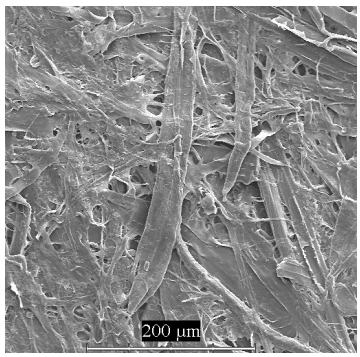

Fig. 8. **Paper treated with polysaccharide system**

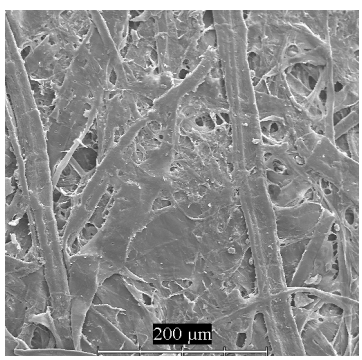

Fig. 9. **Paper treated with polysaccharide system and activated with plasma**

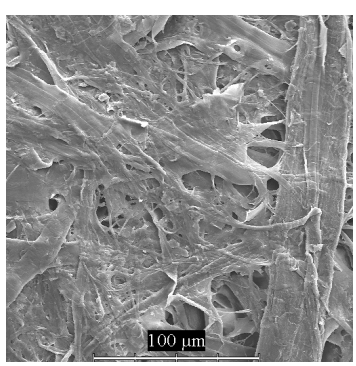

Fig. 10. **Paper treated with polysaccharide system**

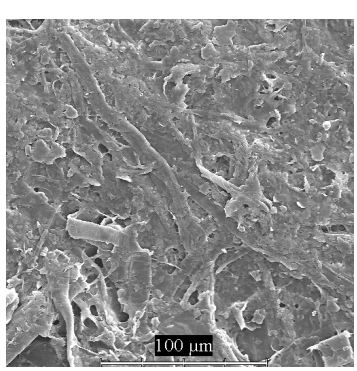

Fig. 11. **Paper treated with polysaccharide system after accelerated aging**

however, obvious in the paper samples after aging, where it is manifested through a more extensive pores filling. It can be supposed that due to heat action during aging, the chitosane layer undergoes changes yielding even cross-linked structures. Fig. 8.–9. illustrate the pictures of the paper modified by a polysaccharide mixture. The mixture stuffs the interfibres space and covers the surface fibres too. As evident from Fig. 11., the protection layer retains its homogeneity also after aging.

Conclusions

The contribution brings the results on evaluation of efficiency of paper modification by a combined action of plasma and polysaccharide-based additives. From the LCM tensile strength point of view, the best results can be reached using a polysaccharide mixture, consisting of a chitosane, water-soluble cellulose derivative and cationic starch. The use of this system leads to a sufficient folding endurance after the accelerated aging expressed by a coefficient S = 2.32. Evaluating this parameter, the application of a polysaccharide mixture in neutralizing solution seems to be disadvantageous. On the other hand, this system ensures a required alkaline reserve for acidic lignocellulosic material when undergoing degradation.

The authors thank Ministry of Education of the Slovak Republic for a support granted to the project No. 661/2003.

REFERENCES

1. Nihlstrand A.: Plasma modification of polypropylene materials for improve adhesion, *16* (1996).
2. Veprek S., Patscheider J., Elmer J.: Plasma Chem. Plasma Process *5*, 201 (1985).
3. Veprek S., Eckmann C., Elmer J. T.: Plasma Chem. Plasma Process *8*, 445 (1988).
4. Mukhopadhyay S. M., Joshi P., Datta S., Zhao J. G., France P.: J. Phys. D: Appl. Phys. *35*, 1927 (2002).
5. Mukhopadhyay S. M., Joshi P., Datta S., Macdaniel J.: Applied Surface Science, *201*, 219 (2002).
6. Vohrer U., Trick I., Bernhardt J., Oehr C., Brunner H.: Surface and Coating Technology *142–144*, 1069 (2001).
7. Felix J.: Chalmers dissertation, 1995.
8. STN ISO 1924-2: Paper and board. Determination of tensile properties. Part 2: Constant rate of elongation method.
9. STN ISO 5626: Paper. Determination of folding endurance.
10. STN 500374: Testing of pulp and paper. Surface pH measurement of pulp and paper.
11. Košík M., Šurina I., Blažej A.: Chemicke Listy, *77*, 177 (1983).
12. Košík M., Šurina I., Lapčík L., Rúčka I., Reiser V.: Chem. Papers, *37*, 843 (1983).
13. Šimkovic I., Šurina I., Vričan M.: J. Anal. Appl. Pyrol. *70*, 493 (2003).

L10 PROPOSAL OF NATIVE WOOD AS A NATURAL COMPARATIVE STANDARD FOR THE INTERPRETATION OF VOC MEASUREMENTS AND INDOOR AIR QUALITY ASSESSMENT

ANDREA BARTEKOVÁ, SVETOZÁR KATUŠČÁK and IGOR ŠURINA, MILAN VRŠKA

Slovak University of Technology, Faculty of Chemical and Food Technology, Department of Chemical Technology of Wood, Pulp and Paper, Radlinského 9, 812 37 Bratislava, Slovakia, svetozar.katuscak@stuba.sk

Introduction

The native wood has been achieving the highest environmental and hygienic quality in comparison with other building materials[1,2], which promotes its usage as a comparative bio-based material for environmental and hygienic evaluation of the building materials. The important component of a complex environmental and hygienic quality assessment[4,5] is evaluation of volatile organic compounds (VOC). The study of the VOC and of the recommended VOC limits continues[14–18], e. g. the U.S. Occupational Safety & Health Administration uses the Permissible Exposure Limits (PEL), the American Conference of Governmental Industrial Hygienists (ACGIH) recommends the Threshold Limit Values and the EC Environment Institute recommends the Lowest Concentration of Interests (LCI). However the *interpretation* of the measured VOC/TVOC emissions data has not been solved properly. The *natural* materials are healthier than *synthetic* and *chemicals*[6,21,22]. It is generally accepted that synthetic VOC can impair air quality and negatively affect health[6–9,11]. The other extreme – long term living in the *sterile* environment with zero emissions (VOC = 0) is not healthy either[10]. Positive effects of the natural VOC like α-pinene (1), β-pinene (2), nonanal (3), decanal (4), camphene, (5) and other VOC have been demonstrated[3,19]. Isoprene, monoterpenes and sesquiterpenes and other biogenic VOC emitted by plants exceeds at a global scale that of anthropogenic components released by man-made activities[20].

The aim of this work has been to evaluate the natural VOC emissions from important bio-based materials according to the PEL and LCI – the US and European VOC toxicological criteria for healthy environment. The aim is also to promote concepts of using natural bio-based materials as a comparative standard material for interpreting of VOC emissions and for development new materials. This recommendation is consistent with the systems said above[1–3,14,15,19,20] as well as with the concepts of building biology[21,22], (3), aromatherapy[23–27], immunology[28], dwelling medicine and other interdisciplinary concepts accepting natural materials containing no synthetic chemicals as the ideal limit for building materials as regards the hygienic and environmental quality.

Experimental

Wood samples were prepared from pine, spruce, beech, oak, locust, maple and mahogany woods (dimensions 20 × 19 × 2.5 cm) and were packaged into an aluminium foil. Sampling (Fig. 1.) and determination of VOC originating from the wood was carried out according[12]. The air volume of a sample[13] was in the range of 1–5 dm^3. Three parallel air samples were taken off after each 72 h, or when investigating the kinetics of VOC transformations after 0; 72; 98; 122; 146 h.

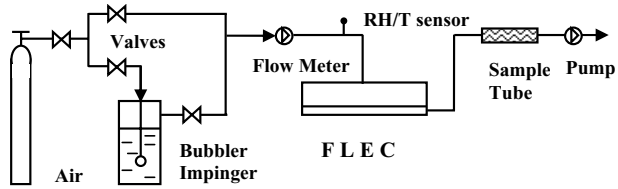

Fig. 1. **The diagram of the experimental set up for sampling of VOC**

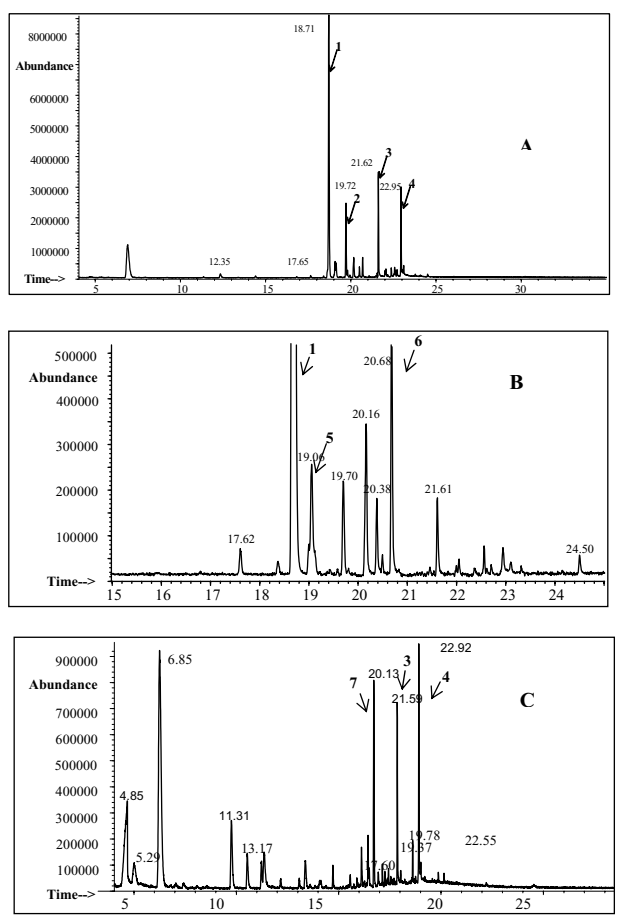

Fig. 2. **Chromatogram from GC-MS analysis of selected wood kinds: A. pine, B. spruce, C. oak. α-pinene (1), β-pinene (2), nonanal (3), decanal (4), camphene (5), 6-methyl-2-methylene--bicyclo [3.1.1] heptane (6), 2,2,9-trimethyldecane (7)**

VOC analysis equipment consisted of a thermodesorption unit (desorption was performed at 200 °C), a gas chromatograph (column: HP-1, 50 m × 0,32 mm × 1.05 μm) and mass spectrometer (energy of ionisation 70 eV).

Calculation of VOC and TVOC. The emission factor *E* and the concentration *C* in the FLEC were calculated from individual concentration data points[18].

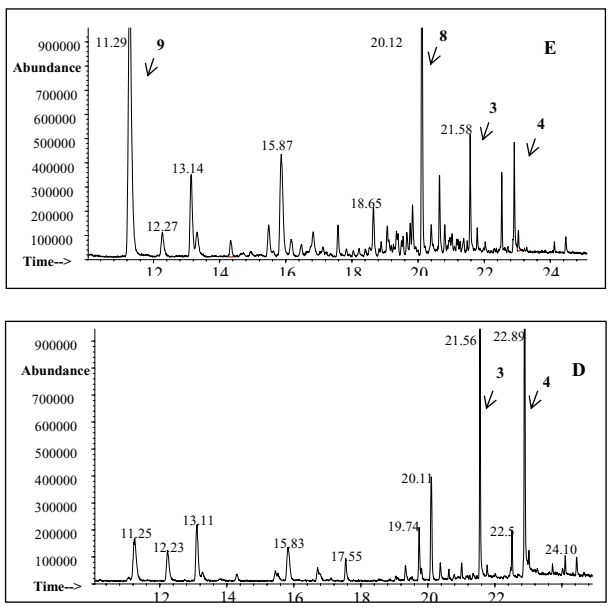

Fig. 3. **Chromatogram from GC-MS analysis of selected wood kinds: D. maple, E. beech nonanal (3), decanal (4), 2,2-dimethylhexane (8), 2,3-dihydro-4-methylfuran (9)**

Table I
The most significant VOC released from native wood after 72 hours following the unpacking the sample (t_0) and average concentration values C_{VOC} (mg m^{-3}).

Sample	The most abundant VOC and average values of their concentration C_{VOC} [mg m^{-3}]
Pine	α-pinene (0.205); nonanal (0.051); decanal (0.046); β-pinene (0.045)
Spruce	α-pinene (0.319); 6-methyl-2-methylene--bicyclo [3.1.1] heptane (0.023); camphene (0.018)
Beech	2,3-dihydro-4-methylfuran (0.024); 2,2-dimethyl hexane (0.010); nonanal (0.002); decanal (0.002)
Oak	2,2,9-trimetyldecane (0.008); decanal (0.006); nonanal (0.005)
Maple	decanal (0.016); nonanal (0.010)
Locust	decanal (0.012)
Mahogany	nonane (0.008); D-limonene (0.005)

Results and discussion

Chromatograms of VOC released from selected woods obtained by GC–MS analyses are shown in Fig. 2. and 3. The highest concentration 612.5 μg m^{-3} and emission factor values 137 μg m^{-2} h^{-1} were found in the case of pine.

It is obvious that the all concentration values C_{TVOC} (mg m^{-3}) (Fig. 4.) from softwood kinds (spruce and pine) are 5–7-times higher than those obtained from oak, beech, locust, maple or mahogany samples.

Critical evaluation according to the American Conference of Governmental Industrial Hygienists

According to the ACGIH[16] the TVOC concentration *after* 72 hours has to be ≤ 5 mg m^{-3}. The corresponding C_{TVOC} values (mg m^{-3}) measured after 72 hours are as follows: pine 0.443 mg m^{-3}, spruce 0.423 mg m^{-3}, oak 0.090 mg m^{-3}, beech 0.059 mg m^{-3}, maple 0.061 mg m^{-3}, locust 0.03 mg m^{-3} and mahogany 0.030 mg m^{-3}. The C_{TVOC} values are 11 to 166 times lower than the ACGIH limit value for the healthy building material.

The ACGIH limits *after 28 days* are to be $C_{TVOC} \leq 0.2$ mg m^{-3}. The corresponding C_{TVOC} after 28 days

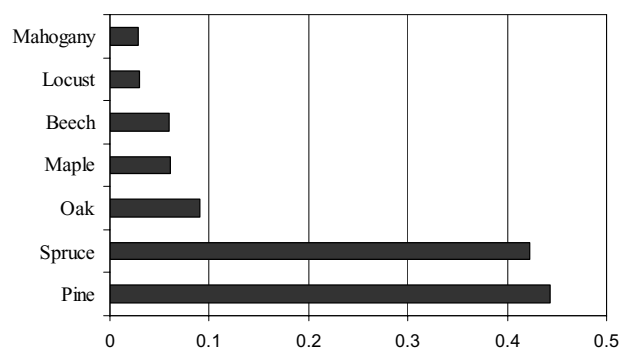

Fig. 4. Average concentration values C_{TVOC} (mg m^{-3}) from wood samples after 72 hours from samples unpacking (t_0)

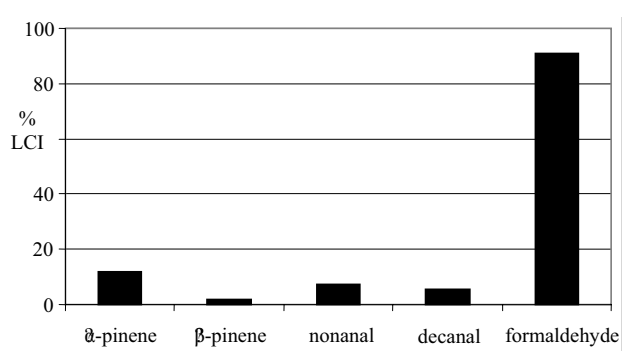

Fig. 5. **Average values of the most abundant substances in VOC emissions from pine wood sample expressed as % to the LCI value**

calculated from the kinetic VOC emissions measurements for the highest emitting pine wood is C_{TVOC} = 0.00496 mg m^{-3} which is 40 times lower than the ACGIH limit.

Critical evaluation of the natural wood VOC emissions related to the lowest concentration of interest LCI[17,18] is shown on Fig. 5. The LCI for both α- and β-pinene is 1 mg m^{-3}, for nonanal and decanal it is 0.4 mg m^{-3}.

It can be seen that the natural VOC emission from native wood is of some orders lower than the ACGIH and LCI limits for the healthy materials and even decreasing in time. It can be supposed that such dwelling environment is healthy for the human beings and their immunity system.

Conclusions

This work has shown that the native wood accomplishes both the VOC toxicological criterions of American Conference of Governmental Industrial Hygienists and the European Committee Environment Institute's the Lowest Concentration of Interest criteria for healthy material. The sterile environment with zero VOC is not suitable for long term living and can not be realised in practical life. The native bio-based material wood has been therefore recommended as a suitable comparative material for the interpretation of the results of the VOC measurements and as theoretical goal limit for development of new materials with the best eco--quality.

We thank Slovak Grant Agency (Project VEGA 1/0061/03) for its financial support.

REFERENCES

1. Gfeller B., Katuščák S., Höllmüller C.: Holzforschung *46*, 2, 25 (1994).
2. Michelozzi M.: *Ecological roles of terpenoid mixtures in conifers, Proceedings of the First Workshop of the Italian Working Group on Ecology of Plant Terpenoids*, Rome (Montelibretti) Research Area National Research Council, 1998.
3. Katuščák S., Gfeller B.: *Biocompatibility and Dwelling Ability*. EL & T, Bratislava 2002, eBook.
4. Levin H.: *Indoor Environmental Quality and Sustainability, Are They Compatible?*, California Interagency Working Group on Indoor Air Quality, Meeting Minutes, DHS Laboratory facility, Berkeley, CA, 1998.
5. US Environmental Protection Agency (1993): Life Cycle Assessment: Inventory Guidelines and Principles, (EPA/600/R-92/245). Risk Reduction Engineering Laboratory, Cincinnati, Ohio, USA.
6. Steinemann A.: Environmental Impact Assessment Review 24, 695 (2004). <http://www.ecomall.com/activism/rachel200.htm>
7. Salthammer T.: Chemie in unserer Zeit, *28*, 280 (1994).
8. Salthammer T., Marutzky R.: Holz-Zentralblatt, *144*, 2405 (1995).
9. Katuščák S.: Životné prostredie, *28*, 177 (1994).
10. Anon.: Is a totally clean environment good for you? <http://www.netdoctor.co.uk/ate/infections/202370.html>
11. Beseda I.: *Ekotoxikológia*. TU Zvolen 2004.
12. DIN 13419-3: Bestimmung der Emission von flüchtigen organischen Verbindungen (VOC), Teil 3: Verfahren zur Probenahme, Lagerung der Proben und Vorbereitung der Prüfstücke, CEN, (1999).
13. ISO/DIS 16017-1: Air Qualiy – Sampling and analysis of volatile organic compounds by the sorbent tube/thermal desorption/capillary gas chromatography – Part 1: Pumped sampling, International Standard, (1998).
14. Crump D. R., Squire R. W. and Yu C. W. F.: Indoor and Built Environment. *6*, 45 (1997).
15. Chuck Y., Crump D.: *VOC emissions from building products. Control, evaluation and labeling schemes*. Building Research Establishment. Digest *464*, 2002.
16. Anon.: Threshold Limit Values (TLVs^{TM}) for Chemical Substances and Physical Agents and Biological Exposure Indices (BEIs^{TM}), ACGIH Inc., Cincinnati, Ohio, 1995–1996.
17. Anon.: *Ausschuss zur gesundheitlichen Bewertung von Bauprodukten* (Committee for Health-related Evaluation of Building Products). Health-related Evaluation Procedure for Volatile Organic Compounds Emissions (VOC and SVOC) from Building Products, AgBB 2004, p. 1–18.
18. Barteková A.: *Environmental Quality of Lignocellulosics*. PhD Thesis. STU Bratislava, 2003.
19. Ourisson G.: Pure & Appl. Chem., Vol. *62*, No. 7, p. 1401–1404, (1990).
20. Ciccioli P.: *Role of biogenic VOC in photochemical smog formation, Proceedings of the First Workshop of the Italian Working Group on Ecology of Plant Terpenoids,* Rome (Montelibretti) Research Area National Research Council, 1998.
21. Schwarz J.: *Ökologie im Bau: Entscheidungshilfen zur Beurteilung und Auswahl von Baumaterialien*, 2. Aufl., Bern, Stutgart, Haupt, 1991.
22. Büeler B. et al.: *Positivliste – Bauökologische/ baubiologische Materialempfehlungen*, SIB, Gerber Bütschwill, 1995.
23. Corner J., Cawley N. and Hildebrand S.: International Journal of Palliative, Care Nursing, *1*, 67 (1995).
24. Lis-Balchin M.: *Aroma science: The chemistry & bioactivity of essential oils*. Surry, Amberwood Publishing, 1995.
25. Lis-Balchin M.: Aromatherapy Today, *7*, 24 (1998).
26. Guba R.: Aromatherapy Today, *3*, 21 (1997).
27. Guba R.: Aromatherapy Today, *4*, 5 (1997).
28. Mozelsio N. B., Harris K. E., McGrath K. G., Grammer L. C.: Allergy Asthma Proc. Jan-Feb; *24*, 73 (2003).

L11 LIGHT STABILITY OF INK-JET PRINTS

MILENA REHÁKOVÁ, VLADIMÍR DVONKA
AND MICHAL ČEPPAN
Department of Graphic Art Technology and Applied Photochemistry, Faculty of Chemical and Food Technology, Slovak University of Technology, Radlinského 9, 812 37 Bratislava 1, milena.rehakova@stuba.sk

Introduction

Digital printing is used in the full-colour large-format printing and sheet-fed printing of the conventional printing products. Selection criteria for specific digital printing technology are various. From the producer's point of view the speed, ability for long-time production charges and colour foreseeing are in interest; on the other hand the most determining for clients are the price and the final product quality. The light stability, aim of this work, is one of these criteria. Many factors influence the light stability of ink-jet prints in the ageing process, such as – printing technique, printing quality, chemical composition of paper or other printed substrate, surface treatment of coating, ink and other additives. Moreover the usage and storage conditions such as temperature, relative humidity, microbial contamination of paper affect the light stability of the prints.

The experimental work was devoted to the examining the light stability of different non-impact prints. We studied 4 samples printed by ink-jet technology and 2 samples printed by thermotransfer printing. The samples were exposed to the simulated daylight. Our attention was concentrated to the influence of the printed substrate on the light stability. The changes of chromatic and non-chromatic parameters were evaluated.

Experimental part

Printed materials

Two series of samples were examined. Inks used for the first set of prints (1–4) were assigned mainly for usage in interior (inks: water based inks HP; technology: ink-jet plotter HP 5000):
Sample 1: substrate: coated paper, 170 g m^{-2}, glossy
Sample 2: substrate: coated paper, 160 g m^{-2}, semi-gloss
Sample 3: substrate: polyester film, backlit, face side (non-printed)
Sample 4: substrate: polyester film, backlit, reverse side (printed).
The other set (5, 6) of samples was printed by special inks assigned for long-term outside using (inks: solvent based inks SCITEX, technology: SCITEX IDANIT NOVO):
Sample 5: substrate: PVC self-adhesive foil SCITEX, 2 years old
Sample 6: substrate: coated paper SCITEX, 150 g m^{-2}.

Methods

Studied parameters were measured up to 48 hours after sample printing. Subsequently the samples were exposed to simulated daylight. Device for simulating daylight consisted of MeX-lamp OSRAM POWERSTAR HQI TS 400/D UV-reduced and two fluorescent lamps with the maximum of emission spectrum in UVA, power 2 × 15 W, temperature 45 ± 5 °C, relative humidity 15 ± 5 %, exposure amount 105 klx in VIS, 25 W m^{-2} in UVA, exposure time 0–100 hours for samples 1–4, 0–140 hours for samples 5, 6.

The samples were exposed also to office interior light Philips TLD 36W/33 Standard 2850 Lm, distance from source 1 m, max. 1000 hours; and natural daylight filtered by window glass, max. 3 months (because of comparing of light source influence). Reference samples (non-exposed) were put into the darkness for 3 months.

Instruments

Spectrocolorimeter Spectrolino (Gretag MacBeth), densitometer X-Rite 428, CCD camera EDC 1000C (Electrim Corp.), microscope Janatech Inspection (Carl Zeiss Jena), stereomicroscope Leica MZ6, FTIR spectrophotometer Excalibur Series Digilab FTS 3000 NX (DRIFT method).

Results

Reflectance spectra

In the reflectance measurements of full-coloured areas before and after light exposition in dependence of wavelength (in the range of 380–760 nm), changes in the chromoforic system of particular colour compound were recognized. The shift of reflectance maximum in wavelength indicated colour changes. Relatively the least stable was sample number 2, samples 1, 3, 4 seemed to be more stable and no changes were observed for samples 5, 6. Mentioned phenomena distinctively occurred for all colours C, M, Y, K on sample 1 (Fig. 1.). Magenta, yellow and partly black demonstrated the increase in reflectance in the whole range of studied wavelengths, which indicated the bleaching of dye on the substrate. The shift of reflectance maximum of cyan testified a change in the colour hue.

Also the paper substrates changed their own colour (whiteness). The changes of spectra at the range 420–460 nm proofed this observation.

Total colour difference

Fig. 2. compares the light stability and the artificial daylight by means of total colour difference ΔE_{ab}^*. For simplification only CMYK colours are presented. Total colour difference ΔE_{ab}^* was calculated concerning the colour reference values L_0, a_0, b_0 of the non-exposed prints.

It is evident, that the most stable are special exterior inks on PVC substrate as well as on the coated paper. The total colour difference of any colour did not exceed value 10. From the samples assigned for exterior usage, the most stable were inks on PES substrate exposed from both the face and the reverse. The lowest light stability was noticed for sample 2, mainly the cyan colour (ΔE_{ab}^* about 30). Also the instability of used substrate contributed to this result (Fig. 2.).

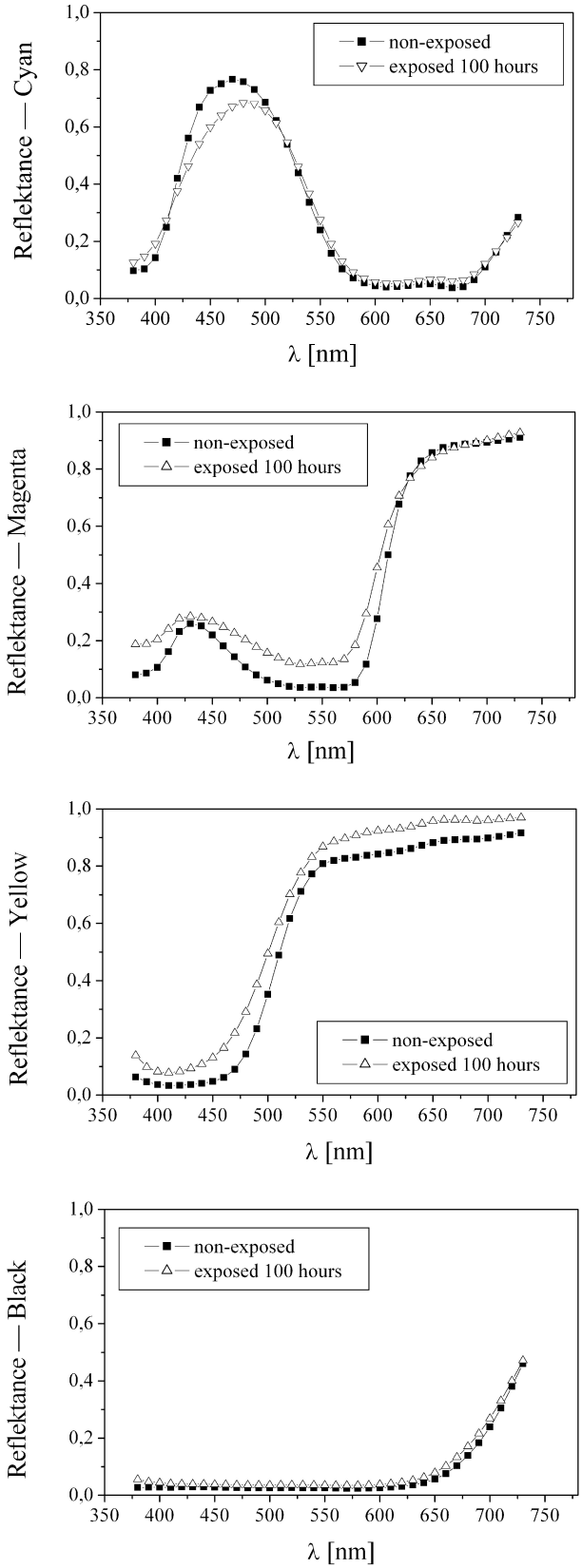

Fig. 1. **R = f (λ), sample 1**

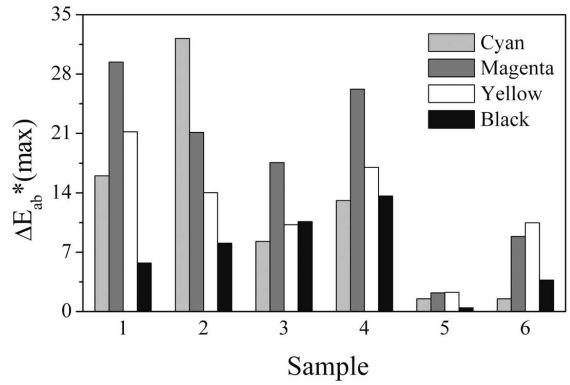

Fig. 2. **ΔE_{ab}^{*}(max) values for process colours of the samples 1–6**

Comparing the stability of colours, only yellow and black showed the same trends of behaviour on all substrates. Magenta and cyan showed different behaviour depending on paper or polymer. The lowest stability showed magenta.

The samples exposed to natural daylight gave similar results, maximal values of ΔE_{ab}^{*} were slightly lower (max. 25, black only 2.5). For samples 5, 6 assigned for exterior use were gained significantly better results, of course. ΔE_{ab}^{*} was always in the range of 0.5–10. Average colour differences measured after 2 months of natural daylight exposition present probably 100 hours exposition in the "light box".

Office light caused total colour difference (of "interior" samples 1–4) from 2 to 9, but differences between colour stability on the paper and polyester substrates were not obvious. Non-exposed samples showed ΔE_{ab}^{*} 0.3–1.3: practically without the colour change (Fig. 3.).

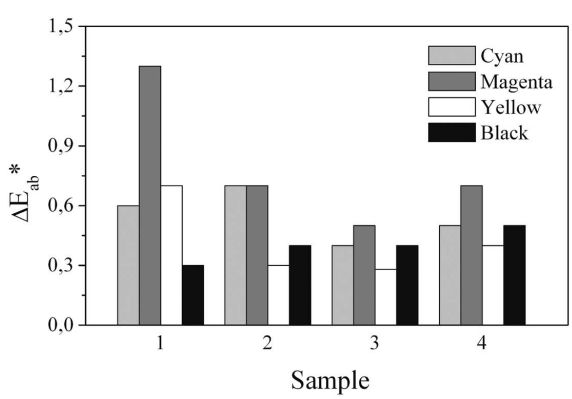

Fig. 3. **ΔE_{ab}^{*} of unprinted substrates, exposition time 100 h, accelerated light ageing**

Dot area changes

The Murray-Davis equation was applied to convert measured optical density of screen dots to dot area A for all samples. The function $A_{exp.} - A_{nonexp.} = f(A)$ was used as a parameter to examine light stability, because this function indicates reduction of screen dot size as a result of colour

bleaching. The bleaching of screen marginal area is the most notable in mid- and light tones (mostly 5–60% dot area). The results for all the samples supported this assumption. The 90 colour dot area remained almost intact. Fig. 4. documents the most significant decrease in dot area for magenta – 19 % at 40–60% dot area range; the slight decrease was observed for cyan and black – 11 %. Substantial changes on the samples 3, 4 were noticed only for 30–60 % of dot areas, hence we considered the PES foil as the most suitable substrate for ink-jet printing. Maximum decline was noticed for 50% area coverage. This fact confirmed the square shape of screen dot, which had the longest circuit at 50% dot area.

E d g e d e f i n i t i o n

Edge definition was measured on the interface substrate/printed solid. Exposure of samples caused the decrease in resolution and dot sharpness of the prints. The most distinctive changes were observed for samples 3 and 4, while in this term the paper substrates seemed to be more suitable. Moreover the measured parameters increased for the sample 2 and 1, which could be explained by additional reactions between substrate surface and dye. Evaluation of edge definition changes after 100 hours exposition in the light box are shown in Table I.

Table I
Comparison of light exposition effect on the changes of edge definition, samples 1–4

Quality of print	Sample 1	Sample 2	Sample 3	Sample 4
Cyan	Expressive lower	Slightly higher	Expressive lower	Expressive higher
Magenta	Expressive lower	Without changes	Slightly lower	Lower
Yellow	Expressive higher	Without changes	Expressive higher	Expressive lower
Black	Slightly higher	Without changes	Lower	Slightly lower

Low edge definition of samples 5, 6 before light exposition caused that these parameters were not investigated.

I m a g e r e s o l u t i o n

Image resolution was evaluated by monitoring the geometry of so called target "Siemens star". Significant differences between certain samples in the process of light ageing were not recognized. Considering the light source the most considerable differences of image resolution quality demonstrate the "light box", then the natural daylight. Office light did not influence this property.

W a t e r r e s i s t a n c e

Only samples 5, 6, which are designated for exterior usage, were used for this test. Colouring of wet filter paper which

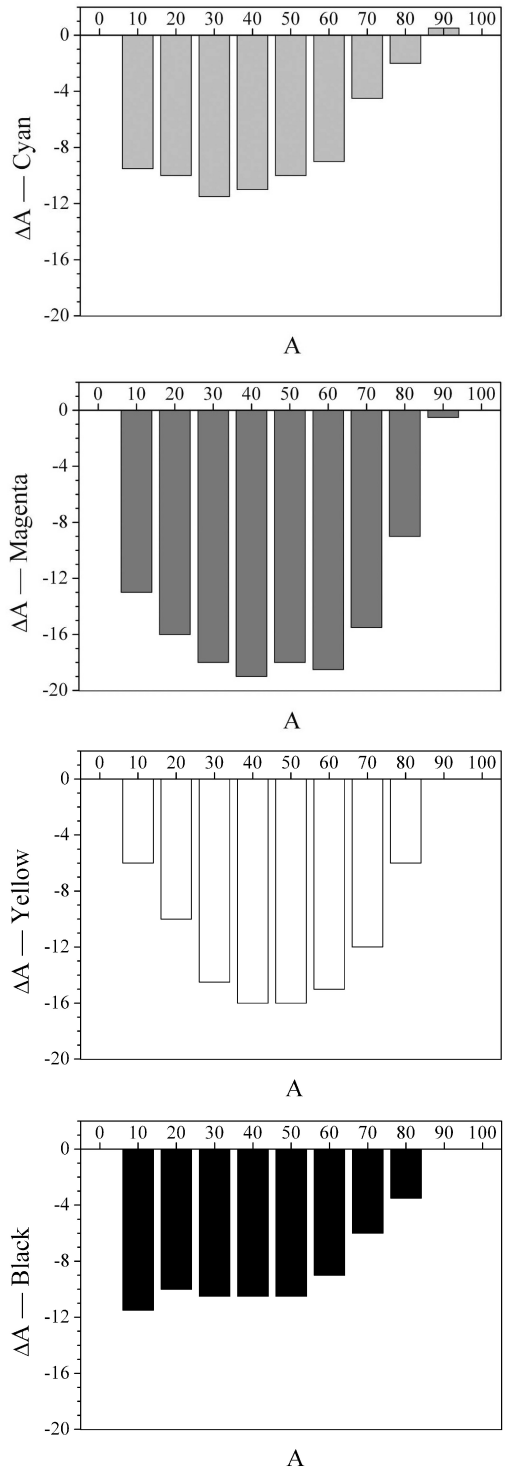

Fig. 4. $\mathbf{A_{exp} - A_{nonexp} = f(A)}$, **exposed 100 h, sample 1**

was in contact with colour samples and total colour difference after the test were observed. The effect of water didn't influenced the colour changes of the filter paper but ΔE_{ab}^{*} of original colour samples (Table II). According to the subsistent norm the water resistance of both samples was high.

Table II
ΔE_{ab}* after the water resistance test

Sample	ΔE_{ab}* Cyan	Magenta	Yellow	Black
5	12.8	6.8	6.3	0.7
6	7.2	3.1	11.4	0.6

F T I R s p e c t r a

To measure IR spectra of used substrates DRIFT method suitable for paper and other diffracting surfaces was used. No qualitative changes were proved. Increase of absorption peak at 1700–1750 cm^{-1} verified increase of free C=O groups caused by light induced reactions (Fig. 5.).

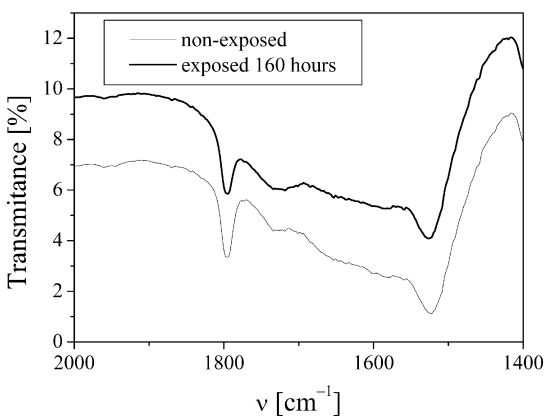

Fig. 5. **IR spectra of sample 6 before and after light exposition (160 h)**

Discussion and conclusions

The goal of this work was to study the light stability of ink-jet prints.

Considering the light source the most significant changes on all samples induced the accelerated daylight exposition. Average total colour difference was about 18. Natural daylight exposition filtered by window glass in time considerable to the same time interval as daylight exposition caused average ΔE_{ab}* 12.5. Office light in the summary exposition time 1000 hours caused colour changes expressed by ΔE_{ab}* value up to 4. Along with it, this is "the duration time" of printed matters for common usage in interior conditions. Presence of UV radiation in light can be the decisive impulse for the initiation of photochemical reactions, which is followed by the destruction of original pigments and dyes and also substrate structures.

Comparing used substrates it was determined PES foil to be the most suitable substrate followed by paper sample 1 (coated, glossy) and paper sample 2 (coated, semi-gloss). Differences between samples 1 and 2 were rather small.

In terms of non-chromatic parameters interpretation, the most suitable substrate was paper sample 1. Its coating favourably effected the edge definition during the exposure. On the other hand, the PES substrate showed unsatisfactory properties.

Concerning the stability of used inks, the best colour couldn't be appointed. Interactions with substrate and suitable combination played the important rule. Cyan and black were more stable, while yellow and magenta were less stable colours.

Samples printed with special exterior inks showed their excellent properties. Sample of self-adhesive foil (PVC) did not exceed value ΔE_{ab}* = 4 (C, K up to 2). Moreover water resistance, the important characteristic of these materials, was very good.

We thank the Slovak Scientific Grant Agency for the financial support (Project VEGA 1/2455/05).

We thank the Ministery of Education for financial support (Project 661/2003 KNIHA.SK).

REFERENCES

1. Ragauskas A. J., Lucia L. A.: American Inkmaker, *52* (1998).
2. Lavery A., Provost J., Sherwin A., Watkinson J.: *The Influence of Media on the Light Fastness of Ink Jet Printers*, Manchester, UK, 1998.
3. Lucas J.: *Keep your true color – Lightfastness and Weatherability Testing*, 2001.
4 . Wang J., Chen T., Glass O., Sagea J.: *Light Fastness of Large Format Ink-Jet Media*, Rhode Island, USA, 1999.
5. Barrow W. J.: *Permanence/Durability of the Book*, a two-year research program, Richmond 1963.
6. Anderson S., Kopperl D.: Journal of Science and Technology, *363* (1993).
7. Sistach M. C., Ferrer N., Romero M. T.: Restaurator *19*, 173, (1998).
8. Hunt R. W. G.: *Measuring Colour*, Ellis Horwood, London 1995.
9. Arney J. S. and Pray E., Journal of Imaging Science and Technology, (1999).

L12 THE EFFECT OF SURFACE PARAMETERS OF INKJET PAPER ON RATE OF INK PENETRATION

ŠTEFAN ŠUTÝ[a], JURAJ GIGAC[b], MILAN VRŠKA[a], PAVOL STREŽO[a], MICHAL JABLONSKÝ[a], RADOVAN TIŇO[a], KATARÍNA VIZÁROVÁ[a] and JANA KOZÁNKOVÁ[a]

[a]Department of Wood, Pulp and Paper and Department of Ceramics, Glass and Cement, Faculty of Chemical and Food Technology Slovak University of Technology, Radlinského 9, Bratislava, Slovak Republic, stefan.suty@stuba.sk, [b]Pulp and Paper Research Institute Bratislava, Lamačská cesta 3, Bratislava, Slovak Republic, gigac@vupc.sk

Introduction

The types of paper used for inkjet printing are non-coated, non-coated treated, or coated papers. The best papers for a high-quality photographic printing are coated papers, either matt or glossy. Matt coatings in inkjet papers typically contain pigments on silica basis, polyvinyl alcohol as a binder and an additive of cationic polymer. Amorphous silicates are used for their high porosity, hydrophilness and specific surface. These properties support high penetration of water-soluble inks, fast drying and sharp-defined edges of print points.

One of the important factors of quality in inkjet printing is the rate of ink penetration into the surface of paper. This parameter plays an important role in high-speed printing. An insufficient rate of ink penetration into the paper surface during the printing process could lead to ink smears and thus to devaluate and damage the printed sample. On the other hand, it is important that the ink gets fixed on the paper surface and does not penetrate into the deeper layer of the paper. Inside the paper surface the ink is optically less effective.

An ideal paper for inkjet printing should absorb the liquid phase of ink rather fast while the colour or pigment should get fixed on the surface. The colour fixed on the paper surface minimises feathering of edges and maximises light penetration on a visible picture[1].

The paper parameters that influence quality of print by inkjet technology are not yet fully identified. Some authors present the view that for a good quality of inkjet print a fast penetration of ink on one hand, and a high deposition of ink on paper surface on the other, are required. To produce a coloured picture of high quality, such systems of ink and paper should be used that would optimise edge sharpness, colour saturation and stability of image[2]. In this article[3]authors have monitored some properties of paper and their correlations with print quality. They have found out that porosity, ash content, smoothness do not correlate with print quality and that from the point of print quality only papers with certain penetration rate are suitable. The authors of the paper[4] have concluded that papers for inkjet printing should be hydrophilic, with highly porous surface without macroscopic structure. Penetration of liquids to the paper structure roughly observes similar laws as movement of liquids into capillaries under surface tension, and can be expressed by the Lucas-Washburn's s equation:

$$h = \sqrt{\frac{\gamma.r.t.\cos\Theta}{2.\eta}} \qquad (1)$$

Where h is a depth of penetration (mm), γ is a surface tension of liquid (N m^{-1}), r is a radius of capillary (nm), I is a time of penetration (s), Θ is an angle of wetting (°), η is a viscosity (Pa s). From the above-mentioned it can be seen that a liquid can penetrate into the paper structure only in the case that the angle of wetting is $\Theta < 90°$, because only then $h > 0$.

The dependence shows that the rate of penetration of liquids to papers depends on paper properties that are given by angle of wetting of paper surface, by radius of capillaries (porosity) and by properties of liquids, i. e. their surface tension and viscosity. The time during which paper is in contact with liquid is also an important factor. Thus, the rate of penetration can be influenced either by alterations in paper properties, or by alterations in ink properties.

This paper is focused on the rate of penetration of ink into paper. We have used a device on the principle of Bristow test. The principle of the test is based on precisely defined conditions under which a known amount of ink is applied (with a writing head) on paper at various speeds of paper movement. The rate of ink penetration on the paper surface can be calculated from the transfer curves.

The another aspect discussed in this paper is the relationship between paper parameters and coatings of inkjet papers and the rate of ink penetration into paper.

Materials and methods

P a p e r s

Several kinds of different commercially available paper have been used in the tests: a) non-coated b) coated matt paper and c) coated glossy paper. All coated papers were to be used for quality photographic print. The characteristic parameters of the papers have been investigated and the results are listed in Table I. The properties have been measured by standard procedures in accordance with STN ISO standards at Pulp and Paper Research Institute Bratislava.

I n k

The ink used in experiments was CANON BJC 2000 of black colour.

P o r o s i t y

To find out structure of paper, the samples were evaluated by mercury micro-porosimetry. This method can determine the following parameters of paper such as total specific volume of pores, specific surface of pores, average radius of pores and total porosity and distribution of pores that are characteristic for porous structure of paper. The results are given in Table II.

Table I
Characteristic parameters of inkjet papers

Sample	Characteristics	Type of coating	Basis weight [g m^{-2}]	Thickness [μm]	Paper mass per volume [kg m^{-3}]	Content of ash at 450 °C [%]
2	non-coated	–	82.1	96	855	17.7
3	coated	matt	110.8	140	791	27.6
6	coated	glossy	170.4	215	793	14
6B	double side coated	matt	180.1	211	854	23.9
10	coated		102.1	124	823	24.9
15	coated	glossy	137.6	164	839	17.3

Table 2
Parameters of porous structure of paper

Sample	Total specific volume, [mm^3 g^{-1}]	Specific surface [m^2 g^{-1}]	Average radius of pores [$\times 10^{-1}$ nm]	Total porosity [%]
2	518	4.15	20240	28
3	615	28.16	13020	50
6	650	17.98	23360	30
6B	570	24.68	13020	34
10	553	24.12	16230	27
15	513	21.82	20240	49

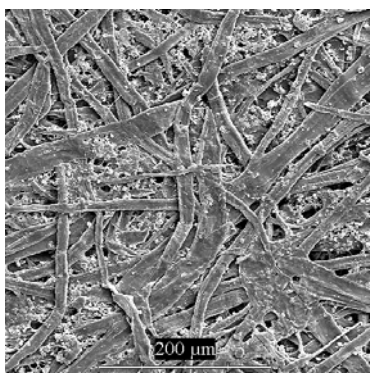

Fig. 1. **Sample 2**

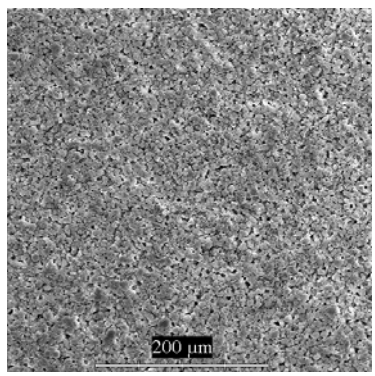

Fig. 2. **Sample 3**

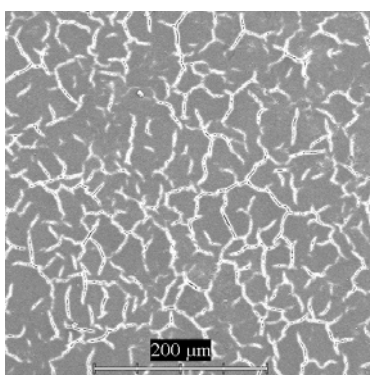

Fig. 3. **Sample 6**

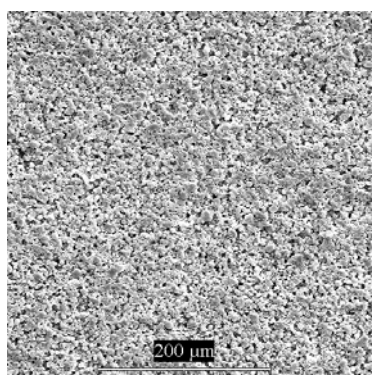

Fig. 4. **Sample 6B**

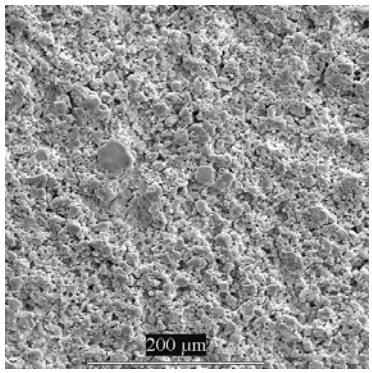

Fig. 5. **Sample 10**

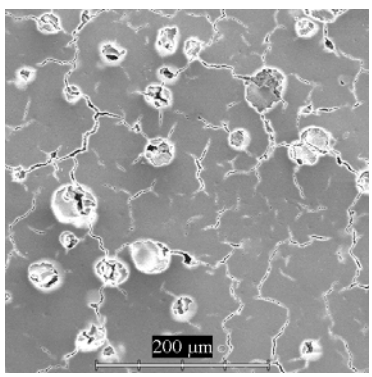

Fig. 6. **Sample 15**

S E M o f p a p e r s u r f a c e s

The samples of papers were analysed by SEM and the results can be seen in Fig. 1.–6. From Fig. 3. and Fig. 6. it can be seen that samples 6 and 15 have a glossy coating, their surfaces have only small cracks and are smooth. Sample 15 (Fig. 6.) has minute craters on its surface. Samples 3, 6B and 10 have matt coatings that are visible also in Fig. 2., 4. and 5. The surface of the samples is grainy and, compared with glossy samples, not so smooth. Samples 3 and 6B have their surfaces nearly equal and less rough than sample 10. Sample 2 does not have any coating and in Fig. 1. some particles of filler can be seen between the fibres.

Rate of Penetration of Ink on Paper Surface

To determine the rate of ink penetration into paper surface, a device operating on the principle of Bristow test was used. The Bristow test simulates writing lines on paper produced at various movement speeds of writing head on the paper. The faster the movement of writing head, the shorter the time of contact between the paper and the ink cartridge. The amount of ink that penetrates into the paper depends on the contact time and surface properties of the paper.

The ink flow in writing head can be expressed as:

$$Q = S.v = \frac{V}{t} \quad (2),$$

where Q is a volumetric flow (µl s^{-1}), S is area of effluence from writing head (mm^2), v is a rate of effluence (mm s^{-1}), V is a volume of liquid (µl), t is a period of effluence (s).

The amount of ink was defined by micropipette dosing. A period of effluence is given by a ratio between the length of line written (1) and the speed of movement of writing head on paper (v_{ph}):

$$t = \frac{l}{v_{ph}} \quad (3)$$

then:

$$Q = \frac{V v_{ph}}{l} \quad (4).$$

Thus, the rate of penetration of ink into paper can be calculated as:

$$v = \frac{Q}{S} = \frac{V v_{ph}}{Sl} \quad (5),$$

and for a circular opening of writing head it stands that:

$$v = \frac{V v_{ph}}{\pi r^2 l} \quad (6),$$

where r is a radius of the area of circular opening of writing head.

As lines are written on papers there occurs feathering in cross-direction vertically to the movement of the written line The rate of feathering can be calculated as a dependence between feathering to sides and contact time. The feathering to sides (g) can be calculated as:

$$g = \frac{h - d}{2} \quad (7),$$

where h is a the width of line in mm, d is a diameter of circular opening of the writing head in mm. Thus the rate of feathering will be:

$$v_{roz} = \frac{g}{t_k} \quad (8),$$

where t_k is contact time. The contact time is the time during which the writing head moves along a distance d. The contact time can be calculated as:

$$t_k = \frac{d}{v_{ph}} \quad (9).$$

The speeds of the contact head and the contact times for the experiments are listed in Table III.

The device used for the experiments consisted of a clamp holding the writing head and a paper shifter that could have its speed adjusted to eight different modes. The amount of ink into the writing head was dosed by a micropipette. After switching on the paper shifter, the writing head was lowered and a line was written. In such a manner the experiments were repeated at different speeds. On each paper lines of different length and width were obtained.

Table III
Speeds of writing head and contact times for listed experiments for d = 1.2 mm

Speed of writing head v_{ph} [mm s^{-1}]	Contact time t_k [s]
10.5	0.11
5.00	.024
2.50	0.48
1.00	1.20
0.50	2.40
0.25	4.80
0.10	12.0
0.05	24.0

Results and discussion

The lines drawn, the speed of paper shift, length and width of lines show the dependence of rate of ink penetration on the surface of paper. The dependence is shown in Fig. 7.

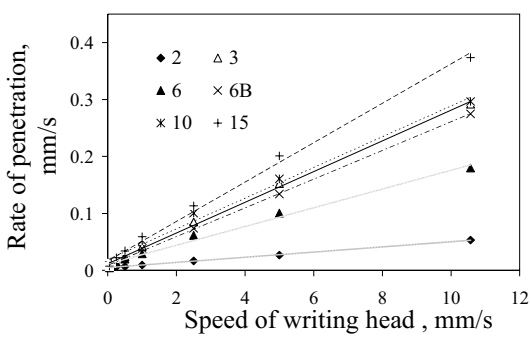

Fig. 7. **Dependence of ink penetration into paper on movement of writing head on paper**

The dependence was described by linear regression equations ($y = bx+c$). The equation parameters and the coefficient of determination (R2) are given in Table IV.

Table IV
Parameters of linear regression equations ($y = bx+c$) for dependence of ink penetration into paper at various speeds of writing head movement on paper.

Sample	Coefficient "b"	Constant "c"	Coefficient of determination, R^2
2	0.0046	0.0047	0.9995
3	0.027	0.0116	0.9973
6	0.0165	0.0108	0.9905
6B	0.0252	0.0088	0.9991
10	0.027	0.0187	0.9922
15	0.0346	0.0165	0.9951

Table V
Parameters of linear regression equation ($y = bx+c$) for dependence of feathering on various speeds of writing head on paper

Sample	Coefficient "b"	Constant "c"	Coefficient of determination, R^2
2	0.0408	0.0063	0.9989
3	0.2885	0.1133	0.9943
6	0.1231	0.0294	0.9944
6B	0.2417	0.1114	0.9871
10	0.2415	0.1717	0.9869
15	0.2838	0.1673	0.9897

From these equations the rate of ink penetration can be calculated at 0 movement of writing head on paper. If $x = 0$, then the equation is $y = c$. The constant c represents the rate of ink penetration into paper at zero movement of writing head (mm s^{-1}). The gradient (b) of linear dependence is a non-dimensional value that can be considered a rate constant of the penetration process. On the basis of this constant, different papers can be compared as to their rate of penetration.

The speed of movement of writing head on paper, as well as the contact time between paper and ink, influence feathering of lines. The higher the speed and the shorter the time, the lower feathering can be achieved. The dependence between the rate of feathering and the speed of writing head movement is in Fig. 8. Then the dependence was transferred to linear regression equation ($y = bx+c$). The equation parameters and the coefficient of determination (R2) are given in Tab. V. The rate of feathering of ink can be determined from the dependence of rate of feathering on speed of writing head movement by exploration to zero speed of the writing head. Constant c represents the rate of feathering at zero speed of paper movement (mm s^{-1}).

This paper also covers the aspect of parameters that influence the rate of penetration and feathering. It has been found (Fig. 9., Fig. 10.) that the rate constant of feathering

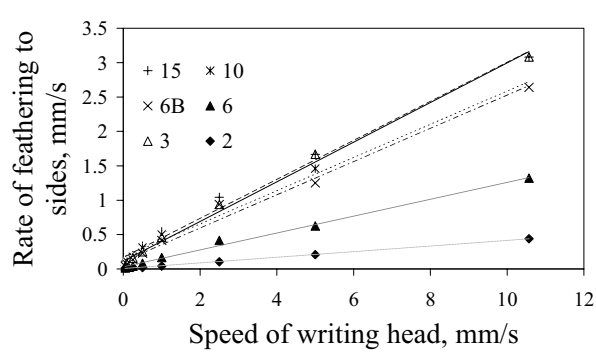

Fig. 8. **Dependence of rate of feathering to sides on speed of movement of writing head**

and penetration depends on specific surface of pores. The rate constant of feathering and penetration increases with growing value of the surface area of pores.

Further it has been found (Fig. 11.) that the average radius of pores depends on the content of residues that are ash content at 450 °C. The higher the residue of ash content, the higher the average radius of pores. At such a temperature the residue of ash content contains all mineral substances present in coatings and fillers including calcium carbonate.

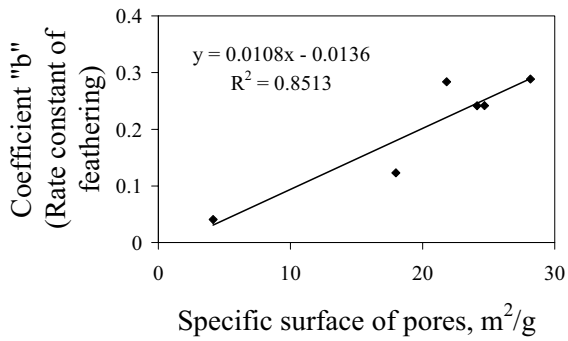

Fig. 9. **Dependence of rate constant of feathering on specific surface of pores**

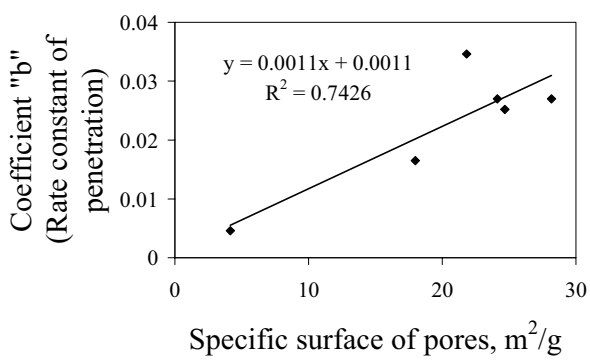

Fig. 10. **Dependence of rate constant of penetration on specific surface of pores**

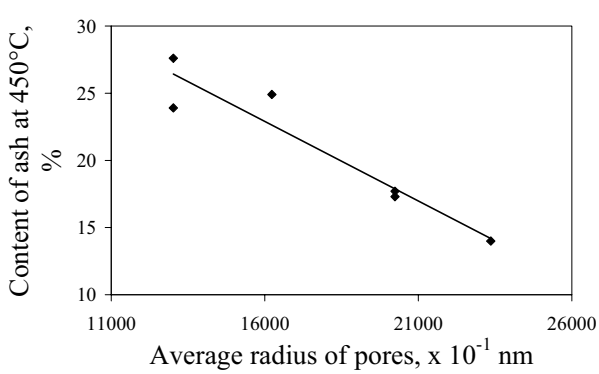

Fig. 11. **Dependence of average radius of pores on content of ash in paper**

Conclusion

The method on the principle of Bristow test, as listed above, is suitable for determining rate at which ink gets absorbed on the paper surface. The rate of ink penetration into paper surface depends on the properties of the actual paper surface as well as on the properties of ink.

From the dependence of rate of penetration and feathering and speed of writing head it is possible to determine the rate of ink penetration and feathering at zero speed of movement of writing head as well as to determine the rate constant of penetration and feathering that is a gradient of that particular linear dependence. On the basis of these parameters different types of papers can be compared as to their rate of penetration and feathering of ink on their surface.

The porous structure of papers has been evaluated and characterised by mercury porosimetry. This method allows to determine characteristics of porous structure of inkjet papers: total specific volume of pores, specific surface of pores, average radius of pores and total porosity. Other characteristics of paper, as basis weight, thickness, volumetric mass, roughness and content of ash (at 450 °C) have also been determined.

From the properties listed previously the dependence between the rate constant of penetration/feathering and specific surface of paper could be detected. It has been found out that the rate constant of penetration and feathering of ink into paper is influenced by specific surface of pores.

The average radius of pores depends on the content of coatings and fillers in the particular sort of paper that can be determined as non-combustible residue in the paper at 450 °C.

This paper was written and published with support from the Agency for Development in Science and Technology, APVT-99-007302.

REFERENCES

1. Ryu R. Y., Gilbert R. D., Khan S. A.: Tappi Journal *82*, 128 (1999).
2. McManus P. A..; Jaeger C. W.; Le H. P.; Titterington D. R.: Tappi Journal *66*, 81 (1983).
3. Bares S. J.; Rennels K. D.: Tappi Journal *73*, 123 (1990).
4. Lyne B. M.; Aspler J. S.: Tappi Journal *68*, 106 (1985).

L13 CONTROLLED PROCESS OF THE PRODUCTION OF MODEL AGED TEST PAPER IN THE SEALED REACTOR

MILAN VRŠKA[a] , RADOVAN TIŇO[a],
SHAHANI CHANDRU J.[b] and SVETOZÁR KATUŠČÁK[a]
[a]*Department of Chemical Technology of Wood, Pulp and Paper,* [b]*Department of Analytical Chemistry, Faculty of Chemical and Food Technology, Slovak University of Technology in Bratislava, Radlinského 9, SK-812 37 Bratislava, Slovakia,* [b]*Library of Congress, Washington D.C., USA.*

To advance the development of new substances, processes and equipment for the modification and/or stabilization of lignocellulosic carriers of information (LCI), it is useful to have access to an unlimited supply of naturally aged papers in desired states of deterioration. Since this is not always possible for most institutions interested in such research, the creation and use of model test papers with properties very similar to those of naturally aged materials in libraries and archives provides a practical solution. This work was aimed at the production and evaluation of batches of such model test papers produced using sealed reactors with controllled humidity and temperature.

The variability and distribution curves of the folding endurance, tensile strength, tensile energy adsorption (TEA) as well as the distribution of the scanned CIE Lab color parameters evaluated by Wood Scan Ecorex SK software of the produced model paper were measured and evaluated. The minimising of the variability of temperature, humidity of paper and relative air humidity was performed.

The comparison of the variabilities of original and aged papers showed possibility of the production of statistically homogeneous sets of papers.

Keywords: archives, libraries, paper, lignocellulosic carriers of information, accelerated ageing,

Introduction

To advance the development of new substances, processes and equipment for the modification and/or stabilization of lignocellulosic carriers of information (LCI)[1, 2] it is useful to have access to an unlimited supply of naturally aged papers in desired states of deterioration.

The creation and use of model test papers with properties very similar to those of naturally aged materials in libraries and archives provides a practical solution[1].

New undegraded acid paper considerably differs from the degraded acid paper mainly by decrease of optical and physico-mechanical properties[3].

Obtained results about differencies of deacidification procedure efficiency at the deacidification of new and degraded paper support need of increased using both the new and degraded test papers for the evaluation of new deacidification and strenghtening agents.

Testing of the impact of deacidification process on improvement of mechanical permanence is mainly being performed on new acid paper in spite of the state that deacidification process are dedicated for deacidification of old degraded paper, old books and old archival documents.

The meaning of the production method: new acid paper is not the degraded paper, characterised by low degree of cellulose polymerization, higher content of organic acids, carboxyls, carbonyl, furaldehyd, other degradation products and functional groups. Paper aged in sealed reactor should degrade similarly to the naturally aged paper[4]. So it is simply better model test paper for the testing of deacidification/ modification processes and equipments efficacy.

This work was aimed at the production and evaluation of batches of such model test papers produced using sealed reactors with controllled humidity and temperature.

Experimental

Materials. Newsprint paper used in tests has subsequent composition and properties: 55 % SGW, 20 % kraft pulp and 15 % waste paper and pH of paper was 6,0 ± 0,2. The stainless steel autoclave with 400 cm^3 volume was used for the testing (max 30 sheets) and next stainless steel sealed reactor (Fig. 1.) was made for testing of 1500 sheets. The variability of pH, humidity (w), mechanical and optical properties were observed on the paper from the stack of acid newsprint paper placed in the reactor. Papers were air conditioned for 24 hours at RH = 50 % ± 2 and T = 23 °C ± 1. The stack was formed from the previously air-conditioned papers and subsequently was put into the reactor. Stack was placed in the centre of the bottom of reactor and filled whole height of vessel (Fig. 1.). The reactor was hermeticaly closed and put ito the thermostat for 5 days at 100 °C with forced circulation of hot air around the reactor. After the 5 days the reactor was withdrawn, vent and cooled. After the opening the reactor, the humidity profile of single layers of the stack was measured. The measured layers were 10, 30, 50, 70 a 90 mm from the bottom of the reactor. The physico-mechanical properties of single layers was measured after the 24 hours of air conditioning.

Variability of properties was followed on the surface of sheets and also in dependence of height of the layer in the stack.

Fig. 1. **Sealed reactor for aging of paper**

HPLC analysis of acids. The condensate, created under aging conditions was analysed using HPLC method to determine volatile organic acids. Acetonitrile (LiChrosol for Chromatography, Merck, Germany), methanol of analytical grade (Merck, Germany), Milli-Q ultra purified water, phosphate

buffer at pH 2 with 5% methanol content were used. As standards, water/acetonitrilic solution of fatty acid (formic, acetic, propionic and butyric) with concentration 100 μg cm^{-3} were prepared. Liquid chromatograph HP 1090 (Hewlett-Packard, Waldbronn, Germany) equipped with nalytical column LiChrosphere 18 RP 125 × 4.0 mm, 5 μm, connected to Diode array UV detector HP 1090 Series II was used. Measured data were evaluated by means of Chemstation A.03.03 operating software. The analysis was carried with direct injection of the water solution to the analytical column. Analytes were separated by employing the gradient elution (that of LC mobile phase). Detection is accomplished with DAD-UV detector by processing responses at the wavelenght of 210 nm.

FTIR DRIFT analysis. The piece of paper sample (approximately area of 1 cm^2) was placed in a standard sample holder of Digilab Excalibur FTS 3000MX FTIR spectrometer. The FTIR spectra were recorded with the resolution of 4 cm^{-1} using DRIFT technique. Spectra were recorded over the range 400–4000 cm^{-1} as the average of 40 individual scans. After carefully realized baseline correction using OMNIC® software, all the measured spectra were transformed using Kubelka-Munk function (KM). The KM intensities of characteristic spectral bands were evaluated and mutually compared.

Results and discussion

Fig. 1. shows the dependence of the pH and folding endurance on time in dry heating aging (105 °C) and in control heating aging in sealed autoclave (100 °C). Considerable decrease of double-folds of the paper aged in sealed autoclave was observed. During the dry aging appeared decrease the pH about 1 while hermeticaly closed autoclave caused decreased of pH about 1.8.

At ageing of lignocellulosics in sealed autoclaves was used a stack of paper approximately 20 mm thick. A small amounth of condensate was observed. Analysis of this condensate was carried out in further test series with more paper sheets (a stack 100 mm thick – cca 1500 sheets of paper). Analyse showed under the aging of paper in sealed reactor the volatile organic acids are being released (Table II). They accelerate degradation of paper. After the aging in sealed autoclaves the significant influence on variability of pH wasn't observe.

Table I contains values quantifying the variability of pH, humidity, folding endurance, tensile strength and other mechanical properties as well as the optical properties characterizing a change in optical parameters of papers in aged stack.

Fig. 2. suggest a dependence of pH variability between thickness of stack and different points on the paper surface. From results in figures 3 it is possible to see that the aging process is uniform across the stack. The variability of pH, isn't function of dimension of reaktor.

A little differences was observed in folding endurance (coefficient of variance CV = 27.28 %) and mechanical properties such as breaking length (Table II). The results in stretch of paper suggest decrease of elasticity of paper, while this decrease is independ on dimension of paper stack but it is observed as a universal phenomenon (CV = 0.03 %). Generally it is possible to say, that the variability of aged paper properties depends on its heterogenity and doesn´t depends on conditions in reactor.

No meaningful statistical difference between non aged/original paper and control aged paper was observed.

Cluster analysis of optical properties (L, a, b) (Fig. 4.) shows homogenity of original and aged test paper. Aged test paper has lower variance of optical properties than original paper (as seen in Table I) and from this point of view is possible to say, that aging in sealed reactor has positive effect on homogenity of aged file.

Table I
Variability comparison of physical and mechanical properties of original and sealed ageing paper

	Original paper			Aged paper		
	CV [%]	Average	St. dev	CV [%]	Average	St. dev
pH	0.58	5.18	0.03	1.21	4.13	0.05
Humidity [%]	1.29	5.17	0.067	3.22	5.20	0.17
Folding endurance	27.18	441	119.7	27.28	5.38	0.70
Tensile strength [MPa]	7.29	30.06	2.19	17.69	20.35	3.60
Breaking length, m	10.49	4120	432.1	17.39	3208	558
TEA [MJ]	15.95	19.94	3.18	2.28	8.45	1.51
Stretch, %	7.30	1.5	0.11	0.03	1.03	0.19
E, MPa	18.52	1595.1	295.4	28.35	1210.1	343
L	1.24	118.27	1.47	0.98	130.72	1.28
A	7.99	33.64	2.69	16.75	12.03	2.01
B	7.34	12.95	0.95	45.19	1.52	0.69
C	7.08	36.07	2.55	16.38	12.15	1.99
H	2.94	68.86	2.02	4.48	82.55	3.70

Table II
Results from analysis of condensate from sealed ageing of newsprint paper.

Sample	Formic acid [μg ml^{-1}]	Acetic acid [μg ml^{-1}]
Condensate from sealed ageing of newsprint paper	3625	3598

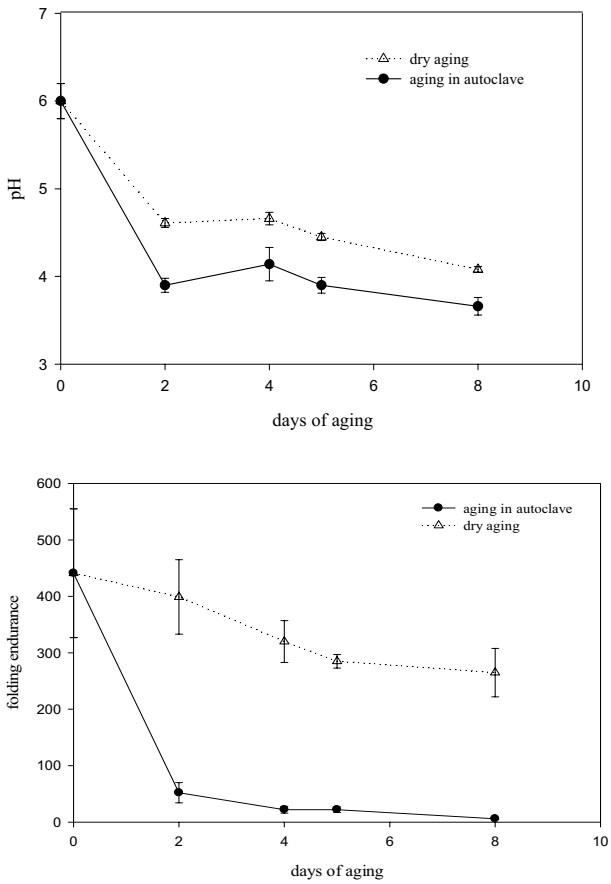

Fig. 2. **Comparison of pH and folding endurance of paper aged in sealed autoclaves**

F T I R a n a l y s i s

As it is demonstrated at Fig. 5., the thermally accelerated ageing process can be very effectively monitored by means of FTIR DRIFT spectroscopy. As a result of ageing, the degradation of paper samples occur, accompanied with the changes in physical properties and chemical structure. The main observable changes are in the hydrogen bonds network structure, as well in the content of carbonyls, degree of polymerization, due to which the content amorphous vs. crystalline phase changes.

These changes lead to consecutive production of low--molecular weight carbonyls and ketones, as well as the pro-

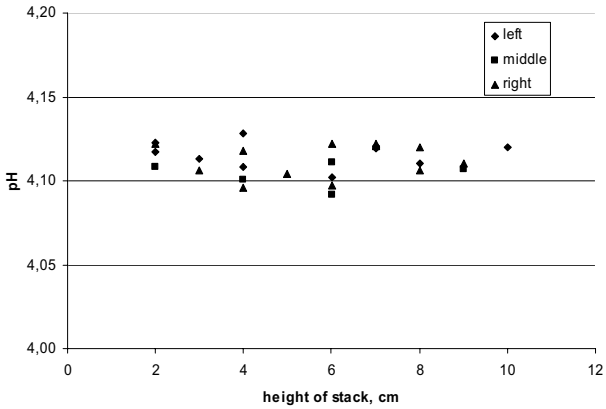

Fig. 3. **Variability of pH in different thick of paper stack**

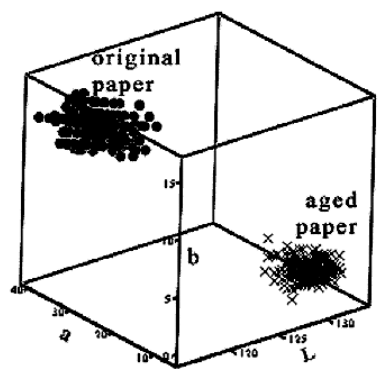

Fig. 4. **Cluster analysis of optical properties (L, a, b)**

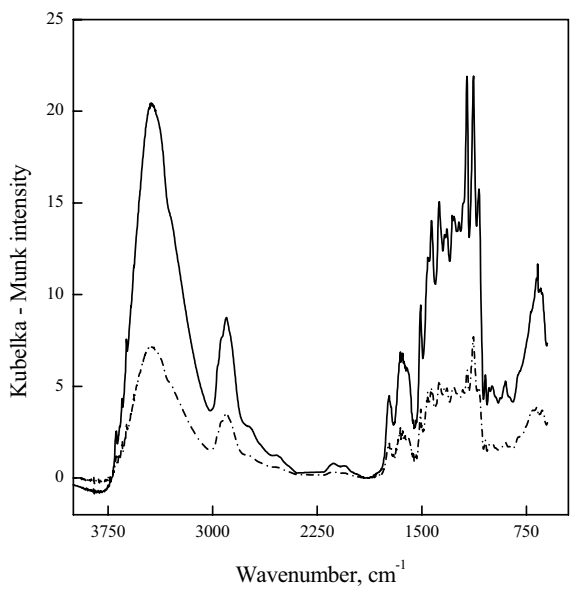

Fig. 5. **Experimental DRIFT FTIR spectra of newsprint paper (paper mill Větřní, pH 6 average weight 45 g m^{-2}), measured with resolution of 4 cm^{-1} for reference (untreated sample) (—) and for sample, aged for 5 days at 100 °C and RH 50 % (---). The spectra are the average of 40 individual scans**

duction of carboxylic acids and esters, immediately desorbed from the paper sample surface.

Conclusion

The new method of controlled production of model aged test paper is being developed. At the beginnig the kinetics of aging in the tube autoclaves on the set of 30 sheets of paper was measured. Subsequently were choosen the appropriate conditions for approval of variability in the bigger horizontal square shaped reactor containing set of 1500 sheets. The minimising of the variability of temperature, humidity of paper and relative air humidity was performed. The comparison of the variabilities of original and aged papers showed possibility of the production of statistically homogeneous sets of papers regarding variability/homogenity of pH, humidity, folding endurance and CIE Lab optical properties.

REFERENCES

1. Shahani Ch.: *The Evolution of a New Accelerated Ageing Test for paper*. Durability of Paper and Writing. Proceedings of the International Conference, 2004, Ljubljana, Slovenia.
2. Hanus J., Katuscak S., Katuščák D., Bukovský V., Rychlý J.: *Integrated Effort for Paper Cultural Heritage Preservation in the Slovak republic*. Durability of paper and Writing, Proceedings of the International Conference, 2004, Ljubljana, Slovenia.
3. Shahani CH. J.: *Accelerated Aging of Paper: Can it Really Foretell the Permanence of Paper*. Library of Congress, Washington D. C., 1995.
4. Cedzová M., Vrška M., Katuščák S.: Chemical Papers (2005). In press.

L14 THE PHASE TRANSFORMATIONS IN BI-2212 SUPERCONDUCTING SYSTEM IN VARIOUS PARTIAL OXYGEN PRESSURE

PETR VESELÝ, PETR PTÁČEK and JAROMÍR HAVLICA
[a]*Brno University of Technolgy, Faculty of Chemistry, Institute of Material Chemistry, Purkyňova 118, Brno, CZ-621 00, Czech Republic, p.vesely@centrum.cz*

Abstract

This work is focused on investigation of the phase transformation of Bi based superconductor. Influence of the partial oxygen pressure on the equilibrium temperature of phase transition of $Bi_2Sr_2CaCu_2O_{8+\delta}$ was determined by DTA. Tested superconducting material was prepared via sol-gel process where EDTA (Chelaton II) was used for preparation of the stable complexes with metal ions. Gel precursor was calcined at 500 °C (0.5 h) and sintered for 24 h at 860 °C in the air atmosphere. This material was in next investigated by DTA and optical microscopy at high temperature.

Introduction

High temperature oxide superconductors derived from Bi (BSCCO) are today studied extensively, due to their potential application in superconductive devices and equipments at superconductive transition temperatures above 100 K[1]. This material discovered by Maeda at al.[2] includes three phases of bismuth superconductor. $Bi_2Sr_2CuO_{6+\delta}$, commonly termed as Bi2201 phase, with T_c in range 10–20 K. The second phase $Bi_2Sr_2CaCu_2O_{8+\delta}$ (Bi2212) and third $Bi_2Sr_2Ca_2Cu_3O_{10+\delta}$ (Bi2223) having T_c 85 and 110 K, respectively[3].

The preparation of single phase is difficult without knowledge of phase relations in Bi-Sr-Ca-Cu-O system and mutual reactions of component. Not only thermodynamics factors participate on the formation of superconducting phase, but also on the kinetics of non-equilibrium growth processes[1,4].

Experimental

Starting components $SrCO_3$, $CaCO_3$ and CuO (Lachema, p. a.) were dissolved in diluted three solutions of HNO_3 (Lachema, p. a.). Fourth solution contained water and $Bi_2(NO_3)_3$ added as $(Bi_2(NO_3)_3 . 6H_2O$, Lachema, p. a.). Exact concentrations of prepared solutions were determined by $C_{10}H_{14}O_8N_2Na_2 . 2H_2O$ (Chelaton III, Lachema, p. a.) titration. To dissolute stoichiometric amount of EDTA II ($C_{10}H_{16}N_2O_8$, Lach-Ner, p. a.), the $Bi_2(NO_3)_3$, $Sr(NO_3)_2$, $Ca(NO_3)_2$ and $Cu(NO_3)_3$ solutions were subsequently added in the molar ratio 1 : 2 : 1 : 2. In next, pH of this solution was adjusted at value in range 7–8 by NH_4OH (Lachema, p. a.). Water was partly evaporated from the solution at 80 °C. During this process the mixture of stable metal complexes (BiY^-, SrY^{2-}, CaY^{2-} and CuY^{2-}) came to transparent blue gel. This gel precursor was calcined at 500 °C (0.5 h) and sintered for 24 h at 860 °C in the air atmosphere. This material was in next investigated by DTA and optical microscopy at high temperature.

Results and diskusion

Temperature of phase transition of the Bi2212 superconducting phase is depended on the partial pressure of oxygen. This was determined by TG-DTA (*TG-DTA analyzer SETARAM* 92-18) in the controlled Ar-O_2 atmosphere. Par-

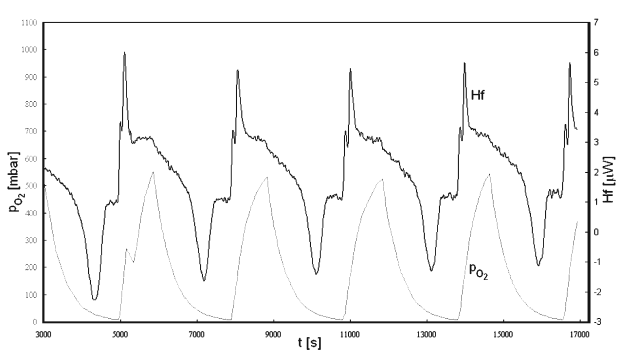

Fig. 1. **The isothermal step of TG-DTA at 860 °C**

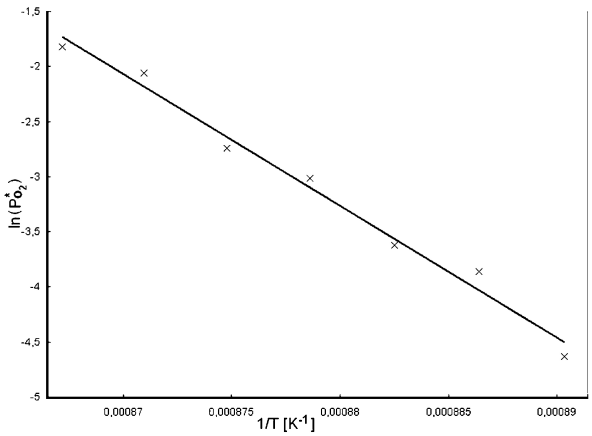

Fig. 2. **Dependence of $P^*_{O_2}$ pressure on to the reciprocal phase transition temperature**

tial pressure of oxygen was periodically changed between 0–600 mbar at constant temperatures. Heating and cooling steps of thermal analysis was also monitored. Plot of isothermal annealing at 860 °C is shown for some changes of partial pressures of oxygen in Fig. 1. Equilibrium p_{O_2} was determined at each 5 °C in temperature range 850–880 °C. This temperature range was located in thermodynamic stability area of Bi2212 determined in the phase diagram published by B. Liang at al.[5]. Results are summarized in Fig. 2. by dependence of relative pressure of oxygen $P^*_{O_2}$ on reciprocal temperature.

Conclusion

Phase transition in Bi2212 superconducting system depends on partial pressure of oxygen. TG-DTA results (Fig. 1.) lead to conclusion, that transformation proceeds reversible and the diffusion of oxygen both from Bi and into Cu layers corresponds to various p_{O_2}. From measured of equilibrium p_{O_2} and temperature was constructed the phase diagram on Fig. 2. The dependence may be described by linear equation:

$$\ln P^*_{O_2} = -\frac{119563}{T} + 101.95$$

REFERENCES

1. Suzuki T., Yumoto K., Mamiya M., Hasegawa M., Takei H.: Physica *C301*, 173 (1988).
2. Maeda H., Tanaka Y., Fukutomi M., Asano T.: Japanese Journal of Applied Physics *27*, 209 (1988).
3. Bhargava S. C., Chakrabarty J. S., Sharma R., Tomy C. V., Malik S. K.: Solid State Communications *78*, 397 (1991).
4. Park N.-B., Park Y.-P., Kim J.-H.: Current Applied Physics *3*, 481 (2003).
5. Liang B., Lin C. T., Shang P., Yang G.: Physics *C383*, 75 (2002).

L15 MODIFICATION OF A SURFACE OF COLLOIDAL SIZE SILICA PARTICLES BY CHEMISORPTION OF 2-PROPANOL VIA AZEOTROPIC DISTILLATION PROCESS

PETR PTÁČEK[a], JAROMÍR HAVLICA[a] and IVO KUŘITKA[b]

[a]Brno University of Technology, Faculty of Chemistry, Institute of Material Chemistry, Purkyňova 118, Brno, CZ-621 00, Czech Republic, ptacek@fch.vutbr.cz, [b]Polymer Centre, Faculty of Technology, Tomas Bata University in Zlin, Zlin, CZ-762 72, Czech Republic, ivo@kuritka.net

Abstract

The surface properties of colloidal silica particles have been changed by chemisorption of 2-propanol on to silanol (≡Si–OH) groups in anhydrous medium via azeotropic distillation. Sodium ion stabilized silica sol was used as a source of the amorphous SiO_2 particles with diameter in range 9–15 nm for utilization in sol-gel process. The hydroxyl groups (–OH) on surface were replacing by alkoxy groups ($–OC_3H_7$). The chemisorption of C_3H_8O on silica surface was carried out in the ternary azeotropic system isopropanol-water-benzene. The main advantage of this process is low temperature for the substitution of the isopropoxy groups for the silanols and the possibilities to the recycling of the chemicals after the esterification. DTA and FTIR methods were used for the characterization of the prepared precursor.

Introduction

The sol-gel process is a chemical synthesis technique for producing an oxide network at lower temperature than classical melting technology[1]. This way has been used for several years now to be efficient for the processing of thin oxide films, especially for the deposition of vitreous SiO_2 layers[2]. Thin films of sol-gel of derived oxide glasses may be used for coatings on to various substrates (glass, ceramics and metals) to improving mechanical, thermal, optical, protective and electrical properties[2] and optical sensors applications[3]. In other hand, bulk material prepared by the sol-gel process are very usefull for production of aerogels[4], low density xerogels[5], porous glasses[6], conductive gels[7] and etc. Important advantages sol-gel offers method due to purity, homogeneity and possibility for modification of resulting material properties by changing of conditions during its preparation[8].

Chemical and physical character of the silica surface may be altered by interaction with a various organics molecules as is PVA, PVP, PMMA, ORMOSILs etc.[9,10]. The efficiency of the modification depends upon the type of bonds, which are formed among silanol on silica surface and functional groups of the modifying proadhesive compounds. Chemical modification of amorphous silica surface has been studied with respect to number of publications extensively, because these materials may be utilize in many applications, such as chemically bonded phase in chromatography, extraction of

cations from aqueous and non-aqueous solvents, catalytic or ion-exchange reactions, electronics and ceramics[11,12].

Silica particles are today commonly used as fillers, polishing materials, pigments and reinforcement material for its nonporous and hydrophilic characteristics. Presence of various kinds of silanol groups (isolated, vinicial, geminal etc.) on the surface lead to hydrophobic behavior of silica particles[13]. Adsorbed water on silanol groups causes a aggregation of silica particles. Improving of material properties may be achieved by change of surface to hydrophobic[14]. Surface of particles dispersed in liquid medium may be modified via reverse micelles method[15], liquid precipitation method[16] and sol-gel process[17].

Experimental

During experiments, the colloidal solution of silica (Tosil, 30% mass SiO_2) has been slowly (0.1 ml s^{-1}) added into stirred 2-propanol (LACHEMA, p. a.). Benzene (LACHEMA, p. a.) was added (0.2 ml s^{-1}) in next step. This order may restrict coagulation of particles by better interaction between polar hydroxyl in alcohol molecule and polar surface of colloid particle. Reverse sequence lead to extend of coagulation accompanied by the increasing of particle size. The mixture was introduced in reboiler contained C_3H_8O, C_6H_6, H_2O and SiO_2 in molar ratio 1 : 0.36 : 0.30 : 0.04. Composition of the liquid phase of dispersion was balanced in to the first region of ternary system 2-propanol-water-benzene (Fig. 1. (A)). This is necessary, because, pure 2-propanol may be remained in reboiler at the end of the azeotropic distillation only from mixture situated in this area of composition.

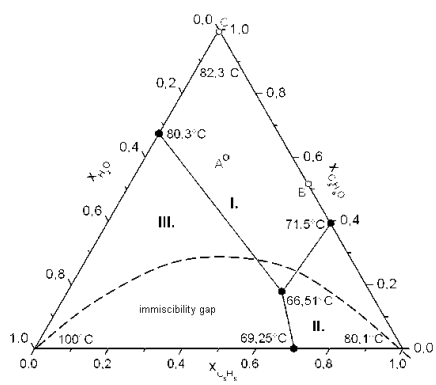

Fig. 1. **Phase diagram of ternary water – 2-propanol – benzene system**

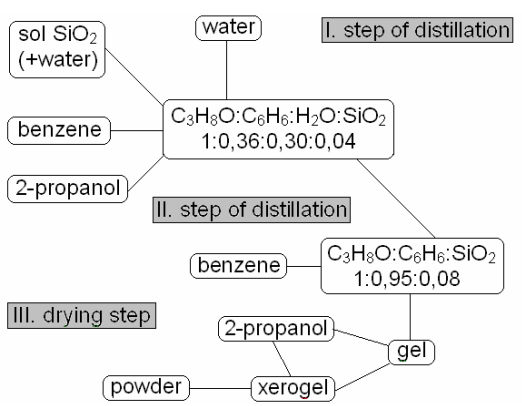

Fig. 2. **General scheme modification of surface silica particles**

The system H_2O – C_3H_7OH – C_6H_6 exhibits a heterogeneous azeotropic behavior and an immiscibility gap in a limited area of ternary compositions. Azeotropic distillation forms the suitable conditions for realization of 2-propanol chemisorption on the silica surface. Water is eliminated from reaction mixture at first. Secondly, the low content of water, which is produced during reaction between silanol and 2-propanol species along of Eq. 1, is maintained by this method. Equilibrium of the reaction is such shit to chemisorption and blocks the reverse course of reaction, i. e. hydrolysis of alcoxygroups.

$$\equiv Si_{(surface)}–OH + ROH \leftrightarrow \equiv Si_{(surface)}–OC_3H_7 + H_2O \quad (1)$$

At the beginning of distillation, the composition profile at the column was formed. Equilibrium between vapor and the liquid phase, which condensed on the surface of a glass spheres in distill column. In first step of synthesis, the composition of reaction mixture was continuously shifted towards the ternary azeotropic point. The heteroazeotrope accumulated in decanter consists from two immiscible liquid phases, because ternary azeotropic point is placed in immiscibility gap. Upper organic liquid layer consisted from mixture of benzene and isopropanol is refluxed back in the column. Main amount of water contained in lower liquid layer has been removed continuously from decanter. At the end of the first step, only 2-propanol and benzene (Fig. 1., (B)) remain in reboiler. In the binary system alcohol and benzene divided by azeotrope point, the initial composition of reaction mixture is in the part with higher content of 2-propanol. Distillation of this system leads to dividing of system on dispersion of the silica particles in pure 2-propanol in reboiler (Fig. 1., (C)) and binary azeotropic mixture in decanter.

In next, C_3H_8O was slowly evaporated from the dispersion. Gel produced at first period of this process subsequently come to xerogel. Final product, obtained by mechanical dispergation of the xerogel, is silica particles with the chemisorbed layer of 2-propanol on their surface. Described process is schematically presented in Fig. 2.

Results and discusion

Properties of the prepared powder of SiO_2 particles with isopropoxy groups (–OC_3H_7) on to the surface was characterized by TG-DTA and FTIR. For IR analysis samples were pelletized with KBr and pressed at 40 kPa (60 s) and next at 80 kPa (30 s). Measurement was approved on single beam FT-IR analyzer NICOLET Impact 400.

Effect of chemisorption of 2-propanol on silanol is appeared at absorption band of the asymmetric stretching mode $\nu_{as}(CH_2)$ a $\nu_{as}(CH_3)$ groups at wavelength 2935 and 2985 cm^{-1}, respectively. Adsorption around 1460 cm^{-1}

indicates bending of δ (CH_3) and δ (CH_2) groups. A broad absorption band in 3400 cm^{-1} region is usually assignable to stretching vibration mode –OH groups in alcohol and water molecules. Very weak band at 3680 cm^{-1} is assigned with chained silanol groups onto silica surface. Presence of water molecule determines bending –OH groups absorption band at 1640 cm^{-1}. Further absorption band in the spectra on Fig. 3. represents common vibration modes SiO_2. At wavelength 471 cm^{-1} and 810, 1106 cm^{-1} was observed bending and stretching modes in tetrahedral $[SiO_4]^{2-}$, respectively.

TG-DTA analysis results (*TG-DTA analyzer SETARAM* 92-18) are shown in Fig. 4. Sample was heated in the air by temperature rate 10 °C min^{-1}. In the course of the heat flow, three peaks correspond with weight decrease on to TG curve. The first decreasing of mass of the sample (about 0.4 %) up to 100 °C is caused by evaporation of residual 2-propanol. The endothermic effect with maximum at 231°C due to desorption of chemisorbed isopropanol from silica surface. With further temperature increase, this effect transfers in exothermic one by the thermal decomposition of isopropoxy groups. Exothermic peak at 390 °C is connected with combustion of residual carbon due to thermal decomposition of ≡Si–OC_3H_8 groups. This processes represents 2.6% decreasing of the sample mass.

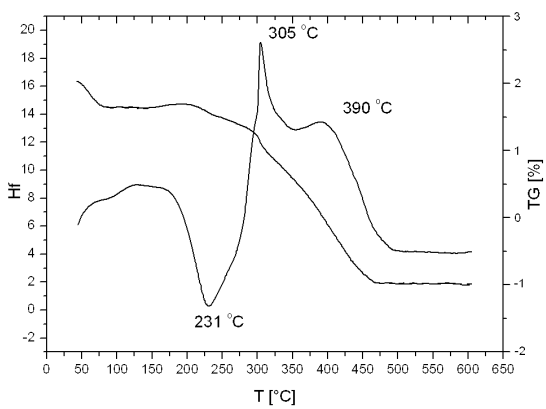

Fig. 3. **TG-DTA of silica modified by chemisorption of C_3H_8O**

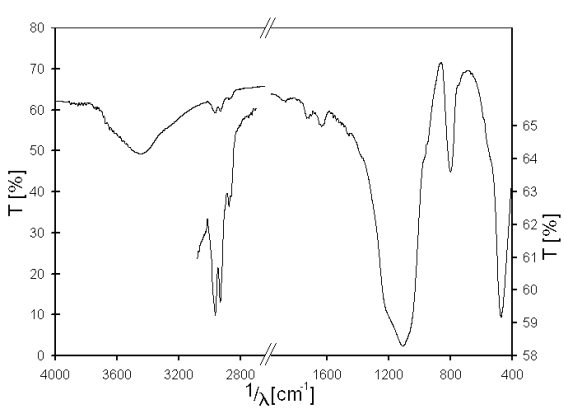

Fig. 4. **FTIR of silica modified by chemisorption of C_3H_8O**

Conclusion

Applied method of azeotropic esterification of the silanol groups enables synthesis of surface 2-propanol ester on colloid silica. This species with surface modified by topochemical reaction (Eq. 1) may keep size close to value of the original SiO_2 particles of Tosil (10 nm) and form relatively stable alcosol, resp. isopropanosol. Presence of isopropoxy groups have been determined by differential thermal analysis, thermogravimetry and IR. Thermal stability of ≡Si–O–C_2H_5 groups has been stable in air up to 200 °C.

This material containing the ≡Si–O–C_2H_5 groups may be hydrolysed in water contained medium. This process leads at first stage to silanol and C_3H_8O molecule (Eq. 2). During condensation of two silanol groups (Eq. 3) or silanol group combined with isopropoxy group (Eq. 4) the siloxane bridge is formed. This behavior allows utilization of this material as precursor for sol-gel synthesis of SiO_2 based oxidic networks.

$$\equiv Si–O–C_2H_5 + H_2O \leftrightarrow \equiv Si–OH + C_3H_8O \quad (2)$$

$$\equiv Si–OH + HO–Si \equiv \leftrightarrow \equiv Si–O–Si\equiv + H_2O \quad (3)$$

$$\equiv Si–O–C_2H_5 + HO–Si \equiv \leftrightarrow \equiv Si–O–Si\equiv + C_3H_8O \quad (4)$$

REFERENCES

1. Jarzycki J.: Journal of Sol-Gel Science Technology *8*, 17 (1977).
2. Primeau N., Vautey C., Langlet M.: Thin Solid Films *310*, 47 (1997).
3. Wenxiu Q., Hu X.: Optical Materials *22*, 31 (2003).
4. Bültzingslöven Ch., McEvoy A. K., McDonagh C., MacCraith B. D.: Analytica Chimica Acta *480*, 275 (2003).
5. Rao A. V., Kulkarni M. M.: Materials Research Bulletin *37*, 1667 (2002).
6. Alié Ch., Pirard J. P.: Journal od Non-Crystalline Solids *320*, 21 (2003).
7. Santos A. M. M., Vasconcelos W. L.: Journal of Non-Crystalline Solids *273*, 145 (2000).
8. Srivastava R., Chandra S.: Solid State Ionics 152–153, 741 (2002).
9. Brinker C. J., Scherer G. W.: *Sol-gel Science: The Physics and Chemistry of Sol-Gel Processing*, Harcourt Brace, San Diego, 1990.
10. Wei Y., Bakthavatchalam R., Whitecar C. K.: Chemistry of Materials *2*, 337 (1990).
11. Chan Ch.-K., Chu I.-M., Ou Ch.-F., Lin Y.-W.: Materials Letters *58*, 2243 (2004).
12. Liu J., Ying P., Xin Q., Li C.: Applied Surface Science *126*, 16 (1988).
13. Jal P. K., Patel S., Mishra B. K.: Talanta *62*, 1005 (2004).
14. Ettlinger M., Ladwig T., Weise A.: Progress in Organic Coatings *40*, 31 (2000).
15. Bauer F. A., Freyer A., Ernst H., Glasel H.-J., Mehnert R.: Applied Surface Science *179*, 119 (2001).

16. Fu X., Qutubuddin S.: Colloids and Surfaces A: Physicochemical & Engineering Aspects *179*, 65 (2001).
17. Krysztafkiewicz A., Jesionowski T., Binkowski S.: Colloids and Surfaces A: Physicochemical & Engineering Aspects *173*, 73 (2000).
18. Zhang J., Gao L.: Ceramics International *27*, 143 (2001).

L16 ANALYSIS OF CERAMIC TILES BY LASER ABLATION-BASED TECHNIQUES

LINDA ZAORÁLKOVÁ, VIKTOR KANICKÝ and ALEŠ HRDLIČKA
Department of Analytical Chemistry, Faculty of Science, Masaryk University in Brno, Kotlářská 2, 611 37 Brno, Czech Republic, liza12@centrum.cz

Introduction

Many routine analytical techniques for determination of chemical composition are employed in technology of ceramics. First used methods for analysis of ceramics were based on sample dissolution and successive solution analysis. Dissolution procedures are based on the acid attack of the sample involving the use of hydrofluoric acid[1]. Unfortunately, digestion of the sample is often incomplete and samples could be contaminated during dissolution[1, 2]. Furthermore, these methods are time-consuming and destructive. Despite of these disadvantages these classical methods are still applied. Although there are plenty of more convenient techniques, digestion still takes important part in analysis of ceramics and in archaeometry as well[3]. Nowadays, methods such as scanning electron microscopy (SEM), X-ray fluorescence spectrometry (XRF), Auger electron spectroscopy (AES), proton induced X-ray emission (PIXE) are used[1, 4]. Beside above-mentioned techniques several techniques using laser can be also employed in field of ceramics analysis.

Laser ablation techniques are based on interaction of laser beam with sample surface. High energy of laser beam is absorbed by surface and converted into heat, resulting in ablation of sample and formation of the vapor in front of the sample when the local temperature reaches the boiling point of the sample material. The vapor with particles of sample is then transported to a second excitation source and analysed.

In case of laser ablation inductively coupled plasma atomic emission spectroscopy (LA-ICP-OES) the vapor is atomized and ionized in ICP and optical emission of excited atoms and ions identifies individual elements. On the other hand, in technique of laser ablation inductively coupled plasma mass spectroscopy (LA-ICP-MS), the ICP is used as ion source[5–7].

The third method called laser induced breakdown spectroscopy (LIBS) is based on scanning of arisen plasma during interaction of the laser beam with sample surface. Emission of the atoms and ions in the plasma is transferred by fibre optics and analysed by a spectrograph[7].

Laser ablation technologies are attractive for little or no sample preparation, non-destructiveness, quickness and low sample consumption. For these advantages laser ablation techniques are widely applied in surface analysis and depth profiling in various fields of science. Especially, laser methods are frequently utilized as a convenient tool by archaeologists and historians[4, 8, 9].

Experimental

Two ablation systems were used for analysis of ceramics. First system was the LINA Spark^{TM} (LSA Sarl, Cully, Switzerland) using the Continuum Surelite Nd:YAG laser operated at the wavelength 1064 nm with a range of energy from 45 to 116 mJ per pulse and pulse duration of 7 ns. The pulse repetition rate was 10 Hz. Pulse energy was adjusted by changing of the flashlamp voltage in the range from 1.10 to 1.29 kV. The defocused laser beam yielded a spot on the sample surface with diameter of 1 mm. The first laser ablation system was coupled with ICP-AES system Vista PRO^{TM} (Varian). The carrier gas flow rate was optimized to 0.85 dm^3 min^{-1}. The ICP-AES system, provided with an echelle spectrometer and CCD detector, was operated in axial viewing mode.

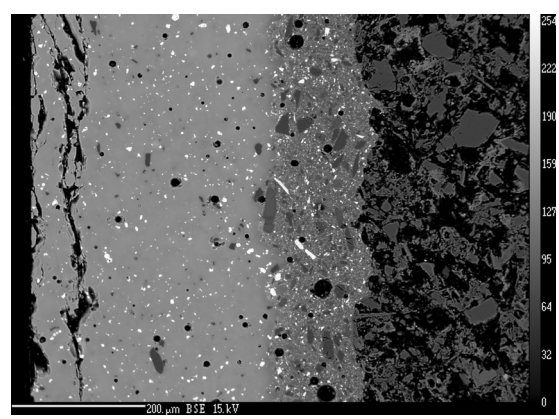

Fig. 1. **SEM photography of tile L600**

Second ablation system was the Geolas Q (Microlas, Germany) based on the ArF* excimer laser with homogenizer (193 nm, Lambda Physik Compex 100). The repetition rate was 10 Hz with energy of 2.5 J $pulse^{-1}$. The diameter of spot size was 31.5 and 16 μm. The ablation system was coupled with ICP-QMS (Agilent 7500). The carrier gas flow rate was 1.80 dm^3 min^{-1} (1.0 He + 0.8 Ar).

The samples used in analysis were ceramic tiles MT100, L101, L600, L965 and L450 (HOB, Lasselberger). Tiles were composed of two or three layers with different composition. Tiles consist of glaze, engobe (engobe was contained only in samples L600 and L965) and ceramic body (Fig. 1.). The chemical composition of each layer of all tiles was determined by X-ray fluorescence spectrometry. Percentages of some of constituents found using XRF spectrometry are given for sample L600 in Table I.

Table I
XRF analysis of sample L600

Compound	Glaze	Engobe Mass percentage [%]	Ceramic body
SiO_2	58.60	57.08	66.11
Al_2O_3	7.98	13.23	18.99
Fe_2O_3	0.27	0.30	1.23
ZrO_2	4.92	15.90	–
ZnO	9.09	3.77	–
PbO	7.85	0.07	–

In case of LA-ICP-OES, laser beam was focused perpendicularly to the tile surface at a fixed single point and the hole with diameter at the surface of 1mm was drilled through layers, while in case of LA-ICP-MS, section of tile was obtained by perpendicular cutting. The tile surface was embedded in a resin and polished surface of this section was line-scanned using the irradiated spot diameter of 31.5 μm over all layers and ceramic body.

Results and discussion

Depth profiles express transition over the layers during ablation, which is represented by increasing or decreasing trend of emission signals of elements present in each layer in various contents (Table I). Laser beam was focused under the surface of sample. Ceramic tiles were studied by LA-ICP-OES at five different laser beam energy values. The intensity of signal rises with increasing laser beam energy as can be seen from Fig. 2. Higher energy of laser pulse results not only in narrower depth profile but also in bold tailing which is undesirable.

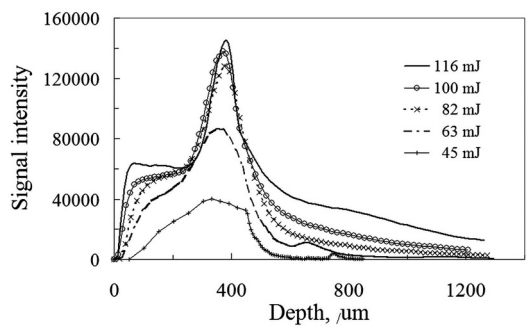

Fig. 2. **Intensity of line Zr 275 nm in relation to depth within the tile**

With both the ablation systems, signals were compensated for fluctuations and changing ablation rate by using the internal standard SiO_2. As the Si content changes slightly between layers, (Table I), corresponding SiO_2 contents were taken into account when applying Si as internal standard. This correction improved the shape of the depth profile, especially at the start and at the end of ablation in deeper part of the crater (Fig. 3.). Decrease of the signal of line Fe 260 nm, caused by lowering of power density of laser beam was particularly compensated for by internal standard (Fig. 3.). Gradual take away of ablated material and deepening of crater results in defocusing of laser beam and consequent changing of the rate of ablation.

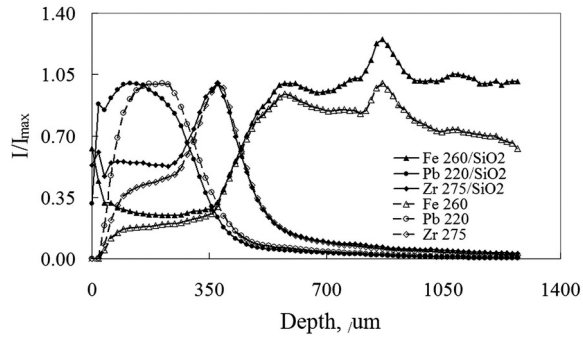

Fig. 3. **LA-ICP-OES depth profile for energy of pulse 82 mJ**

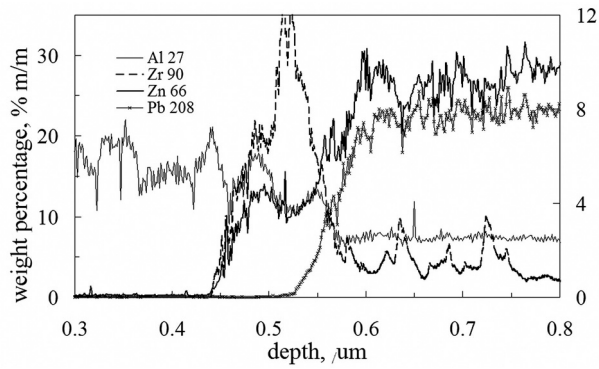

Fig. 4. **LA-ICP-MS depth profile (ceramic body-engobe-glaze from left to right)**

Table II
Ablation rates for each layer

Energy of pulse [mJ]	Glaze [μm pulse^{-1}]	Engobe [μm pulse^{-1}]	Ceramic body [μm pulse^{-1}]
45	2.235	1.274	0.276
63	1.118	0.978	0.664
82	0.840	0.785	0.714
100	0.610	0.494	0.820
116	0.495	0.335	1.149

Rate of ablation is not related only to depth of crater but also to the composition of the layers and energy of laser beam (Table II). The most balanced ablation rates through all layers were for the energy 82 mJ. Depth profiles are smooth and do not exhibit spikes corresponding to mineral grains and other local inhomogeneities, as are, for that matter, visible from

electron microscopy image (Fig. 1.). Smooth course of the depth profile is due to intentionally relatively long integration times used with ICP-AES. This approach makes it possible to obtain "global", averaged depth profiles.

Linear scanning of the tile section performed with LA-ICP-MS is presented in the Fig. 4. Profiles are not as smooth as in case of LA-ICP-OES, because of short MS acquisition times (10–100 ms) that made it possible, together with small laser spot diameter, to record sample fine structure, similarly as electron probe X-ray microanalysis. Individual grains of ZrO_2 were detected in layer of glaze, for example.

Conclusions

The above-presented results demonstrate the possibility of usage of laser ablation techniques in analysis of ceramics. Two different laser ablation plasma spectrometry systems with different spatial and temporal resolution were tested and their possibilities in respect to either global or fine-structure depth profile qualitative analysis were proved. These methods are easy, fast and almost non-destructive without complicated handling procedures. These advantages could lead to broad application of the laser methods not only in ceramic technology but also in more delicate fields as archaeology.

Authors would like to express their thanks to N.Gilon from Laboratoire des Sciences Analytiques at Université Claude Bernard Lyon 1 and D. Günther from Group for Trace Element and Micro Analysis, Laboratory of Inorganic Chemistry, Department of Chemistry and Applied Biosciences, ETH in Zurich.

REFERENCES

1. Šašek L. et al.: *Laboratorní metody v oboru silikátů.SNTL*, Praha 1981.
2. Papadopoulou D. N., Zachariadis G. A., Anthemidis A. N., Tsirliganis N. C.: Stratis J. A.: Anal. Chim. Acta *505*, 173 (2004).
3. Tsolakidou A., Garrigos J. B., Kilikoglou V.: Anal. Chim. Acta *474*, 177 (2002).
4. Melessanaki K., Mateo M., Ferrence S. C., Betancourt P. P., Anglos D.: Appl. Surf. Sci. *197–198*, 156 (2002).
5. Russo R. E., Mao X., Liu H., Gonzalez J., Mao S. S.: Talanta *57*, 425 (2002).
6. Gunther D., Jackson S. E., Longerich H. P.: Spectrochim. Acta B *54*, 381 (1999).
7. Vadillo J. M., Laserna J. J.: Spectrochim. Acta B *59*, 147 (2004).
8. Calao F., Fantoni R., Lazic V., Spizzichino V.: Spectrochim. Acta B *57*, 1219 (2002).
9. Junk S. A.: Nucl. Instr. And Meth. In Phys. Res. B *181*, 723 (2001).

L17 SHUNGITE ROCKS AND THEIR MINERAL PROCESSING

TOMÁŠ SVĚRÁK and PETRA MOUČKOVÁ
Institute of Material Chemistry, Faculty of Chemistry, Brno University of Technology, Purkyňova 118, 612 00 Brno, Czech Republic, sverak@fch.vutbr.cz

Introduction

Shungite is a natural, poly-mineral, carbon containing material which – from the geological point of wiev – belongs to the oldest carbon containing minerals on Earth. This material has a unique structure of uniformly distributed highly disperse crystalline silicate particles in amorphous carbon matrix and due to its atypical properties, relatively rare occurrence and, last but not least, even to a very interesting appearance of dense green to black mineral, it has been under a veil of mystery. Shungite is a solid state organic substance preserved in sedimentary rocks and its name originates from it's best-known deposit nearby the village of Shunga in Karelia. Mysterious properties are ascribed to the mineral – one can encounter it in folk faith healing and it also occurs in occult procedures and formulas. Knowledge of effects of shungite, as it dispersed in east cultures, has been the subject of detailed analysis and scientific testing during the last decades. References can be found to shungite testing in cancer research where it makes a component of anticancer drugs and to its use as drinking water treatment additive having some anticancer effects. There are also references to shungite applications in the branch of colour producing industry and pigment production, shungite is being tested in water treatment branch of industries, in shielding against pathogen zones and radiation, in the electrometallurgy of non-ferrous metals, in the production of phosphorus and in rubber industries[1].

Theoretical part

Shungite rocks

Shungite originated in the process of intense accumulation of organic material in archeozoic Precambrian rocks some 2 billions years ago. Clarification of such an extraordinary intense accumulation of organic material has been disputed until now. The occurrence of shungite deposits represents a result of combination of petrified oil fields, petrified organosilicate diapirs and volcanic rocks. Shungite deposits were formed during volcanic activities in non-euxinic brackish water in the environment of lagoons. Shungite occurs both in dispersed and concentrated form and both in layers of laminar rock and as veins of ore. The general name shungite rock is used for all those rocks, in which the mineral is found in a concentrated form and those rocks are classified into three basic categories (for more information see[2]).

Processing properties

In case of any application of shungite based on a broad scale of it's utility properties, it is necessary to have a knowledge of structure, chemical properties and principal process-

ing properties of this material. Because the material in question will always be applied in a particulate form, and mostly in a very fine or possibly even in a micro fine particular form – its disintegration, classification and bulk properties belong to those characteristics that must be known above all.

Disintegration and classification properties

Of many possibilities that are available for assessment of energy consumption of grinding, the Bond theory and the so called „coefficient of grinding" are most often used in the praxis of assessment of regimes of very fine grinding. The coefficient represents integral energy requirements for the creation of a unit of new surface of the ground material[4].

To assess classification properties, the material constant ε entering the Equation 1 has often been used[5].

$$d_{cr} = \frac{3D \cdot \rho_f \cdot \psi \cdot \varepsilon}{8\rho} \cdot \left[\frac{w_r}{v_u}\right]^2 \quad (1)$$

where:

$$\psi = \frac{21}{Re} + \frac{C}{\sqrt{Re}} + 0.28 \quad (2)$$

d_{cr} – is the critical size of the particle [m]

D – is the effective diameter of the turbine of the classifying device [m]

ρ_f – is the density of the stream of gas [kg m^{-3}]

w_r – is the radial component of the stream of gas that transports particles into the turbine of the classifier [m s^{-1}]

v_u – is the circumferential speed of turbine of the classifier which depends on the effective diameter of the turbine [m s^{-1}]

ψ – is the correction coefficient that includes gas flow

ε – is the correction material constant that includes the influence of surface interaction forces of the classified particles

C – is the shape factor of particles

Re – is the Reynolds number.

Experimental part

Grinding tests were carried out in a 10 litre vibration mill (made by Přerovské strojíry, model 1872). The mill was modified in the PIB Brno to enable its barrel cooling (by means of a mantel) and operation in a controlled atmosphere.

Shungite was ground in a nitrogen atmosphere, in a batch regime and with water cooling circuit employed for mill cooling via the said mantle. Regimes of grinding with and without grinding activator were alternatively chosen. The grinding times of samples without surface active additive were from 2.5 minutes to 32 hours, the grinding times of samples with surface active additive were from 15 minutes to 8 hours. Samples were taken in accordance with a chosen time series. Sample taking lasted 1 minute and 30 seconds.

Mill barrel temperature and characteristics of electrical power consumption were picked-up in the course of grinding. Evaluation and integration of the latter values gave the real grinding energy for this type of milling equipment. The measurement was supplemented by the data of nitrogen consumption from the protective atmosphere of the mill.

Samples were evaluated by measuring their bulk density, by analysing their content of abrasion materials and by applying granulometry methods in two steps: first of all it was a primary screening and then it was a He-Ne laser granulometer LA-500 Horiba (Japan). During grinding, ground materials were visually mapped by scanning in an optical microscope with the assistance of digital camera. Selected samples were pictured by methods of electron microscopy. Samples were concurrently analysed for their structure (X-ray analysis) and selected chemistry.

Classification tests were done in a pilot-plant classifier Alpine ATP-50 (the product of Hosokawa, Alpine, Augsburg (BRD)).

Details of the grinding and classifying equipment and regimes of classification, as well as of the methodology of sample taking and evaluation are available[6].

Results and discussion

Shungite rock analysis

Processed and evaluated sample: the shungite sample supplied by Carbon Gate s.r.o, fraction 3 to 5 mm.

Main components: 26.26 % carbon, 71.59 % aluminosilicates, water 110 °C 0.75 %, water 150 °C 1.4 %.

Basic composition of the alumi-nosilicate components is presented in the following overview. This composition presented corresponds to the chemistry of the raw material before our process testing.

Table I
Chemical composition

Serial no.	Compound	Content [%]	Serial no.	Compound	Content [%]
1.	SiO_2	56.46	13.	P_2O_5	0.05
2.	Al_2O_3	4.05	14.	V	0.015
3.	K_2O	1.23	15.	Ni	0.0085
4.	Fe_2O_3	1.01	16.	Cr	0.0078
5.	S	0.57	17.	B	0.004
6.	MgO	0.56	18.	Cu	0.0037
7.	FeO	0.54	19.	Mo	0.0011
8.	Na_2O	0.36	20.	Sr	0.001
9.	Ba	0.32	21.	Pb	0.0023
10.	TiO_2	0.24	22.	As	0.00025
11.	MnO	0.12	23.	Co	0.00024
12.	CaO	0.12	24.	–	

Further data on the sample. Methods and the results of analysis – see[6].

The results of grinding and classifi-cation tests

The evaluation of first samples brought about some knowledge of shape formation of the resulting ground matter in the course of grinding. The particles exhibit a relatively regular shape of polyhedron or plate like flakes of the small – up to 2.5 – aspect ratio[4]. which. with a sufficient degree of precision. can be considered by one dimension reading d both for the calculation formulas of kinetics of flow during classification and also for the definitions of grinding coefficients for newly resulting surface of the ground matter in the process of grinding. The material exhibits isotropic properties along the directions of fracture surfaces.

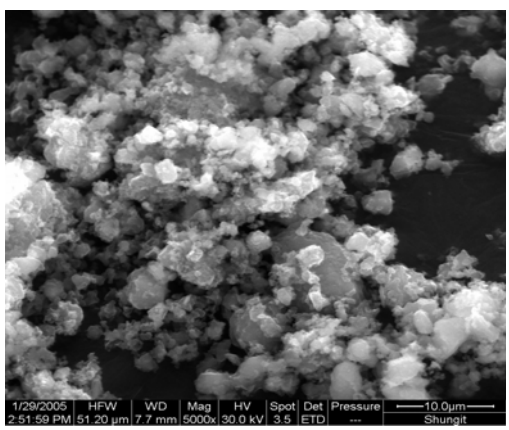

Fig. 1. **SEM picture of shungite particles in the process of grinding**

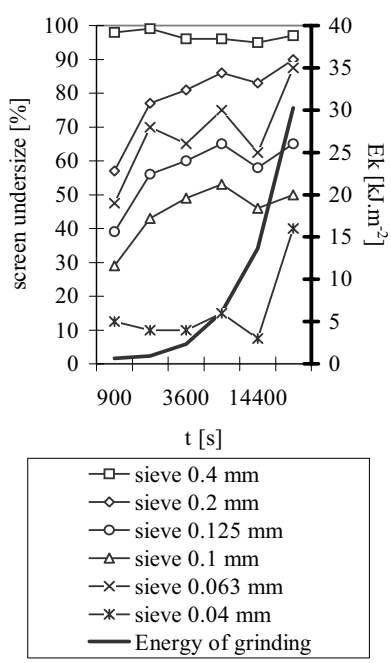

Fig. 2. **Screen undersize and the grinding factor E_k. as a function of grinding time**

Grinding experiments brought about a rich basis of data as for the dependence of grain-saizing of the ground shungite on the time of grinding and on the presence of additives and possibly also about energy requirements for achieving the required grain saizing of the product. The latter data can be compared with calculations based on the formulas of Bond's theory and the grinding factor E_k. From the producer's point overview, probably the most important result appears to be the diagram shown in Fig. 2.

Classification testing comprised, first of all, the tests of assessment of the limits of air classification.

First of all we searched for gas flows that – at given temperature and pressure and at maximum RPM of the turbine equal to $2.4 . 10^4$ [min^{-1}] and regular processing conditions – would satisfy equations (3) and (4) with respect to the minimum grain size of the material. The value of material classification constant ε was retrospectively evaluated for such conditions. The grain-sizing of marginal regular fraction processed on the above classifier is shown in Fig. 3. The calculated value of ε for the fraction d99 is at a very low level of ε = 1.15 (the case of ideal classification conditions is characterised by the value of ε = 1.0). For more details about the conditions of tests[6].

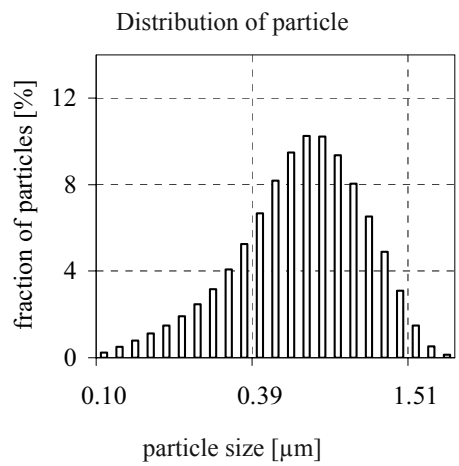

Fig. 3. **Marginal grain sizing of classified shungite**

Grinding and classification properties

In spite of concerns about grinding shungite, it is now obvious that, thanks to a very homogenous distribution of the carbon base in the silicate skeleton, excellent conditions for grinding were created. Shungite is sufficiently strong for common handling, but it crushes easily when normal forces have increased. Simultaneously, due to the presence of long carbon chains in the structure of shungite, there exist ideal conditions for conducting away, in the course of grinding, electrical charges created on fracture surfaces. Therefore the process of grinding up to micron region is very favourable and reagglo-meration tendency of the ground matter is small.

In cases of very fine grinding and micro grinding, supplying grinding additives is understandably needed. With respect to a prevailing quantity of acid silicate surface groups in the structure of shungite, it is above all suitable to use organosilicate binding agents and it is then possible, with these agents, to reach the sub micron region even at „dry" regimes of grinding.

Starting-up with experience on grinding of carbon containing materials, we mostly used a safety protective atmosphere in our test runs. Considering a high content of silicate compounds in the structure of shungite, it is probable that the strict requirement of 100% inert atmosphere could be partially decreased in cases of full scale shungite grinding.

The process of classification, due to continuous conducting away surface electrical charges of shungite particles during processing, is favourable and the material coefficient ε closely approaches its ideal value.

Utility properties of shungite

The basic processing, utility and manu-facturing characteristics of shungite can be discussed from the point of view of our knowledge of the material and also as they appeared in the course of our testing:

– chemistry – besides the carbon part which will be discussed further – the aluminosilicate part consists of a broad spectrum of minerals that can, because of their chemistry, limit applications (it is necessary to check how typical were the samples and how they comply with the strict standards in respective application areas – e. g. the content of heavy metals is on upper limit of acceptance for drugs and food applications, the content of transition bivalent metals excludes any direct application of shungite as a filler in rubber compounds without blocking the negative influence of these metals on stability of such compounds).

– mechanical properties – due to its composite structure in which the silicate part makes a carrier structure for a high content of a rather very pure carbon, shungite is a carbon material having a high strength and abrasion resistance,

– fulerene structures of carbon were not found in shungite,

– chemical stability – the mineral contains no unstable compounds (it is necessary to check for particular application – especially in the case of intended applications in chemical industry and bio-applications, know-ledge of bonds between minerals and carbon chains is also missing),

– electrical conductance – the chains of carbon molecules in the structure of shungite are mostly uninterrupted by silicate compounds (it is necessary to prove by a systematic conductance measurements that would map isotropy and homogeneity of conductance of this material, it would also be appropriate to engage in defining carbon structures and its assumed chains),

– a very active adsorption properties – „shungites are able to increase up to 6-times their inner molecular volume under conditions of extreme adsorption while preserving their outer volume"[1]. Even when considering some uncertainty of the „inner molecular volume" referred to, one can expect high adsorption capability of the material, first of all due to a high content of aluminosilicate compounds evidently encompassing a broad spectrum of minerals that probably offer ample possibilities of bonding to their surface groups (it is necessary to check in interrelation with specific surface or the material which appears to be relatively very small) – a very good miscibility with a majority of materials (due to a rather high relative content of carbon, an easy conduction of electrical charge away of aluminosilicate surfaces can be expected – therefore shungite should behave as a relatively „dull" filler),

– a very good bulk properties – such properties can be expected due to already mentioned passivation mechanisms of surface electric charge and a relatively high bulk densities and low specific surface areas (these properties should be measured for very fine fractions),

– abrasion properties – a higher abrasi-veness can be assumed considering a high content of aluminosilicates (of course, a superposition of very good sliding properties of carbon and abrasive characteristics of silicates is evident; abrasion properties should be checked for those fractions that could be intended for large scale applications, and, naturally an preferably, for the sake of proper choice of grinding and classification equipment for very fine and micro fine fractions).

The other properties of shungite – its often mentioned transcendent properties, its bio-activity, colouring and opacity properties, its utilisation in the industry of pigments or as a filler for rubber compounds, its use as a raw material in metallurgy, for the production of ferrosilicon and in chemical industry…, that all are applications that must be judged by professional workplaces competent in corresponding areas of application.

Conclusions

Natural material shungite finds its applications in the field of water treatment, metallurgy and in pigment production, its utilisation in pharmacy is being tested and rather a broad scale of other application is under consideration. This work presents the results of our first testing of manufacturing properties of shungite, it outlines the possibilities of gaining the required granulometry fractions by grinding and classification processes.

In the chapter „Utility properties of shungite", this work reviews the knowledge of structure and principal processing and utility properties of shungite which knowledge could become a point of reference for those who will engage in application of this very interesting mineral in any realm of life of humane society.

REFERENCES

1. Carbongate s. r. o. www.carbongate.cz.
2. Melezhik V. A., Filippov M. M., Romashkin A. E.: *A giant Palaeoproterozoic deposit of shungite in NW Russia*, Oregeorev, 2003.

3. Medek J.: *Mechanické pochody*, skriptum VUT Brno, 1998.
4. Wills B. A.: *Mineral Processing Technology*, Oxford 1997.
5. Sverak T., Valderrama W. R.: Mineral Processing (in press).
6. Moučková P.: *Shungite rocks*, Diploma thesis, Brno University of Technology, Brno 2005.

L18 MECHANOCHEMICAL FORMATION OF DICALCIUM SILICATE

NADEŽDA ŠTEVULOVÁ,
MAGDALÉNA BÁLINTOVÁ[a], JAROSLAV BRIANČIN and ZUZANA SZEGHYOVÁ[c]
[a]Department of Environmental Engineering, Faculty of Civil Engineering, Technical University of Košice, Vysokoškolská 4, 042 00 Košice, Slovak Republic, nadezda.stevulova@tuke.sk, [b]Institute of Materials Research of the Slovak Academy of Sciences, Watsonova 47, 043 53 Košice, Slovak Republic, briancin@imrnov.saske.sk, [c]Regional Public Health Authority, Ipeľská 1, 042 20 Košice, Slovak Republic, ocha-po@ruvzke.sk

Introduction

Recently there is a growing interest in the syntheses of alternative low-energy cements, chemically and structurally related to Ca_2SiO_4. The total or partial replacement of conventional Portland cement by Ca_2SiO_4 seems to be a good approach to solve both economic and environmental issues in cement industry. Recent published papers have been presented the using fly ashes or residues generated from combustion processes of fuels as raw materials for the Ca_2SiO_4 preparation[1–6] by hydrothermal way. The low temperature syntheses of the new cement kinds based on fly ash (so-called fly ash belite cements – FABC) by hydrothermal process and subsequent heating at temperature of 700 °C[4] was performed. Decrease in the synthesis temperature of inorganic compounds is possible by mechanochemical treatment of the reaction mixtures, especially if at least one component contains water or hydroxyl groups[7]. In previous papers[8, 9], the changes in structure and phase composition of model mixture (SiO_2/$CaCO_3$ and SiO_2/$Ca(OH)_2$) and reactive mixture consisting of fluidised coal fly ash, calcite or portlandite with Ca/Si ratio of 2 and 3 during high-energy milling and subsequent heating were investigated. In this work, the detail characterization of products after mechanochemical treatment of mixture of coal fly ash and portlandite in comparison with starting mixture is studied.

Experimental

As a raw material the Slovak fly ash originating from fluidised bed coal combustion in power plant ENO A in Nováky was used. Table I presents the chemical composition and particle size characteristics of the fly ash. The used fly ash meets the requirements for class F of the European standard.

Table I
Chemical composition, mean particle diameter d_m and specific surface area S_{BET} of coal fly ash

SiO_2	CaO	Al_2O_3	Fe_2O_3 [%]	S_{total}	MgO	l.o.i.*	d_m [μm]	S_{BET} [$m^2.g^{-1}$]
33.0	23.9	11.4	8.3	3.22	1.99	<0.01	29.18	5.0

* loss on ignition

The main crystalline phases detected by XRD are SiO_2 (α-quartz), $CaSO_4$ (Anhydrite), $CaCO_3$ (calcite), $Ca(OH)_2$ (portlandite), CaO (lime), $Al_2O_3.SiO_2$ (kyanite) and clayey minerals - illite and montmorillonite. Fly ash was mixed with $Ca(OH)_2$ prepared by way described in paper[9] at Ca/Si molar ratio of 2. The mixture was milled for 2 h using a planetary mill AGO-2 (URF Technology, Hungary) with acceleration of 80 g. Both the chamber and milling balls were from steel. Both non-milled and 2 h milled mixtures were thermally treated in the high-temperature chamber oven LM 417 (NETZSCH, Germany) for 4 hours at 600–1200 °C. The particle size distribution of powders was measured on granulometer Helos and Rodos (SYMPATEC, Germany) and mean particle diameter was calculated as the first moment of the distribution density. The specific surface area was determined by the standard B.E.T. method using the equipment GEMINI 2360 (Sy-Lab, Austria). A scanning electron microscope (SEM) (Tesla BS-340, Brno) was used to observe the morphology of the powders and the individual particle size. IR study was carried out on FT IR 330 AVATAR (THERMONICOLET, USA) using KBr pellets. X-ray diffraction patterns were recorded on a DRON 2.0 diffractometer with goniometer GUR-5 (Technabsexport, Russia).

Results and discussion

According to Table II, the increase in values of the mean particle diameter and decrease in specific surface area after 2 h milling of mixture comparing to the starting mixture is observed. In accordance with published data in work[10], this fact confirms a formation of agglomerates at high-energy milling under dry conditions. The curves of particle size distribution don't show any significant differences between the milled and starting mixture. For both mixtures, the same value of the distribution density maximum centred at 5–6 μm is reached. A weak increase in peak distribution density attributed to the coarser particles at 70–80 μm indicating a shift to greater particle size in comparison with non-milled mixture is observed. Aggregation of primary particles during mechanical deformation is assumed to be a consequence of cold welding and/or creation of layered structures. SEM images of mixtures before and after mechanochemical treatment are

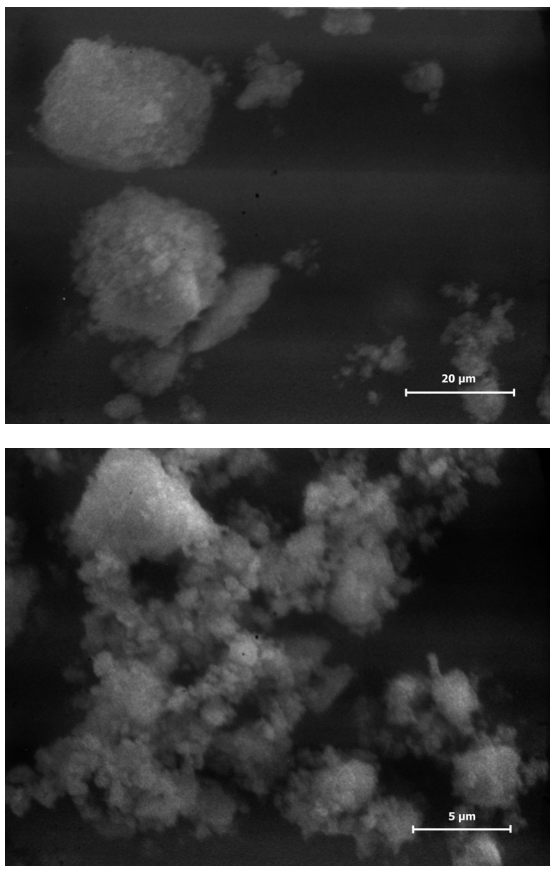

Fig. 1. **SEM images of starting a) and 2 h milled b) mixture of coal fly ash/portlandite**

in accordance with results of particle size analysis and show particles of the various sizes and shape (Fig. 1a) and b)). The different morphology of particles and behaviour of the finest particles at aggregation is illustrated in Fig. 1b).

Table II
Mean particle diameter d_m and specific surface area S_{BET} of coal fly ash/portlandite mixtures before and after milling

Mixture	d_m [μm]	S_{BET} [$m^2 g^{-1}$]
Starting	20.0	10.8
Milled	26.8	3.52

Formation of numerous intimate point contacts and their possible changes to interfaces by plastic flow[11] creates favourable conditions for intimate mixing between the reacting components in mixture on the atomic level. Using XRD analysis, a rapid gradual diminishing and disappearance of the XRD intensity of reflections corresponding to initial crystalline phases of quartz, calcite, portlandite, anhydrite and kyanite was observed after milling for 2 h (Fig. 2.). As it has been shown in paper[8], it relates to the crystallite size

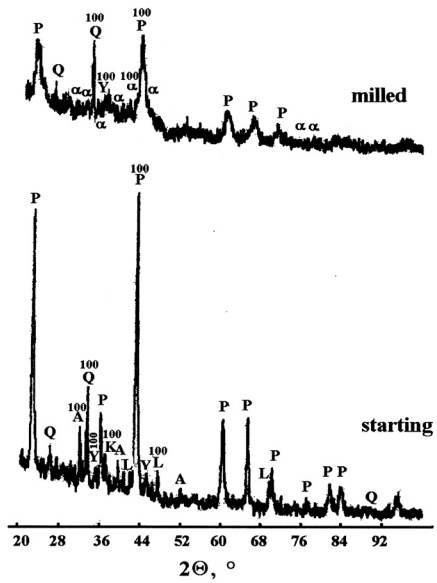

Fig. 2. **XRD patterns of starting and 2 h milled mixture of coal fly ash/portlandite (K-calcite. Q-quartz. Y-kyanite. A-anhydrite. L-lime. P-portlandite. α - bredigite)**

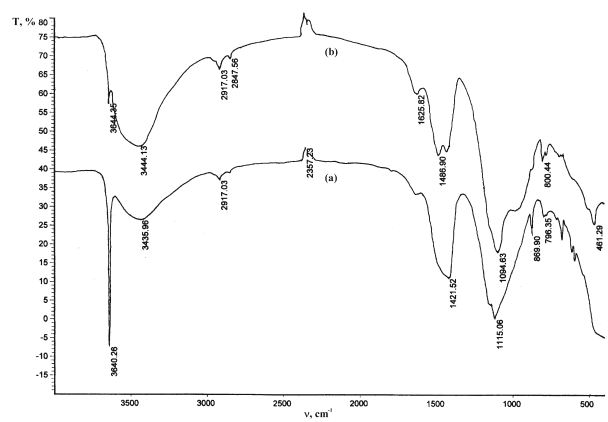

Fig. 3. **IR spectra of starting (a) and 2 h milled (b) mixture of coal fly ash/portlandite**

reduction, introduction of lattice microstrains and/or the amorphization of the reacting components. In the case of calcite and portlandite, the decrease in XRD peak intensity is connected with mechanochemical decomposition of those two substances. A rapid decrease in absorption band intensity around 870 and 3640 cm^{-1} attributed to stretching vibration of OH^- group during milling also confirm mechanochemical dehydration of portlandite (Fig. 3.).

Amorphization of the main reacting silicon and calcium oxide and the formation of tight contacts between particles during high-energy milling greatly facilitate the successive nucleation of new phases. The two new nanocrystalline phases of dicalcium silicates (α-C_2S-bregidite and β-C_2S-larnite) of peak intensity (α100/51, β100/36) were detected apart from residual weak reflections of initial phases

of portlandite, quartz and illite (P100/93, Q100/87, Y100/44) after mechanochemical treatment of mixture (Fig. 2., Table III).

Table III
XRD-intensities of crystalline phase profiles (K-calcite. Q-quartz. A-anhydrite. Y-kyanite. L-lime. α-bredigite (α-C_2S). β-larnite (β-C_2S). G-gehlenite (C_2AS)) in starting and 2 h milled mixtures of coal fly ash/portlandite before and after heating

Mixture	XRD-intensity
Starting	P_{100}/239. Q_{100}/103. A_{100}/73. Y_{100}/43. K_{100}/53. L_{100}/42
After heating	
600 °C	P_{100}/103. Q_{100}/109. A_{100}/84. Y_{100}/69. K_{100}/81. L_{100}/40
800 °C	P_{100}/30. Q_{100}/51. A_{100}/47. L_{100}/129
1000 °C	P_{100}/42. Q_{100}/16. A_{100}/28. L_{100}/13
1200 °C	α_{100}/116.β_{max}/111. G_{100}/137
Milled	P_{100}/93. Q_{100}/87. Y_{100}/44. α_{100}/51. β_{max}/36
After heating	
600 °C	K_{100}/64. Q_{100}/82. α_{100}/45. β_{max}/103
800 °C	Q_{100}/82. α_{100}/47. β_{max}/140. G_{100}/78
1000 °C	Q_{100}/36. α_{100}/91. β_{max}/110. G_{100}/288
1200 °C	α_{100}/90. β_{max}/87. G_{100}/206

Silicates as the main type of compounds on IR spectra (Fig. 3.) show the oxygen related absorption bands in zones of 800–1200 cm^{-1} and 460–470 cm^{-1}. The band around 1100 cm^{-1} is attributed to the symmetric Si–O–Si stretching vibration. The characteristic absorption band of amorphous silica attributed to Si–O symmetric valence vibration of low intensity is observed at 800 cm^{-1} for milled mixture. The broad band centred at 3400 cm^{-1} is responsible for valence vibration of water molecules released during mechanochemical dehydration and their adsorption on surface products. The bands at 1500–1400 with two maxima at 1487 and 1420 cm^{-1}, and 870 cm^{-1} can be attributed to carbonates formed during milling and handling of mixtures. In accordance with the work[4] the formation of hydrated calcium silicates (CSH gel and α-C_2HS) with a very low degree of ordering during mechanochemical reaction between SiO_2 and $Ca(OH)_2$ in mixture can be identified by the absorptions appeared at 1000 and 960–970 cm^{-1}. The presence of CSH gels by XRD it wasn't possible to discover due to their disordered structure.

As it can be seen in Table III, the α- and β-C_2S and C_2AS are the dominant phases at all temperatures during the subsequent thermal treatment of milled mixture. Subsequent heating of milled mixture results in the formation of dicalcium silicates and gehlenite at lower temperature (600 °C) in comparison with the formation of these crystalline phases from starting mixture (1200 °C). Preferential crystallization of β-C_2S was observed in samples of milled mixture during heating at lower temperatures up to 1000 °C. Based on literature data[12, 13] it can be explained by thermal dehydration of α-C_2HS mechanosynthesized intermediary product and its crystallization to β-C_2S.

Conclusion

In this paper the changes in particle size, specific surface area and morphology after 2 h high-energy milling of reactive mixture of fluidised coal fly ash and portlandite (Ca/Si = 2) are shown. The formation of α- and β-C_2S crystalline phases and CSH gels with low degree of ordering was confirmed by XRD and IR spectroscopy. Completed solid-state syntheses of cements related to C_2S in milled mixture takes place at lower temperature comparing to non-milled starting mixture. Mechanochemical synthesis in combination with thermal treatment offers opportunities for the increased utilization of fly ash as a basic raw material for cement production.

The authors are grateful to the Grant Agency of Science (Grant No. 1/0350/03) for financial support of this work.

REFERENCES

1. Jiang W., Roy D. M.: Ceram Bull. *71*, 642 (1992).
2. Chatterjee A. K.: Cem. Concr. Res. *26*, 1213 (1996).
3. Ma W., Brown P. W.: Cem. Concr. Res. *27*, 1237 (1997).
4. Goni S., Guerrero A., Luxán M. P., Macias A.: Chem. Concr. Res. *33*, 1399 (2003).
5. Öztük A., Suyadal R., Oguz H.: Chem. Concr. Res. *30*, 967 (2000).
6. Rodrigues F. A., Monteiro P. I. M.: J. Mater. Sci. Lett.*18*, 1551 (1999).
7. Avvakumov E. G.: Chem. Sustanaible Dev. *2*, 475 (1994).
8. Števulová N., Mezencevová A.: *Materials of the 16th International Congress of Chemical and Process Engineering CHISA 2004. Praha, ECED Praha, 2004*. CD-ROM of Full Texts.
9. Števulová N., Mezencevová A.: Chem. listy *97*, 872 (2003).
10. Tkáčová K.: *Mechanical Activation of Minerals*. Elsevier, Amsterdam 1989.
11. Tkáčová K., Števulová N.: Ceramics-Silikáty *36*, 109 (1992).
12. Goni S., Guerrero A., Luxán M. P., Macias A.: Mater. Res. Bull. *35*, 1333 (2000).
13. Ishida H., Yamazaki S., Sasaki K., Okada Y., Mitsuda T.: J. Am. Cera. Soc. *76*, 1707 (1993).

L19 APPLICATION OF MECHANOCHEMICAL METHODS IN ENVIRONMENTAL ENGINEERING

NADEŽDA ŠTEVULOVÁ[a] and TOMÁŠ SVĚRÁK[b]
[a]*Department of Environmental Engineering, Faculty of Civil Engineering, Technical University of Košice, Vysokoškolská 4, 042 00 Košice, Slovak Republic, nadezda.stevulova@tuke.sk,* [b]*Department of Materials Chemistry, Faculty of Chemistry, Brno University of Technology, Purkyňova 118, 612 00 Brno, Czech Republic, sverak@fch.vutbr.cz*

Introduction

Solid-state mechanochemistry is a field of research dealing with physicochemical transformations and chemical reactions, which occur under the action of mechanical energy. During the 20th century, an extensive accumulation of knowledge in the field of solid-state mechanochemistry was obtained by studying the influence of high-energy milling on the rate and mechanism of mechanochemical solid-state reactions[1, 2]. Numerous papers have been demonstrated an important position of mechanical activation in the intensification and stimulation of the progress of chemical solid-state process engineering[2–4]. In the last three decades, technological and scientific challenges of a search for simple and energy-efficient synthesis and processing route of materials have caused that the non-conventional mechanochemical route became a very useful preparation and processing technique in material science and environmental engineering. It was connected with the preparation of the reactive precursors for special materials and novel, high-performance, and low-cost materials[1, 4] as well as with conversion of various hazardous persistent organic pollutants[5] and organic waste to harmless, defined and usable products[6]. The main advantages, economic and ecological benefits of mechanochemical method are visible in comparison with conventional solid-state reactions: ball milling proceeds at the room temperature, ambient pressure and frequently in a short time, it is environmental friendly technology because no production of wastewaters and harmful emissions to the environment.

Mechanochemical synthesis of alternative inorganic materials from secondary raw materials as well as structural modification of various waste kinds by mechanical treatment is becoming a priority in current mechanochemical research. This paper presents a review of selected results of various feasibility studies demonstrating the application and efficiency of mechanical activation and mechanochemical treatment regarding the utilization of fluidised coal fly ash in concrete and cement production and the defined destruction of hazardous organic pollutants in contaminated materials.

Mechanical activation and mechanochemical treatment in cement processing

Mechanochemical procedures significantly accelerate the solid-state synthesis and high-temperature compacting processes of building materials, they reduce the temperature of these processes simultaneously with the enhancement of product quality[2]. Current research in the area of mechanical activation of cement is directed towards improvement in the mineral composition, hydration and durability of cements minerals[7, 8] and maximization of waste materials as additives in the cement such as fly ash and blast furnace slag[9–11]. However, fly ash and blast furnace slag usage in blended cements is restricted by hydraulic activity of these materials. Mechanical activation offers opportunities for their increased utilization in cement industry and for the development of waste-free technologies. There have been some interesting recent studies concerning mechanical activation of ashes from coal-fired power plants and their use in clinker production of the cement industry and concrete production[10–12]. The investigation of the use of mechanically activated fly ash as a partial cement replacement in concrete showed that the addition of the activated coal fly ash improves the compressive strength of the concrete/mortars[13–15]. In paper[14] was studied the influence of mechanical activation of fluidized coal fly ash with addition of various surfactants on its pozzolanic activity. The highest compressive strength values of hardened fly ash based concrete (25 % cement replacement) after 28- and 90- days curing time were obtained for the cement/fly ash composite containing the finest fly ash prepared by mechanical activation of coal fly ash for 1.5 h with 0.2% triethanolamine in vibratory mill. The value of relative compressive strength of this concrete sample exceeded the values required by STN EN 450, i. e. $K_R > 75$ % after 28 days or $K_R > 85$ % after 90 days. This result is in accordance with data from literature[16, 17] according to the particle size, specific surface area and activity of surface of fly ash particles play a significant role at the hardening of cement/fly ash pastes.

Utilization of fly ash in cement production is based on the development of new kinds of cements using appropriate methods. Fly ash based cements were prepared by mechanical activation of mixture consisting of Portland cement with 20 % fly ash in a vibratory mill with rings for three minutes resulted in 58% increase in the compressive strength after 28 days of hardening[11]. Another studies on fly ash based cements have indicated that combined effect of mechanical and chemical activation results in much higher strength than chemical or mechanical activation carried out separately[18, 19].

The study of mechanochemical changes proceeding during high-energy ball milling of fluidized coal fly ash was carried out with the aim of coal fly ash utilization as a basic raw material in the cement production. Results of high-energy milling of coal fly ash as a poly-component mixture of solids (consisting mainly of SiO_2, CaO, Al_2O_3 and Fe_2O_3) with Ca/Si ratio of 0.69 presented in paper[20] have shown that mechanochemical synthesis proceeds in the ball mill between the main components SiO_2 and CaO finding in fly ash and an amorphous and/or nanocrystalline calcium silicate (CS) is formed. Formation of cement minerals C_2S and C_3S was investigated at high-energy milling of reactive mixtures consisting of coal fly ash and calcium compound

addition (calcite and portlandite) at Ca/Si ratio of 2 and 3 (ref.[21,22]). Planetary milling under conditions of high intensity of cyclic loading (an acceleration exceeding 80 times the gravitational one) of these mixtures results in transition of reacting components into mechanically induced metastable states of various kind and lifetime. Mixing of the reacting components at a physical level during milling leads to an increase of the number of contact spots between reacting particles. An activity of new-formed surfaces during milling accompanied by a change in the energetic state of structure in the surface layers of particles and the tendency of ultra-fine particles to agglomeration constitute a morphological metastability. An increase of the number close contacts between particles, area of forming interfaces, concentration and mobility dislocations in a thick network of interfaces and grain boundaries as well as temperature elevation at the contact points (hot spots) during energy-intensive milling of reactive mixtures accelerate a self diffusion. This effect known in mechanochemistry as the "transport effect" leads to mixing of reacting components at the chemical level and it brings about a partial mechanochemical conversion to calcium silicates. The new nanocrystalline phases of dicalcium silicates (α-C_2S-bregidite and β-C_2S-larnite) and aluminosilicate (C_2AS-gehlenite) are formed in both reactive mixtures with Ca/Si = 2 at milling for 2 and 8 h. The C_2S-formation proceeds faster in the mixture with portlandite because of the water and OH^- ions formed during mechanochemical dehydroxylation of $Ca(OH)_2$ in mixture and it occurs under conditions similar to hydrothermal reaction. In case of high-energy milling of mixtures with Ca/Si = 3, a formation of high metastable X-ray amorphous precursors of C_2S and C_3S was observed. Completion of solid-state synthesis of cement minerals in mixtures of coal fly ash with calcite or portlandite milled for 2 h with Ca/Si of 2 and 3 takes place during subsequent heating at lower temperatures about 200 to 400 °C in dependence on metastability degree and Ca/Si ratio in mixture[21,22].

Mechanochemical degradation of wastes and pollutants

The persistence of hazardous pollutants in the environment or waste streams and materials is frequently due to the thermodynamic and/or kinetic stability related to their molecular structure. Further these pollutants tend to be sorbed strongly to other components of the contaminated matter. Published literature data refer that these difficulties of stability and inaccessibility can be effectively overcome by mechanochemical methods[5,23]. Hazardous persistent organic compounds were completely dechlorinated by ball milling of the contaminated material with a base metal and a hydrogen donor. This novel ex situ dehalogenation approach can be successfully applied both to contaminated and highly concentrated materials or their mixtures. Mechanochemical processing of plant raw materials with special solid reagents results into forms with practically useful properties[6]. High-reactive mechanocomposite was prepared from cellulose component and bioactive alkaloids and triterpenic acids were transformed into the form more soluble substances.

Conclusion

Some specific features of the mechanochemical treatment of coal fly ash and hazardous organic pollutants with aim of their re-use in industry were summarized. Utilization of wastes is not only beneficial from the point of view of resource conservation, energy saving and CO_2 emissions decrease but also solves problems associated with disposal of the wastes.

The authors are grateful to the Grant Agency of Science (Grant No. 1/0350/03) for financial support of this work.

REFERENCES

1. Boldyrev V. V., Tkáčová K.: J. Mater. Synth. Process. *8*, 121 (2000).
2. Tkáčová K.: *Mechanical Activation of Minerals*. Elsevier, Amsterdam 1989.
3. Morales J., Tirado L.: Thermochim. Acta *110*, 319 (1987).
4. Suryanarayana C., Ivanov E., Boldyrev V. V.: Mater. Sci. Eng. *A304–306*, 151 (2001).
5. Tanaka Y., Zhang Q., Saito F.: J. Mater. Sci. *39*, 5497 (2004).
6. Lomovsky G. I.: *IVth International Conference on Mechanochemistry and Mechanical Alloying – INCOME 2003, Braunschweig, 8–11 Sept. 2003*, Book of Abstracts, O-66.
7. Juhasz A. Z., Opoczky L.: *Mechanical Activation of Minerals by Grinding: Pulverizing and Morphology of Particles*. Ellis Horwood Limited, New York, 1994.
8. Boldyrev V. V.: J. Chim. Phys. *83*, 821 (1986).
9. Sekulič Z., Popov S., Miloševič S.: Ceramics-Silikáty *42*, 25 (1998).
10. Sekulič Z., Popov S., Duričič M., Rosič A.: Materials Letters *39*, 115 (1999).
11. Johansson K., Larsson C., Autzutkin O. N., Forsling W., Rao H. K., Ronin V.: Cem. Concr. Res. *29*, 1575 (1999).
12. Paya J., Monzo J., Borrachero M. V., Mora E. P., Amahjour F.: Cem. Concr. Res. *30*, 543 (2000).
13. Števulová N., Svěrák T.: Inžinierske stavby *51*, 36 (2003).
14. Števulová N., Mezencevová A.: *Proceedings of 6th Conference on Environment and Mineral Processing. Ostrava, 2002* (Fečko P., ed.), part I, p. 133. VŠB TU Ostrava, 2002.
15. Paya J., Monzo J., Borrachero M. V., Mora E. P., Lopez E. G.: Cem. Concr. Res. *26*, 225 (1996).
16. Berdov G. I., Balachnin M. W., Protalinski A. N: Izv. Sib. Otdel. AN SSSR, ser. chim. nauk 1983, 45.
17. Wang A., Zhang Ch., Sun W.: Cem. Concr. Res. *33*, 2023 (2003).
18. Shi C., Day R. I.: Cem. Concr. Res. *31*, 813 (2001).
19. Qian I., Shi C., Zhi W.: Cem. Concr. Res. *31*, 1121 (2001).

20. Števulová N., Mezencevová A.: Chem. listy *96*, 515 (2002).
21. Števulová N., Mezencevová A.: Szesyty Naukowe Politechniki Rzesowskiej, Budownictwo i inżynieria środowiska, part 2 – Environmental Engineerging *37*, 407 (2004).
22. Števulová N., *Mezencevová A.: Materials of the 16th International Congress of Chemical and Process Engineering CHISA 2004. Praha*, ECED Praha, 2004. CD-ROM of Full Texts.
23. Birke V., Mattik J., Runne D.: J. Mat. Sci. *39*, 5111 (2004).

L20 CALCIUM HYDRATE SORPTION PROPERTIES

TOMÁŠ SVĚRÁK[a], ROMANA MOUČKOVÁ[a] and V. OBŠEL[b]
[a]*Institute of Material Chemistry, Faculty of Chemistry, Brno University of Technology, Purkyňova 118, 612 00 Brno, Czech Republic, sverak@fch.vutbr.cz,* [b]*UTÚO, Veslařská 230, 637 00 Brno, Czech Republic, obsel@atlas.cz*

Introduction

Calcium hydrate is used in building industry but, presently, it comes more and more in useful in other branches of industry, especially when applied for sorption purposes[1]. In our previous papers[2,3], we already devoted attention to mapping those characteristics of calcium hydrates that are used for assessment during processing of this material primarily intended for building purposes and that could have an impact on the sorption properties of such a material. It was obvious that problems of sorption properties are so complex that parameters enabling to assess sorption properties of calcium hydrate prior to its particular application are nowadays not available. Series of tests carried out predominantly in full scale testing of de-sulphurisation has shown that sorption surface of calcium hydrate can be a long way from a parameter decisive for achieving higher sorption effects. Therefore we concentrated our interest to collecting maximum information about changes of surface characteristics of a few different types of hydrates that would help to define the mechanisms of sorption. In this paper we devote attention to links among detailed chemical analysis of the hydrate, it's structure and it's sorption behaviour. We assessed the structure of calcium hydrate according to imaging snapshots of hydrate surfaces taken by the methods of AFM and electron scanning microscopy. At the same time, we assessed sorption properties of calcium hydrates according to experimental data of specific surface as measured by gas absorption method BET and by parallel data of sorption capacity as they resulted from the newly outlined experiments of SO_2 sorption. By taking the advantage of comparative material, the potentialities of the above specified testing were delineated in this paper.

Theoretical part

Calcium hydrate

Calcium hydrate is defined as a material originating by the hydration of CaO produced by a so called dry process. It means that CaO is hydrated by only such a quantity of water that corresponds to stoichiometry plus a slight surplus that nearly totally evaporates at temperatures above 100 °C. The hydration proceeds according to the equation:

$$CaO + H_2O \rightarrow Ca(OH)_2 \quad \left(+1180\,kJ.kg^{-1}\,CaO\right) \qquad (1)$$

However, it is necessary to realise that calcium hydrate is not the same substance as calcium hydroxide. Calcium hydrate, besides non-hydrated CaO the content of which is often over 15 %, also contains certain „under-fires" representing the residues of carbonates after the first stage of processing of a limestone raw material via thermal decomposition of a natural limestone at temperatures over 800 °C, which decomposition – under the release of carbon dioxide[4] – proceeds according to the equation:

$$CaCO_3 \rightarrow CaO + CO_2 \qquad (2)$$

The residues of carbonates that were not decomposed by the above reaction are usually found in the amounts of a units of percent. The hydrate usually also contains, in analogous amounts of a units of percent, foreign matter originating from accompanying materials that attend the raw material in its deposits.

Calcium hydrate, as a resultant product of two chemical reaction processes presented above, is a very porous particulate matter occurring, first of all, in two principal crystalline forms[1].

Approximately l' of the volume of material is in the form of hexagonal platelets or tiny prisms of calcium hydroxide whose fissibility copy its crystal lattice. The granulometry interval of calcium hydrate starts with the basic elements composed of „cauliflower" clusters of crystals formed predominantly along the lattice of calcium hydroxide and having the size of tens of nanometers and the interval ends at units of millimetres. The said granulometry interval thus goes across the span of more than six orders of magnitude of sizes.

The description of methods used

In this work we mention only the AFM microscopy, the scanning electron microscopy and the measurement of sorption properties of calcium hydrates.

Microscopy based on the detection of atomic forces

Microscopy AFM (Atomic Force Microscopy) investigates surfaces of samples on the basis of mutual force interactions among atoms being on the tip of a very sharply pointed probe and those on the surface of the sample under investigation.

Details of the grinding and classifying equipment and regimes of classification, as well as of the methodology of sample taking and evaluation are available[6].

The principle of atomic force microscopy relies on the measurement of forces acting between the probe spike and the sample. The sharp spike is placed on a flexible tiny arm having a very low stiffness (≈1 N) which is known as *cantilever* in technical Anglo-Saxon literature. The cantilever must have a very low stiffness so that it would be able to respond to the influence of both attractive and repulsive forces and in a sense it becomes the principal element in the chain of atomic force registration[5]. The principle of function of the microscope is on Fig. 1. Laser beam comes to an adjustable mirror and is focused on the end of the cantilever. From there it is reflected to a quadrant photo detector which – depending on a change of the position of the beam impacting on it – detects the change of deflexion of cantilever.

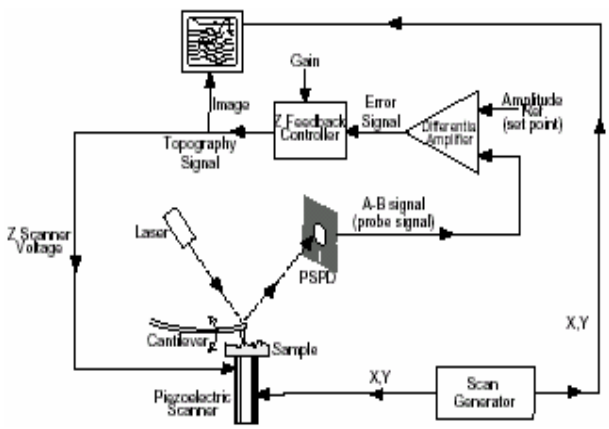

Fig. 1. **Technical outfit and the detection od signal in AFM microscope**

Scanning electron microscope

The image obtained from scanning electron microscope is created point to point in the form of a raster. Electrons emitted by an electron gun are accelerated by high voltage and are focused into a very narrow beam by a multi-lens system.

The focused beam is diverted by means of diverting coils in such a way that it travels, row by row, along the sample surface. Electrons emitted of sample surface at the point of the beam impact are captured and amplified to give electrical signal. This signal then modifies the intensity of another beam of electrons impacting a cathode-ray tube screen. The resulting picture is called raster[6].

The determination of sorption characteristics

Reactivity of calcium hydrates was determined by means of sulphur dioxide in a dynamic system. This method is used for studying the efficiency of sulphur dioxide adsorption in the case of it's passing through a homogenous layer of calcium hydrate.

The principle of the newly outlined test is as follows[7]:

A weighed quantity of powder calcium hydrate is placed on a sintered glass plate fussed in a glass tube in such a way that a defined layer is formed on the plate. The layer is homogenised and subsequently leveled by slightly knocking the tube against a solid base. The gas mixture of a known concentration of sulphur dioxide is sucked through the layer at constant flowrate and at laboratory temperature and pressure. Sulphur dioxide gradually reacts with calcium hydrate according to the equation:

$$Ca(OH)_2 + SO_2 = CaSO_3 + H_2O \qquad (3)$$

The gas mixture exiting the layer bubbles through distilled water whose electrical conductivity is measured. The first breakthrough of non-reacted sulphur dioxide is characterised by a steep increase of the said conductivity of water. The result of this measurement is a typical breakthrough curve.

Experimental part

Calcium hydrate

The material assessed in this work was calcium hydrate of common commercial quality as supplied by European producers to our market (Carmeuse, Lhoist etc.), for more information see [9].

AFM microscopy

Surface topology of the two calcium hydrates denoted as Z 188/5 a Z 189/5 was examined. Contact mode of AFM microscopy with a regime of constant force was used in our measurements. Samples were measured repeatedly in specified time intervals and the influence of ageing of hydrate surface topology was followed. We gained 2D and 3D microphotographs of those calcium hydrates. The comparison of surface structure and its development of the two hydrates which were diametrically different in their application, as enabled within the capabilities of AFM 3D microphotography, is shown in the following sequences presented in Fig. 2. to 5.

The capability of AFM microphotography for 2D imaging is shown by a pair of snapshots presented in Fig. 6. and 7.

Scanning electron microscopy

Surface topology of the same samples Z 188/5 a Z 189/5 which it was obtained by SEM imaging at magnification level 20 000 is shown in Fig. 8. and 9.

The reactivity of calcium hydrates

The reactivity of calcium hydrates was evaluated on the basis of the amount of reacted SO_2. Actually, we measured an extensive package of samples, but to make our presentation more transparent, only the samples corresponding to the preceding demonstrations of results obtained from AFM and SEM are presented in this paper. In fact, we take into a consideration the samples denoted Z 188/5 a Z 189/5. The examples in Fig. 10. and 11. show the influence of sample ageing on the reactivity of hydrates. For the purpose of clearness of representation of calcium hydrate reactivity by means of its breakthrough curve, illustration of behaviour of other materials were also included.

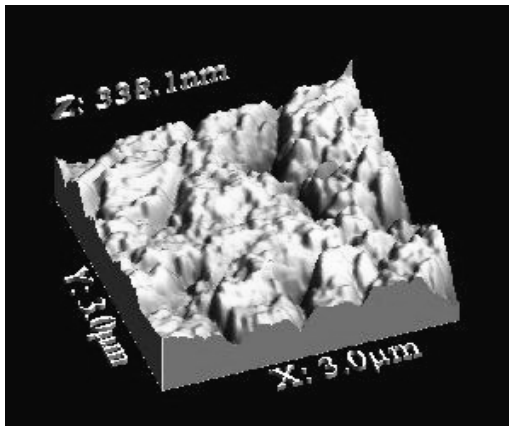

Fig. 2. **AFM – Z 188/5 – sample is 0 days old**

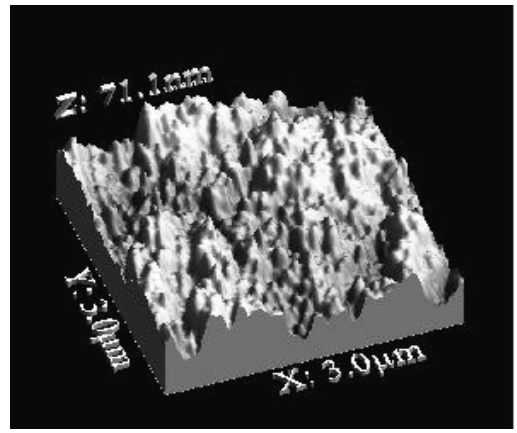

Fig. 3. **AFM – Z 188/5 – sample is 61 days old**

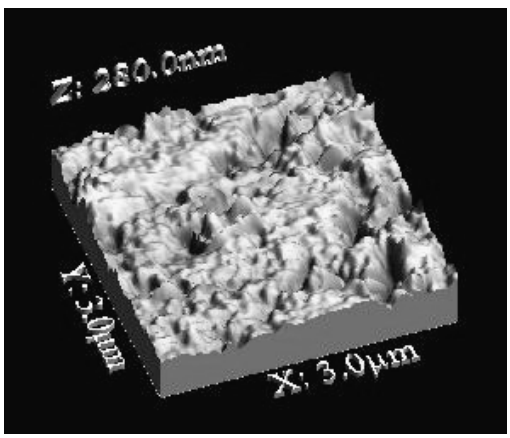

Fig. 4. **AFM – Z 189/5 – sample is 0 days old**

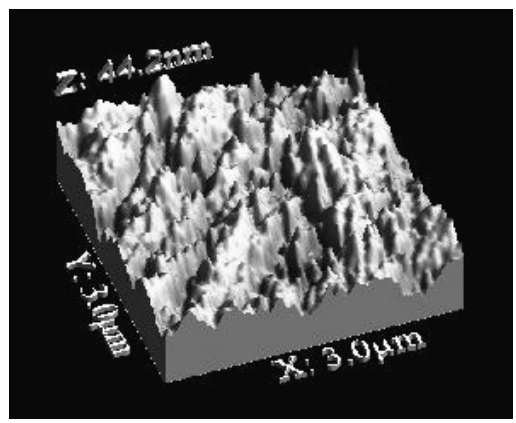

Fig. 5. **AFM – Z 189/5 – sample is 61 days old**

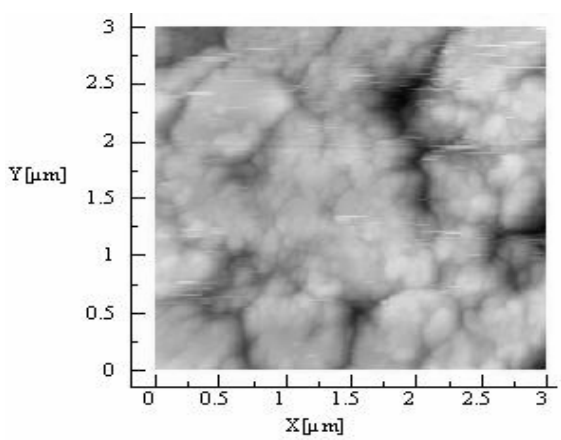

Fig. 6. **AFM 2D, Z 188/5 – sample is 0 days**

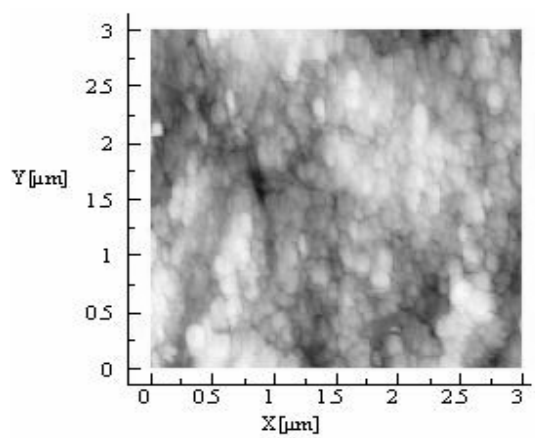

Fig. 7. **AFM 2D, Z 188/5 – sample is 61 days**

Discussion and Conclusion

The results of our work on surfaces-imagery by the methods of AFM and electron scanning microscopy that were chosen to study the absorption of considerably different calcium hydrates were presented in this paper. The results of the above-mentioned surfaces-imagery offered the possibility of their confrontation to our experimental data of sorption capacity, which are based on the newly outlined sulphur dioxide sorption experiments. As became obvious, there are rather considerable differences among all used methods. On

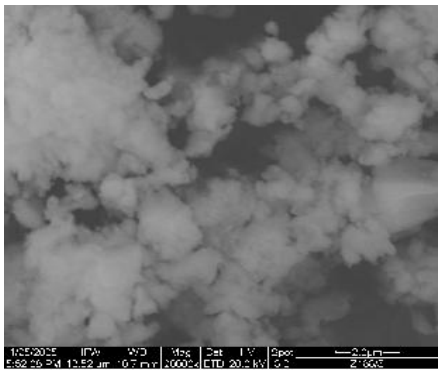

Fig. 8. **SEM, Z 188/5 sample**

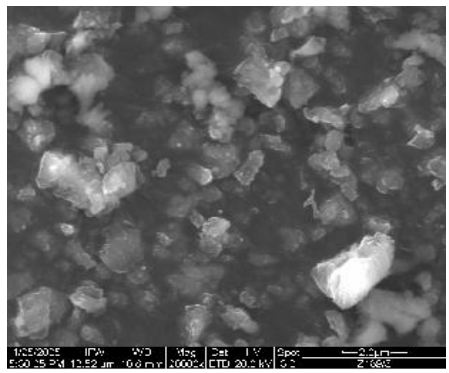

Fig. 9. **SEM, Z 189/5 sample**

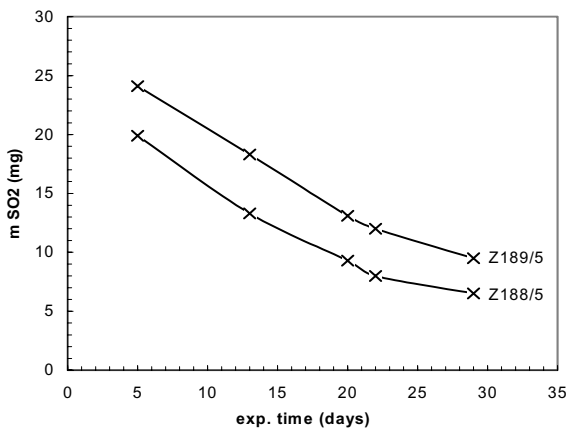

Fig. 10. **Exposition time influence on the SO_2 reaction quality Z 188/5 and 189/5 samples**

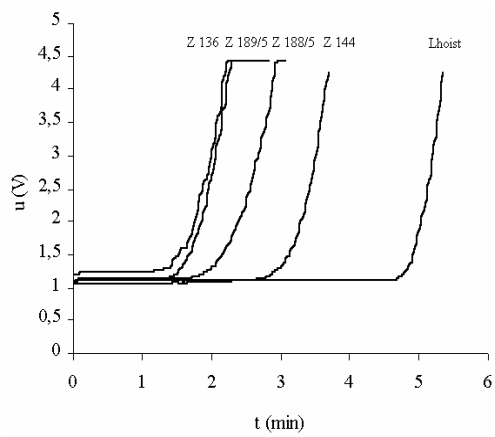

Fig. 11. **Penetration of SO_2 through the $Ca(OH)_2$ layer, samples Z 188/5, 189/5, Z 136, Z 144 and Lhoist**

the other hand, it gives a possibility to express one's opinion about the sorption reactivity of individual materials including a possibility to specify this reactivity explicitly and, retrospectively, to seek out the co-relations to surface structure changes of the hydrates involved. Nowadays, it is too early to make a definite conclusions as for the methodology of our experimental work. However, it is sure that the chosen approach brings the coveted quantification of calcium hydrate sorption behaviour which, owing to its affinity to hydrate performance in de-sulphurisation processes, could bring about more credible data of sorption capacity of hydrates than the results obtained by a quantification of data on nitrogen sorption by the BET method.

If proven by systematic long time tests, that the chosen methodology of assessment of calcium hydrate sorption properties by the test of reactivity with sulphur dioxide correlates with the mesured results of de-sulphurisation, preferably under realistic conditions of plant tests, the chosen surfaces-imagery technique described in this work, could be a door-opener to process changes in the area of technology of calcium hydrates for all development workers. The said process changes will lead then to the desirable and maximally efficient surface structure modifications.

REFERENCES

1. Sverak T.: International Journal of Mineral Processing, *74*, Supplement 1, S379 (2004).
2. Svěrák T., Gachová L. and Malysz K.: Chem. Listy, Symposia, *96*, S218 (2002).
3. Svěrák T., Wichterle K. and Gachová L.: Chemické listy, *97*, S802 (2003).
4. Boyton R. S.: *Chemistry and technology of lime and limestone*, 2nd ed. New York: John Wiley & Sons, 1966, p. 303.
5. Škoda D.: *Vývoj a testování UHV-kompatibilního mikroskopu AFM/STM (Czech)*, Diploma thesis, Brno University of Technology, Brno 2003.
6. Firm www pages Micromeritics [online]. [cit.2005-05-04] http://www.micromeritics.com/products/mercury--porosimetry.aspx.
7. Fiedier R.: *Metody analýzy a kontroly materiálů*, SNTL, Praha 1983.
8. Obšel V.: in preparation.
9. Moučková R.: *Surface structure of calcium hydrate* (Czech), Diploma thesis, Brno University of Technology, Brno 2005.

L21 THE SURFACE CHANGES DETERMINATION OF MECHANICAL ACTIVATED SILICON

MAGDALÉNA BÁLINTOVÁ
and NADEŽDA ŠTEVULOVÁ
Department of Environmental Engineering, Faculty of Civil Engineering, Technical University of Košice, Vysokoškolská 4, 042 00 Košice, Slovak Republic,
magdalena.balintova@tuke.sk

Introduction

Silicon, the most important material in electronics, is one of the most frequenly studied substances in solid-state physics and chemistry. The preparation of silicon-based alloys, composites and ceramics by mechanochemical procedures stimulates the investigation in surface reactivity of finely ground silicon. Milling and handling of finely dispersed powders in vacuum or non-polar liquids belong to the effective methods of surface protection. In attempt to determine the optimal conditions of milling and surface protection of silicon powder against oxidation, the changes in particle size, surface properties and composition brought about by an energy-intensive milling of silicon in various permittivity liquids have been investigated[1]. The nature of milling environment also affects the composition of the superficial oxide layer. Based on received results our further research has aimed at completing our knowledge about surface changes of silicon in consequence of mechanochemical reactions among milling powder, milling media and liquid environment.

In this work identification of the surface changes of silicon during milling in various liquid environments by various analytical methods is presented.

Experimental

The experimental studies were carried out on synthetic silicon of 99.95% purity (Tesla Sezam, Rožnov). The milling was carried out in a planetary mill Pulverisette 4 (Fritsch, Idar-Oberstein) using tungsten carbide chambers and balls of 17,4 GPa hardness under conditions displayed in the Table I. Milling experiments were performed in various liquid environments (water, methanol, benzene, acetone). The particle size distribution and mean particle diameter d_m of milled powders was measured by the method of laser radiation scattering on the Helos and Rodos granulometer (Sympatec GmbH, Claustahl-Zellerfeld).

The specific surface area S_A was determined by the standard BET method using the apparatus Gemini 2360 (Sy-Lab, Vienna).

Infrared absorption spectra were measured by means of a conventional KBr disk method using a FT-IR spectrometer (Bio Lad, FTS 65, Tokyo). Tungsten content of milled samples was determined by method AAS (SpectrAA-30, Varian, Australia).

Table I
Experimental milling conditions

Milling conditions	Planetary milling
Specific mill power P [W kg^{-1}]	209–268
Relative acceleration b	12.9 g
Rate of stress [m s^{-1}]	2.1
Media filling	0.25
Ball to powder weight ratio	20:1
Milling time [h]	0.25–4
Milling environment	water, methanol, acetone, benzene

Results and discussion

Influence of milling enviroment on surface changes of silicon

The area of newly created surface and the particle size distribution provide basic information on milling. Based on previous research works[3–5] and the study of correlation mean particle diameter d_m versus specific energy consumption E (Fig. 1.) and specific surface area S_A versus mean particle diameter d_m for silicon milled in various liquid environments (Fig. 2.) anomalous behavior of silicon milled in water environment was observed. According to literature data this fact was attributed to oxide formation of surface layer on milled silicon particles caused by their mechanochemical reaction with environment.

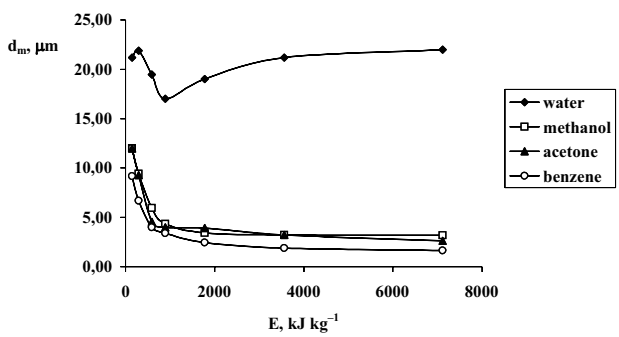

Fig. 1. **Mean particle diameter d_m versus specific energy consumption E for silicon milled in various liquid environments**

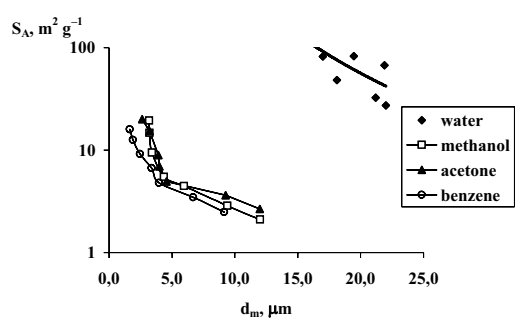

Fig. 2. **Specific surface area S_A versus mean particle diameter d_m for silicon milled in various liquid environments**

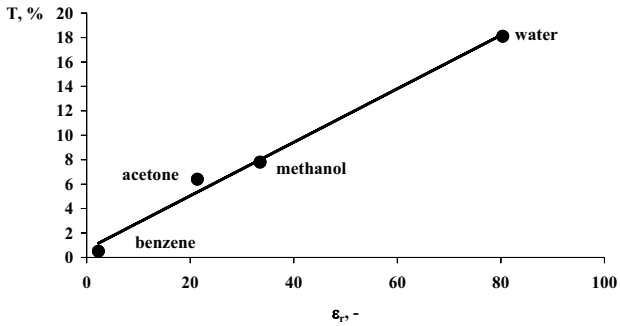

Fig. 3. **Intensity of IR peak around 1100 cm^{-1} *T* for silicon milled versus permittivity ε_r of the used liquid**

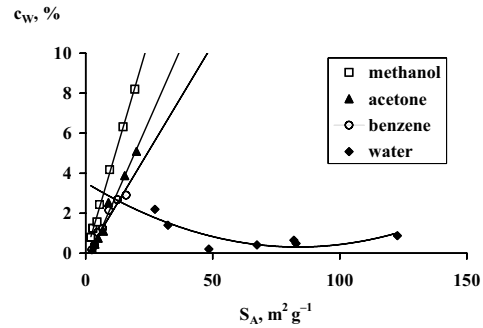

Fig. 5. **Tungsten contamination c_w of silicon versus specific surface area S_A**

In agreement with our previous work[4] the various polarity of milling environment influences oxidation during milling. It confirms the increasing of absorption band intensity around 1100 cm^{-1}, attributed to asymmetric stretching vibration (Fig. 3.) for silicon milled 4 h in various environments.

The results of the IR measurements are in a good agreement with the XPS spectra in our previous published work[4] where formation of suboxides in all organic environments was observed but XPS spectra of silicon milled in water confirmed only line belonging to Si^{4+} in SiO_2. The thickness of the oxide layer formed on the surface of particles milled in water was higher than the sampling depth of the XPS method SiO_2, which is ~3 λ where is the Si(2p) electron mean free path (λ=2.7 nm). The Si^{ox}/Si^0 intensity ratio is proportional to the effective thickness of the oxide layer and increases in the sequence: benzene (0.22) < acetone (0.37) < methanol (0.45) <<water (1).

Influence of milling tools on surface changes of silicon

The result of energy and material interactions between the milling media and milling environment is a contamination of milled materials originated from wear.

The total mill wear expressed as the tungsten contamination c_w of the milled silicon was determined for various environments (water, methanol, acetone and benzene) at various specific energy consumptions *E*. As is seen in Fig. 4. contamination of the milled powder c_w is influenced by the specific milling energy consumption and increased in the sequence: benzene < acetone < methanol.

The same trend can be observed in Fig. 5. where the tungsten contamination c_w is directly proportional to the newly created surfaces S_A for milling in organic liquids. Because of abovementioned anomalous behaviour of silicon milled in water environment our attention was paid only to the influence of organic compound on contamination of silicon by wear.

The study of mechanochemical reactions among the milling balls, environment and silicon was realised by IR spectra. The formation of tungsten compounds can be confirmed by the comparison of IR spectra nonactivated samples, silicon milled in water environment during 4 hour with the spectrum of standard amorphous silica (Fig. 6.). Based on literary date[10] the new band ~833 cm^{-1} in activated sample of silicon was assigned is to the Si–O–Me bond.

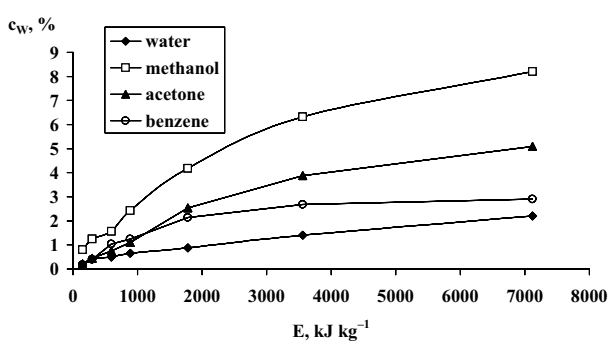

Fig. 4. **Tungsten contamination c_w milled at various specific energy consumption *E***

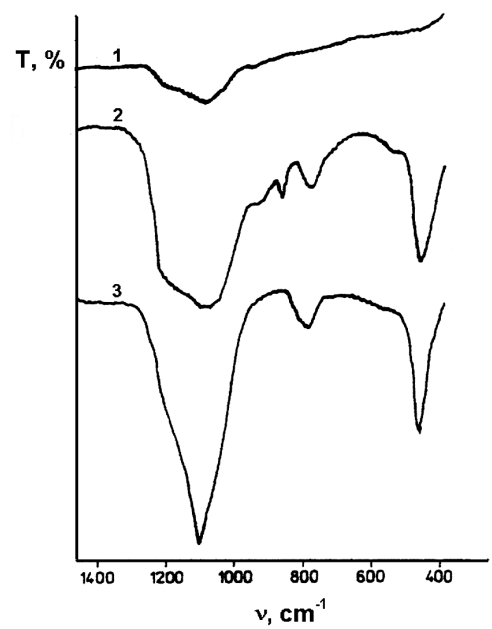

Fig. 6. **Comparison of IR spectra nonactivated samples (1), silicon milled in water environment during 4 hour (2) with the spectrum of standard amorphous silica (3)**

Conclusion

Changes in particle size by intensive milling are connected with the change of surface properties of powders. During energy-intensive milling silicon interacts with the media and milling environment. The thickness of the superficial layer and the share of SiO_2 are increased with increasing permittivity of liquids. The presence of superficial layers on milled particles of silicon markedly influences the value of the specific area. Milling with the tungsten media results in mechanochemical formation of tungsten compounds confirmed by IR spectra. Therefore, the particle size and/or specific surface area data cannot be taken as the measure of the real dispersity of the milled powder.

The authors are grateful to the Slovak Grant Agency for Science (Grant No. 1/0350/03) for financial support of this work.

REFERENCES

1. Tkáčová K.: *Mechanical Activation of Minerals*. Elsevier, Amsterdam-Oxford-New York-Tokyo 1989.
2. Tkáčová K., Števulová N., Bastl Z., Stopka P., Bálintová M.: J. Mater. Res. *10*, 2728 (1995).
3. Yokoyama T., Jimbo G.: Sib. Khim. Zh.. *5*, 56 (1991).
4. Bálintová M., Števulová N.: *Procceedings. of International Conference: New Trends in Mineral Processing III* (Fečko P. ed), p.111. Technical University Ostrava, 1999.
5. Tkáčová K., Števulová N., Lipka J., Šepelák V.: Powder Technol., *83*, 163 (1995).
6. Števulová N., Bálintová M., Tkáčová K., J. Mater. Synth. Proc. *8*, 265 (2000).
7. Pavlukhin Yu. T., Medikov Ya. Ya., Avakumov E. G., Boldyrev V. V.: Izv. Sib. Otd. Akad. SSSR, Ser. Khim. *9*, 11 (1981)
8. Rogachev A. Yu., Bokhonov B. B., Šepelák V., Pavlukhin Yu. T.: *Procceedings. Of 1st Int. Conf. Mechanochemistry* (Tkáčová K. ed), p. 174. Vol. 1, Cambridge Interscience Publishing, Cambridge 1993.
9. Avakumov E. G.: *Mechanochemical Synthesis in Inorganic Chemistry*. Nauka, Moscow 1991.
10. Lazarev A. N. et al.: *Oscillatory spectra: Silicates and its analogues*. Nauka, Leningrad 1975.

L22 SOME NEW BINDERS TESTED AT THE STUDENT LABORATORIES OF THE MATERIALS CHEMISTRY INSTITUTE, BRNO UNIVERSITY OF TECHNOLOGY

JIŘÍ BRANDŠTETR

Department of Materials Chemistry, Faculty of Chemistry, Brno University of Technology, Purkyňova 118, 612 00 Brno, Czech Republic, brandstetr@fch.vutbr.cz

Introduction

The diploma theses as well as the themes for the postgradural students are focused on the actual problems of the materials chemistry important for the activities in the building industry (special concrete, new binders, chemical admixtures) or foundries (ecologically friendly production of molds). The contemporary trend covers the R&D in the broad use of new effective superplasticizers, hybrid inorganic-organic copolymers, biomaterials and better utilization of secondary industrial by-products thus contributing to the solving of economic and ecological problems, enlarging the assortment of binders and concrete. Urgently needed better productivity of materials can distinctly contribute to the saving of natural mineral resources and permanently sustainable living standard of the society.

Special concrete based on portland cement

In last decades, *high-performance (HPC)* and *high--strength concrete (HSC)* are in increasing demand[1]. New composites possess long term durability and high performance. Very promissing utilization show non-traditional composites[2,3] tailored for special applications. The very effective constituents of these composites (concrete) are besides unavoidable silica fumes and microaggregate chemical modificating admixtures, especially new generation of plycarboxylate superplasticizers[4], lowering considerably the w/c ratio and thus enhancing strengths. The increasing important role plays finely ground granulated blast furnace slag (over 500 m^2/kg)[5], fluidized bed ash[6], quartz sand, corundum (used mainly as fine abrasives) and calcite[7]. The high-strength aggregate – fused bauxite is preferred in smaler fractions, similar effect exhibits high-stength basalt, having compressive strengths over 300 MPa. In addition, randomly dispersed steel fibers allow to reach 28-d compressive strengths over 240 MPa[8]. This HSC can in different applications replace steel, its distinct advantage is the lower bulk density 2.800–3.100 kg m^{-3} in comparison with that of 7.500 kg m^{-3} of steel. More expensive, but very effective carbon fibers or microtubes are used in composites of very different matrix, even those based on metals. Still more increasing demand is paid to *self-compacting concretes (SCC)*, enabling some important advanced novelties in the building industry activities[9]. The SCC concrete filled steel tubes used in construction of halls allow to spare steel considerably[10]. Very promissing

is *reactive powdered concrete (RPC)*[11] produced by using mechanochemical activation (high-shear mixing), compacted by hot pressing maintained during the whole setting period.

As microaggregate, fine steel powder was used. The strengths of RPC which hardened in steel tubes reached as much as 800 MPa. The concrete possessing strengths of 1 000 MPa are no more a dream. All the above named novel concrete for different applications contain superplasticizers, the most universal of which are polycarboxylates[4].

Alkali-activated blast-furnace slag (ABFS)

Finely ground granulated BFS is activated by sodium (potassium) hydroxides or preferably by sodium silicate solution (water glass)[12,13,14]. Due to zeolitic properties of the reaction product, it is preferably used for the immobilization of heavy metals. The dense microstructure of CNSAH gel and low porosity ensures low permeability for water and solutions thus improving the chemical corrosion resistance of the material. After exposing to higher temperature, the strengths increase and enable to use this concrete as refractories[15]. Interesting results were obtained in using newly introduced *mixed sodium silicate-aluminate solution* (trade name SIAL 10 or RUDAL) instead of the common sodium water glass: the presence of aluminate monomers in the solution from the very beginning of the alkali activation of powdered aluminosilicates (pozzolans in general) contributes to the formation of amorphous microstructure possessing better ratio of Si/Al, which enables to prepare water cured concretes of 60 d compressive strengths over 140 MPa[16]. In the mixture, the concentration of sodium ions Na^+ must be adequate to the concentration of aluminate to compensate the negative charge of trivalent Al^{III} in the anion $[Al(OH)_4]^-$. The use of sodium aluminate solution of proper concentration as activator of slag (pozzolans) has been tested with interesting results on the evolution of hydration heat, which is being studied by multicell isoperibolic calorimeter[17]. Decisive role in the structure plays the ratio of $SiO_4/AlNaO_4$ tetrahedra in the gel microstructure, which must be higher than 2: while SiO4 tetrahedra form very stable disilicate anions, similar dialuminate does not exist. Therefore, one aluminate tetrahedron (better – AlNa) can be surrounded in the microstructure in hardened composite only by silicate tetrahedra. The mixed sodium silicate-aluminate soution with molar ratio Si/Al about 10 (RUDAL) is now preferably used in the foundries as a binder for molds based on quartz sand, To reach the same proper strengths, considerably lower amount of this activator can be added in comparison with water glass. This phenomenon can be explained by the presence of aluminate monomer in the mixture, enabling the formation of the more stable polymer chain with more favourable Al/Si ratio. The use of mechanochemical activation, especially high-shear mixing, accelerates the reactions of the components. In the presence of other mineral constituents, high shear mixing contributes to the better adhesion of the paste to the microaggregate grains or fibres. The function (problematic) of superplasticizers in alkali activated aluminosilicates was tested unsufficiently thus far. Neverthless, the addition of new type of polycarboxylate superplasticizer to the very neglected blast-furnace slag cement (containing up to 95 % of finely ground GBFS) enables to lower the w/c ratio as much as to 0.20. In activation of very finely ground BFS by 20 % of PC, 28-day compressive strengths of the paste exceed 100 MPa[18].

By the alkali activation of metakaolin (MK), *geopolymers* are prepared possessing similar structure and properties as BF slag composites, imitating natural rocks[19], often calcium-free formations possessing zeolitic character. The reaction of fine MK in high alkaline media of 12–15 M NaOH or KOH brings about faster dissolution of MK (uncomplet) forming at ambient temperature silicate and aluminate monomers. Subsequent addition of water glass soution of silicate modulus 3.3 increases the Si/Al molar ratio to the value 2 or higher producing zeolite (sodalite, natrolite...) precursors. After proper curing, the compressive strengths of these geopolymers can exceed 75 MPa[20].

Solid residues after fluidized bed coal combustion (FBC)

This type of rather neglected material (coarse bed ash and fine fly ash from the separators) formed at the temperatures around 850 °C possesses hydraulic properties and sets and hardens after addition of water only due to the presence of free lime and anhydrite[7]. The use of finely ground bed ash and unavoidable effective superplasticizer allows to lower the water-to-cement ratio under 0.25 and thus to reach the 28 d compressive strengths over 60 MPa[21,22]. The fine fly ash from the separators contains usually too low concentration of free lime, which must be added in preparation of superplasticized composites from this ash. After heating to 130 °C, the excess of free water evaporates, primarily formed ettringite decomposes and the light porous composite exhibits excellent ratio of bulk density to compressive strength (1.000 kg m^{-2} to around 10 MPa)[22,23]. Conspicious results were obtained in using the anhydrite constituent in FBC (up to 30 % of finely ground FBC) for the replacement of gypsum in producing special portland cement. This non-traditional new composite cement with polycarboxylate superplasticizer exhibits pastes or concrete of the same strengths than that based on ordinary PC with traditional gypsum retarder. Conspicious effect show clinker-free superplasticized composites with w/c 0.22 based on BF slag. After activation by 25 % of finely ground FBC bed ash, 360 d compressive strenghths of pastes or concretes exceed as much as 100 MPa[22].

The „green“ binders of foundry sands

Are still more demanded in the casting industry to improve the unfriendly conditions in the foundry halls. Our students are developing new binders based on water soluble proteins and/or polysaccharides. which were succesfully used in the amount 1–1.5 % to the foundry sand[24,25]. These binders improve the ecological conditions in the foundries

considerably. Some of these binders are based on secondary products (wastes) from pharmaceutical industry.

Materials based on clay minerals

Composites based on clay with organic additives (enzymes, saccharides) are being developed for the building industry (earth constructions) and casting industry. Nearly a half of the inhabitants of our planet lives in earth constructions, some of them are thousands of years old. Very sophisticated buldings are *nests (mounds) of termites* – soil eaters[26]. They mixed soil (clay) with enzymes and excrements and this material exhibits very high strengths and resistancy against tropical rains, remarkable is also the architecture of these nests. The mounds are as much as 8 m high and wide, the material of abandoned nests is used for other constructions including tenis courts. The multilayered structure of clay minerals enables the organic constituent to penetrate into the interspace[27,28]. The bond between enzymes and/or saccharides and clay minerals (especially montmorillonite) has been studied to enable the proper selection of these organic additives to improve the performance of the clay inorganic--organic composite (copolymer). The newly invented is often thoroughly forgotten old. Recently, interest in earth constructions is increasing, new buildings are bulit not only in Africa and India, but also in European states and USA[29]. In many countries, modificated clay material is used in road and dam constructions, for the restauration of dumping sites, lagoons and ponds, for landscape forming etc.

In the casting industry, high volume of bentonite is used as a binder in the preparation of moulds (around 8 % plus 3 % of water). Its possible modification especially by enzymes is a part of our contemporary research. The preliminary experiments show possibilities of substantial saving of bentonite by increased performance of the modificated mixture. The complex R & D team consists of specialists in soil material, biochemistry and biology (enzymes) and of people from the casting imndustry.

Thermal energy storage concrete

The effect of saving energy worldwide leeds to different new or older technologies or principles with novel utilization[30]. Rather neglected possibility is the use of concrete blocks impregnated with two phase changing material (PCM). One is butyl stearate, the melting point of which is 19 °C. The research is at present being extended from the laboratory scale. As an active PCM medium, some inorganic salts can also be used ($KF.4H_2O$, $CaCl_2.6H_2O$) with adequate melting point.

Organic-inorganic hybrid biopolymers

Very important and intereseting research is devoted to the study of the structure and properties of biopolymers[31], very different in composition and properties (bones, shells, wings of insects, wood, nut shells, termite mounds…) and possible utilization. Their very sophisticated composition was optimized by nature for hundred thousand of years, they possess outstanding physico-mechanical properties. We try to imitate at least the most simple ones. To this category belongs macro-defect-free concrete (MDF) based mostly on calcium aluminates and polysaccharides, polyvinylacetate-alcohol and other organic compounds[32,33]. Similar reactions proceed between cement constituents and polycarboxylate superplasticizers, enabling the production of gypsum-free cements[33,34]. Recently, new excellent instrumental techniques enable to solve the structure of materials at nanometer scale, which is just the size of molecules and atoms. The study of biopolymers is the interesting topics of many international research teams, nature is for us a constant source of inspiration.

Results published in this paper were partly performed owing to the support of the Grant Agency of the Czech Republic, projects No. 106/01/1277 and No. 103/05/2687.

REFERENCES

1. Aitcin P.-C.: High-performance concrete. SPON, London 1998.
2. Bílek V. (ed.).: Proceedings of the 2nd international conference Non-traditional Cement and Concrete, Brno, University of Technology, Brno 2005.
3. Odler I.: Special inorganic cements. SPON, London 2000.
4. Brandštetr J., Krátký J., Szklorzová H.: Silika *13*, 214 (2003), 14, 40 (2004).
5. Krivenko P.V. (ed.).: Proceedings of the 2nd international conference Alkaline Cements and Concrete, Kiew, SRIBM, Kiew 1999.
6. Brandštetr J.: Stavební materiály *1*, 13 (1998).
7. Brandštetr J., Lukáš J., Krátký J., Hanáková Z.: Silika *13*, 40 (2003).
8. Krátký J., Brandštetr J., Lukáš J., in: Proceedings of the 6th conference Nové stavební hmoty a výrobky, p. *37*. VÚSH Brno 2002.
9. Lukáš J., Brandštetr J., Melcher J., Krátký J.: Beton TJS, *9*, 2003.
10. Lukáš J., Brandštetr J., Melcher J., in: Proceedings of 2nd international symposium Fibre concrete and high--performance concrete, p. 80. Malenovice, 2003. Sekurkon, Praha 2003.
11. Brandštetr J.: Minerální suroviny *1*, 23 (1999).
12. Talling B., Brandstetr J.: Clinker-free concrete based on alkali activated slag, in: Progress in Cement and Concrete (Ghosh S., ed.), Vol. *4*, p. 396. ABI Books, New Delhi (India), 1993.
13. Jelínek K.: Diploma theses, FCH BUT, 2002.
14. Šotek M.: Diploma theses, FCH BUT, 2004.
15. Rovnaník P., Bayer P., Rovnaníková P., in: Proceedings of the 2nd internatioinal symposium Non-traditional Cement & Concrete. p. 46. BUT Brno 2005.
16. Holznerová Š.: Diploma theses, FCH BUT, 2005.
17. Brandštetr J., Polcer J., Krátký J., Holešinský R., Havlica J.: Cem. Concr. Res. *31*, 941 (2001).

18. Bartoníčková E.: Diploma theses, FCH BUT, 2005.
19. Davidovics J. (ed.): Proceedings of the 3rd international konference Geopolymers. Saint Quentin (France), 2005. Geopolymer Institute, Saint Quentin 2005.
20. Huťa J.: Diploma theses, FCH BUT, 2002.
21. Mikulíková R.: Diploma theses, FCH BUT, 2002
22. Opravil T.: Diploma theses, FCH BUT, 2005.
23. Brandstetr J., Havlica J., Odler I.: Properties and use of solid residue from fluidized bed coal combustion, In: Waste Material Used Concrete Manufacturing (Chandra S., ed.), p. *1*. Noyes Publ., Wasterwood, 1996.
24. Laichman L., Brandštetr J., in: Proceedings of the 7th conference New building materials and products, p. 90. Telč 2002. VUSH Brno, 2002.
25. Kramářová D.: PhD dissertation, FCH BUT, 2003.
26. Garnier-Sillam E., Harry M.: Insectes Sociaux *42*, 167 (1995).
27. Horák J.: Diploma theses, FCH BUT, 2005.
28. Pinnavaia T. J., Beal G. W.: Polymer-Clay Nanocomposites. Wiley, New York 2000.
29. Houben H., Guillaud H.: Earth construction. Intermediate technik. Publ., Grenoble 1994.
30. Lee T., Hawes D.VW., Danu D., Feldman D.: Solar Energy Mater. & Solar Cells. *62*, 217 (2000).
31. Raab M.: *Materiály a člověk*. Encyklopedický dům, Praha 1999.
32. Śoukal F.: Diploma theses, FCH BUT, 2004.
32. Drábik M., Slade R. C. T.: Interface Science *12*, 375 (2004).
33. Krátký J.: PhD dissertation, FCH BUT Brno, 2004.
34. Krátký J., Brandštetr J., Opravil J., Šotek M., Szklorzová H., Bartoníčková E., in: Proceedings of the 2nd Symposium Non-traditional Cement and Concrete (Bílek V., Keršner Z., eds.), p.109. BUT, Brno 2005.

L23 MONITORING OF THE CONTAMINATION OF SEWAGE SLUDGE BEFORE THE MATERIAL AND ENERGETIC RECYCLATION

JAN SPONAR and JAROMÍR HAVLICA
Faculty of Chemistry, Brno University of Technology, Purkyňova 118, 612 00 Brno, Czech Republic, sponar@bn.cizp.cz

Introduction

Defining a good or acceptable quality for any product or waste is bound to cause difficulties and problems in definition and interpretation. This is most certainly also the case of a heterogeneous waste product like the sewage sludge. The sewage sludge is a very complex product containing residues or traces of a large number of chemicals used in the society as a whole.

Sewage is produced in the waste water treatment plants (WWTP) by means of sedimentation of the particles of the waste water and the products of biological processing. The biotic and abiotic processes are used for the stabilization of the sludge. The biological stabilization processes include anaerobic and aerobic digestion. Belt presses and especially centrifuging are still the most commonly used dewatering methods. The production of municipal sludge and municipal-industry sludge from the 1 410 Czech WWTP (capacity $1\,432 \cdot 10^6$ m^3, waste water treated $780 \cdot 10^6$ m^3, including precipitation water) represented in 2003 up to 206 000 tonnes of dry matter (DM) or approximately 20 kg DM per person[1]. The comparison is showed in Fig. 1.–4.

Recently new methods of use of the sludge have appeared. The incorporation of the inorganic fraction of the sewage sludge into clinker after the incineration process is a progressive solution. This design requires protection of the environment, particularly the air.

Sewage sludge may contain significant concentrations of potentially toxic metals (Cd , Cr, Cu, Hg, Ni, Pb, Zn), in dependence on their origin and character of the waste water treatment technology. There are still many problems related e. g. to mercury in scope of the long range atmospheric transfrontier pollution, water and soil pollution. Mercury is the most volatile heavy metal and its control requires special treatment technologies, which are constantly under development. The methods are mainly divided in scrubbing and adsorption process, although coupling of these techniques and the utilization of adsorbents and additives are usually required for an efficient control[2]. Cadmium may be a source of the same problem.

Regulations

Emissions regulations for sewage sludge incineration are not stipulated specifically. This is usually covered by the general regulation for waste incineration or clinker production[3]. There are specific limits introduced by the Regional Authority for technology and kinds of waste, which are co-combusted with the main fuel, in this case by The Southern Moravia Regional Authority. Past experience has shown that the trend is to continue in reducing the emission limits.

Limits, for waste water, sewage sludge, soil, and air pollution, which are shown in Table I, are given by different Acts.

Reuse

An effort has been made to find utilization of the sewage sludge as fuel or as an ingredient of the material for clinker production. This kind of recycling of the waste coming from the sewage treatment plant is focused on the removal of pollutants from the environment, making the assessment of the best form of exploitation of the by-product, and the generation of heating-power.

The methods of use of the sewage sludge from the region of Southern Moravia have been investigated by Dobšáková[4]. The results are shown in Table II. The legal possibilities of reuse of the sewage sludge have been discussed[5,6]. The use of sewage sludge focused on the clinker production has been described in several articles. A design of drying technology

Table I
Selected limits for different use of the sewage sludge

Document	Gas phase CO [mg m^{-3}]	SO_2 [mg m^{-3}]	HCl [mg m^{-3}]	Organic carbon [mg m^{-3}]	Cd+Tl [mg m^{-3}]	Hg [mg m^{-3}]	Sb + oth. [mg m^{-3}]	PCDD/PCDF [ng m^{-3}]
EU 2000/76/EC waste co-incineration, cement kilns (day average)	can be set by competend authority	50	10	10	0.05	0.05	0.5	0.1
Germany incineration 17th BImSchV (hours average)	50	50	10	10	0.1	0.05	0.5	0.1
354/2002 Sb., co-combustion of waste, cement kilns (day average, 10 % $O_{2)}$	can be stipulated	50	10	10	0.05	0.05	0.5	0.1
The Southern Moravia Regional Authority specific limit for clinker producer (273.15 °C, 101.32 kPa, 10 % O_2, dry base, day aver.)	no defined	260	10	20	0.05	0.05	0.5	0.1
354/2002 Sb., refuse incinerating plant (day average)	50	50	10	10	0.05 (0.5–8 h)	0.05 (0.5–8 h)	0.5 (0.5–8 h)	0.1 (6–8 h)

Document	Liquid phase NES [mg m^{-3}]	Cd [mg m^{-3}]	Cr [mg m^{-3}]	Cu [mg m^{-3}]	Hg [mg m^{-3}]	Ni [mg m^{-3}]	Pb [mg m^{-3}]	Zn [mg m^{-3}]
Sewage rules Brno, effluents	15	0.005	0.05	0.1	0.001	0.1	0.05	2
Sewage rules Brno, pretreatment units		0.050	0.10	0.5	0.010	0.1	0.10	2

Document	Solid phase NES [mg m^{-3}] DM	Cd [mg m^{-3}] DM	Cr [mg m^{-3}] DM	Cu [mg m^{-3}] DM	Hg [mg m^{-3}] DM	Ni [mg m^{-3}] DM	Pb [mg m^{-3}] DM	Zn [mg m^{-3}] DM
EU 86/278/EEC, agriculture, sludge		20–40		1000–1750	16–25	300–400	750–1200	2500–4000
ČSN 465735, raw material		13	1000	1200	10	200	500	3000
382/2001 Sb., direct use		5	200	500	4	100	200	2500
383/2001 Sb., spec. landfill		500	5000	5000	500	2000	5000	5000
13/1994 Sb., arable land, common soil		1.0	200	100	0.8	80	140	200
13/1994 Sb., arable land, sandy soil		0.4	100	60	0.6	60	100	130

Sb + oth. Sb + As + Pb + Cr + Co + Cu + Mn + Ni + V + Sn st. cond., dry base. based on 11 vol % O_2 in the off-gas
NES non-polar extractable substances

and economy for the selected clinker producer has been set up[7]. The essential part is that the ash of the sewage sludge and the majority of risk elements (heavy metals, risk metals) have been incorporated into the clinker structure simultaneously.

The optimum treatment of the waste water is a removal of the pollutant in the initial parts of the technological course, where the concentration of pollutant is relatively high. If combustion is used at the end of the process, the cleaning

Table II
Results of a questionnaire

WWTP	Production of sewage sludge (DM) [t/y]	Dry matter (DM) [%]	Treatment of sludge	Use
1	80–100	58	drying	biodegradation
2	230	28.4	long-time storage	landfill
3	300–350	18	lime. long-time storage	direct application on arable land
4	500	21	long-time storage	landfill
5	650	24.5	could anaerobic digestion	composting
6	750–800	24	aerobic digestion	composting
7	860	18.22	messofilic anaerobic digestion	composting
8 + near WWTPs	4 322	27.5–28.5	anaerobic digestion	composting
9 + near 19 WWTPs	10 355	liquid 1.1–1.5 dewater. 17–28	biologic treatment dewatering	before 2001 direct use since 2002 composting
10	30 000	30	anaerobic digestion and lime	composting + fertilizers

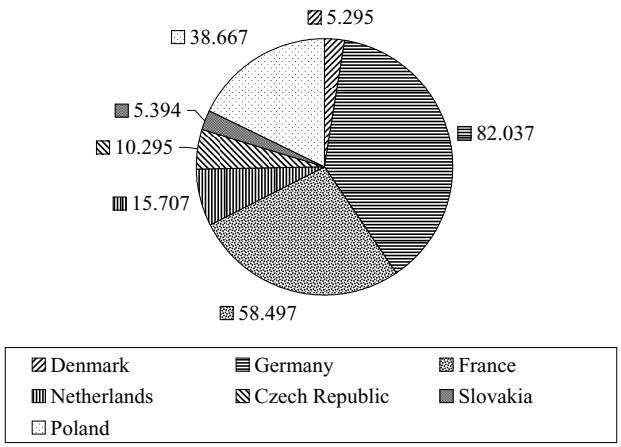

Fig. 1. **Population in selected entities (mil. of habitants, 1998)**

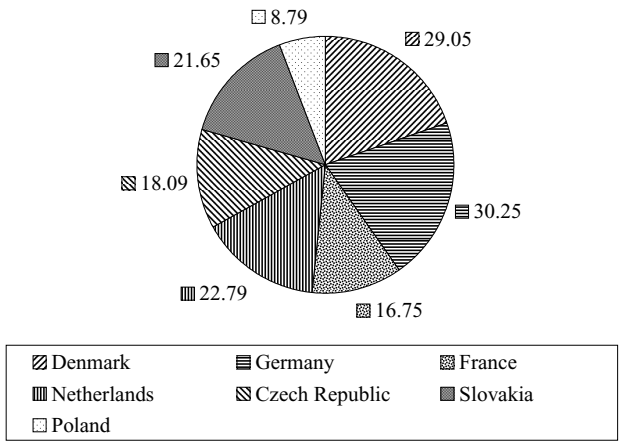

Fig. 3. **Production (in kg DM, 1998) of sewage sludge per person in selected entities**

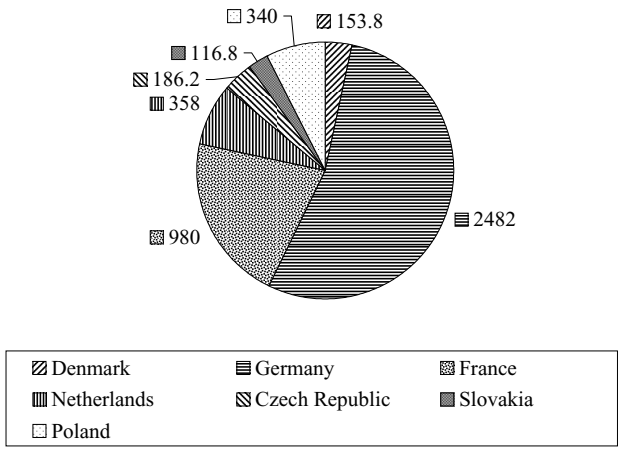

Fig. 2. **Total production (in 1000 ton DM, 1998) of sewage sludge in selected entities**

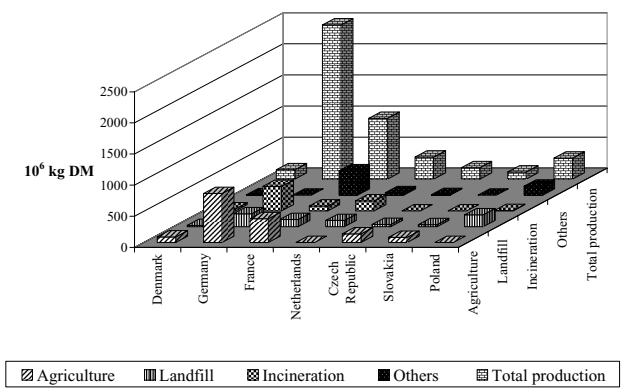

Fig. 4. **Fraction of sewage sludge end-use (1998) in selected entities**

is difficult. The problem is in the cleaning of high amounts of off-gases, because the concentration of pollutant is low ($<10^1$ μg m^{-3}), while the concentration of pollutant in the waste water ranges from 10^{-2} to 10^3 mg dm^{-3} and in the wastes ranges from 10^{-2} to 10^5 mg dm^{-3}. For this reason it is much better to prevent the entrance of risk elements to the waste water and consequently to the sludge.

Experimental

The samples of solids (wastes, different kinds of sludge etc.) and liquids (more frequently the waste water from technologic lines, less often black- and grey-water) were taken at the selected subjects from Brno during 2003–2004. At the same time, the urban waste water collecting system and WWTP (interceptor sewer A, E and F, raw sludge, dewatered sludge and in 2004 dry sludge) were sampled. The volume of each sample was about 500 g for solids and about 1.5 dm^3 for liquids. The analysis was carried out in the laboratories of WWTP Brno, in the laboratory in Brno and in the other one in Praha. The total number of the samples was about 400 and the costs about 1 000 000 Kč.

Analytical methodologies

The risk metals concentration was determined by means of using the atomic emission/absorption spectrometry after a complete acidic digestion and in case of mercury by means of using the flameless atomic absorption spectrometry (automatic mercury analyser AMA 254). Non-polar extractable substances (NES) were determined by the IR spectrometry. The measurement uncertainties were: Cd ± 6–10 %, Cr ± 5–10 %, Cu ± 10 %, Hg ± 10–16 %, Ni ± 4–10 %, Pbm ± 5–10 %, Zn ± 10–12 % and NES ± 20–25 %, depending on the laboratory and the method used.

Results and discussion

Air pollution caused by heavy metals may occur during the combustion. It is necessary to trace these metals in the sludge, to determine their sources and to make an effort to remove them. In case of big cities and industrial zones the task becomes the more difficult because it is uneasy to differentiate the pollution sources.

The sludge, sediments, and technological wastes, particularly from deemulsifying and neutralization units, were sampled. As the next step the analyses of sewage from the collectors, raw sludge, digested sludge, and dry sludge (final product) were carried out.

Two large industrial areas were assessed as the sources of the trace metals (Cd, Cr, Cu, Hg, Ni, Pb, Zn). There are about 20 subjects operating in these areas.

Results of WWTP analyses are shown in Table III. There were found no significant differences at collectors in 2003 and 2004.

The high concentration of Cd (8.2 mg kg^{-1} DM) in dried sludge 2003 was caused by the neutralization unit. The 15days sample on 30.6.2003 reached 147 mg kg^{-1} DM, and on 15.8. it was still 15 mg kg^{-1} DM. The results were a signal

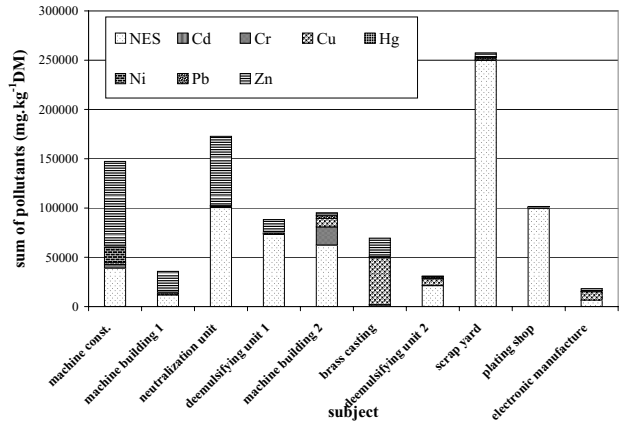

Fig. 5. **Solids-waste of selected producers**

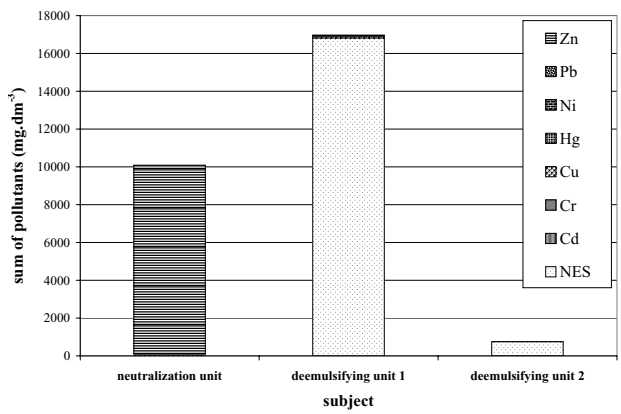

Fig. 6. **Liquids-waste of selected producers**

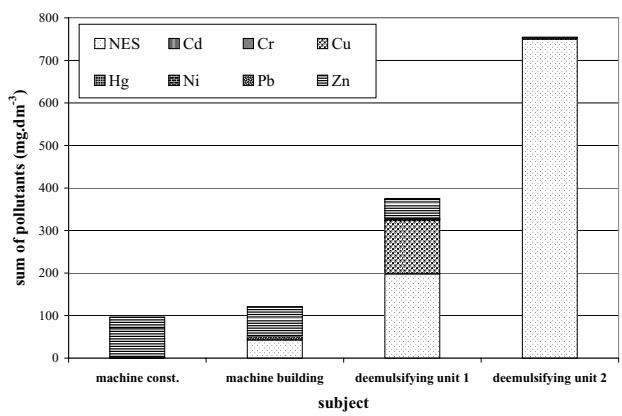

Fig. 7. **Waste water of selected producers**

for opening of this investigation. The subject - the neutralization unit, which caused it, was fined 500 000 Kč and remedial works with estimated costs around 5 000 000 Kč. Sequentially the neutralization unit had been checking for 12 months and there was not found any problem more.

Table III
Analyses of sewers, raw sludge, dewatered sludge and dry sludge, Part A

2003 raw sludge	Cd [mg kg^{-1}] DM	Cr [mg kg^{-1}] DM	Cu [mg kg^{-1}] DM	Hg [mg kg^{-1}] DM	Ni [mg kg^{-1}] DM	Pb [mg kg^{-1}] DM	Zn [mg kg^{-1}] DM
average	2.07	89.95	174.43	2.49	59.95	50.24	1570.67
st. dev.	1.18	31.22	45.44	0.49	33.77	26.47	1072.10
median	1.70	84.00	154.00	2.40	45.00	43.00	1161.00
min	0.99	56.00	116.00	1.70	30.00	32.00	822.00
max	5.80	204.00	336.00	3.70	183.00	141.00	5172.00
n	21	21	21	21	21	21	21

2003 dew. sludge	Cd [mg kg^{-1}] DM	Cr [mg kg^{-1}] DM	Cu [mg kg^{-1}] DM	Hg [mg kg^{-1}] DM	Ni [mg kg^{-1}] DM	Pb [mg kg^{-1}] DM	Zn [mg kg^{-1}] DM
average	8.26	126.15	230.00	3.46	91.08	65.55	2171.52
st. dev.	22.76	26.31	28.53	0.42	25.75	17.50	1190.60
median	2.58	121.00	227.00	3.48	87.00	61.50	1756.50
min	1.60	64.00	134.00	2.60	44.00	47.00	771.00
max	147.10	215.50	289.00	4.60	158.00	142.00	7469.00
n	50	50	50	50	50	50	50

2003 collector A	Cd [mg dm^{-3}]	Cr [mg dm^{-3}]	Cu [mg dm^{-3}]	Hg [mg dm^{-3}]	Ni [mg dm^{-3}]	Pb [mg dm^{-3}]	Zn [mg dm^{-3}]
average	0.00	0.03	0.06	0.44	0.04	0.02	0.19
st. dev.	0.00	0.01	0.04	0.11	0.02	0.00	0.13
median	0.00	0.04	0.05	0.38	0.04	0.02	0.17
min	0.00	0.01	0.03	0.38	0.01	0.02	0.01
max	0.01	0.04	0.14	0.67	0.10	0.02	0.49
n	12	12	12	12	12	12	12

2003 collector E	Cd [mg dm^{-3}]	Cr [mg dm^{-3}]	Cu [mg dm^{-3}]	Hg [mg dm^{-3}]	Ni [mg dm^{-3}]	Pb [mg dm^{-3}]	Zn [mg dm^{-3}]
average	0.00	0.04	0.06	0.49	0.04	0.02	0.28
st. dev.	0.00	0.00	0.04	0.34	0.00	0.00	0.27
median	0.00	0.04	0.05	0.38	0.04	0.02	0.18
min	0.00	0.02	0.02	0.38	0.03	0.02	0.01
max	0.01	0.04	0.17	1.62	0.04	0.03	1.05
n	12	12	12	12	12	12	12

2003 collector F	Cd [mg dm^{-3}]	Cr [mg dm^{-3}]	Cu [mg dm^{-3}]	Hg [mg dm^{-3}]	Ni [mg dm^{-3}]	Pb [mg dm^{-3}]	Zn [mg dm^{-3}]
average	0.00	0.07	0.06	0.63	0.05	0.04	0.19
st. dev.	0.00	0.09	0.02	0.43	0.04	0.05	0.09
median	0.00	0.04	0.06	0.38	0.04	0.02	0.17
min	0.00	0.04	0.02	0.38	0.04	0.02	0.04
max	0.00	0.38	0.08	1.80	0.18	0.22	0.36
n	12	12	12	12	12	12	12

Table III
Analyses of sewers, raw sludge, dewatered sludge and dry sludge, Part B

2004 raw sludge	Cd [mg kg^{-1}] DM	Cr [mg kg^{-1}] DM	Cu [mg kg^{-1}] DM	Hg [mg kg^{-1}] DM	Ni [mg kg^{-1}] DM	Pb [mg kg^{-1}] DM	Zn [mg kg^{-1}] DM
average	1.25	75.66	183.15	2.78	57.60	58.98	1839.45
st. dev.	1.39	32.43	144.93	0.68	49.78	109.05	1711.87
median	1.00	72.00	159.00	2.70	46.00	41.00	1320.00
min	0.30	27.00	96.00	1.39	20.00	16.00	534.00
max	10.80	202.00	1200.00	4.36	328.00	835.00	11300.00
n	53	53	53	53	53	53	53

2004 dew. sludge	Cd [mg kg^{-1}] DM	Cr [mg kg^{-1}] DM	Cu [mg kg^{-1}] DM	Hg [mg kg^{-1}] DM	Ni [mg kg^{-1}] DM	Pb [mg kg^{-1}] DM	Zn [mg kg^{-1}] DM
average	1.66	121.54	242.54	3.25	85.72	64.46	3138.75
st. dev.	0.64	30.31	55.53	0.53	28.88	28.69	996.76
median	1.57	116.00	234.50	3.28	81.00	54.00	3500.00
min	0.65	70.00	71.00	1.02	38.00	29.00	1170.00
max	3.27	190.00	392.00	4.00	220.00	147.00	5230.00
n	48	48	48	48	48	48	48

2004 dried sludge	Cd [mg kg^{-1}] DM	Cr [mg kg^{-1}] DM	Cu [mg kg^{-1}] DM	Hg [mg kg^{-1}] DM	Ni [mg kg^{-1}] DM	Pb [mg kg^{-1}] DM	Zn [mg kg^{-1}] DM
average	2.11	116.19	293.19	3.57	119.49	78.94	3109.14
st. dev.	0.59	27.75	50.24	0.58	51.57	33.27	1404.02
median	2.03	117.00	304.00	3.61	100.50	75.00	2800.00
min	0.88	61.00	80.00	1.14	41.00	37.00	1230.00
max	3.85	216.00	380.00	4.78	326.00	178.00	6580.00
n	58	58	58	58	58	58	58

2004 collector A	Cd [mg dm^{-3}]	Cr [mg dm^{-3}]	Cu [mg dm^{-3}]	Hg [mg dm^{-3}]	Ni [mg dm^{-3}]	Pb [mg dm^{-3}]	Zn [mg dm^{-3}]
average	0.00	0.02	0.08	0.85	0.02	0.03	0.25
st. dev.	0.00	0.01	0.05	1.03	0.01	0.01	0.15
median	0.00	0.01	0.07	0.38	0.02	0.02	0.21
min	0.00	0.01	0.03	0.38	0.01	0.02	0.05
max	0.00	0.05	0.24	3.60	0.06	0.04	0.57
n	12	12	12	12	12	12	12

2004 collector E	Cd [mg dm^{-3}]	Cr [mg dm^{-3}]	Cu [mg dm^{-3}]	Hg [mg dm^{-3}]	Ni [mg dm^{-3}]	Pb [mg dm^{-3}]	Zn [mg dm^{-3}]
average	0.00	0.03	0.10	0.48	0.03	0.03	0.31
st. dev.	0.00	0.01	0.08	0.23	0.02	0.01	0.12
median	0.00	0.03	0.09	0.38	0.03	0.02	0.31
min	0.00	0.01	0.03	0.38	0.01	0.02	0.12
max	0.00	0.04	0.32	1.20	0.06	0.05	0.50
n	12	12	12	12	12	12	12

Table III
Analyses of sewers, raw sludge, dewatered sludge and dry sludge, Part C

2004 collector F	Cd [mg dm^{-3}]	Cr [mg dm^{-3}]	Cu [mg dm^{-3}]	Hg [mg dm^{-3}]	Ni [mg dm^{-3}]	Pb [mg dm^{-3}]	Zn [mg dm^{-3}]
average	0.00	0.02	0.07	0.46	0.02	0.04	0.25
st. dev.	0.00	0.01	0.04	0.17	0.01	0.04	0.21
median	0.00	0.02	0.07	0.38	0.02	0.02	0.23
min	0.00	0.01	0.01	0.38	0.01	0.02	0.01
max	0.00	0.04	0.13	0.80	0.04	0.17	0.80
n	10	10	10	10	10	10	10

The rise of Zn (3140 mg kg^{-1} DM) in dried sludge 2004 was caused in several periods (4. 2.–15. 3., 26. 3.–28. 4. and 13. 9.–27. 9.), where the concentration of Zn was between 3500 mg kg^{-1} DM and 5200 mg kg^{-1} DM. A subject causing pollution has not been discovered yet, but the sources of pollution have. In this areas are operating machine building unit, machine construction and deemulsifying unit 1. The average of pollutant concentration in the solid waste in subject is shown in Fig. 5. Fig. 6. illustrates the average concentration of pollutant in the liquid waste. Fig. 7. represents the average of pollutant concentration in the waste water. These results provide very good knowledge of the treated or produced the solid waste and the liquid waste may lead to a discovery of a potential pollution producer.

Conclusions

For the prevention of entrance of the risk elements into the waste water and consequently into the sludge it is necessary for WWTP to cooperate with the authorities, strictly keep the Municipal Sewage Rules and to punish every subject, which transcends it. The authorities have to have a very good knowledge of the treated or produced wastes in area and to support WWTP. This way is very expensive for the authorities, because they have to have a evidence before to charge someone. In this case about 400 samples had been taken and the costs reached more then 1 000 000 Kč.

REFERENCES

1. http://europa.eu.int/comm/eurostat/
2. Lopes M. H., Abelha P., Lapa N., Oliviera J. S., Cabrita I., Gulyurtlu I.:Waste Management, *23*, 859 (2003).
3. http://europa.eu.int/comm/environment/
4. Dobšáková M.: *Diploma theses*, Mendel University of Agriculture and Forestry, Brno, CR, 2004.
   Dobšáková M., Sponar J.: Odpady 2, 26, (2003).
6. Šťasta P., Boráň J., Bébar L., Stehlík P., Oral J., Sponar J.: SOVAK, *13*, 19, (2004).
7. Šťasta P.: Doctoral essay, Technical University of Brno, Brno, CR, 2005.